UNDERSTANDING THE PHYSICS OF X-RAY EMISSION IN YOUNG STARS

By

Sonali J. Shukla

Dissertation

Submitted to the Faculty of the

Graduate School of Vanderbilt University

in partial fulfillment of the requirements

for the degree of

DOCTOR OF PHILOSOPHY

in

PHYSICS

August 2009

Nashville, Tennessee

Approved:

Professor David A. Weintraub

Professor John C. Ayers

Professor Robert A. Knop

Professor Robert J. Scherrer

Professor Keivan G. Stassun

ABSTRACT

The goals of the research presented in this dissertation are to better understand the characteristics of the X-ray emitting plasmas of young stars and the physical mechanisms that produce the emission. We seek to achieve these goals through the analysis of X-ray observations of a sample of young stars, particularly T Tauri stars, obtained with the CXO. First, we present spatially-resolved X-ray observations of the binary T Tauri star system V710 Tau. Using Chandras Advanced CCD Imaging Spectrometer (ACIS), we imaged this 3.2 separation binary system, consisting of a classical T Tauri star, V710 Tau N, and a weak-lined T Tauri star, V710 Tau S. The Chandra images cleanly resolve the V710 Tau binary, demonstrating that both stars emit X-rays and thereby enabling the first spectral/ temporal study of the individual components of this mixed (classical and weak-lined) T Tauri star binary system. The northern component, V710 Tau N, appears to have been in a flaring state during the first (2004 December) exposure. During this flare event, the X-ray flux of the classical T Tauri star hardened significantly. Single-component plasma models with plasma temperatures in the range kTX $\sim$ 0.7 1.1 keV are adequate to fit the observed X-ray spectra of V710 Tau S in 2004 December and both stars in 2005 April. The 2004 December flare-state observation of V710 Tau N requires a higher-temperature plasma component (kTX $\sim$ 2.5 3.0 keV) in addition to the soft component (kTX $\sim$ 0.5 keV) and is better fit by a model that includes a slightly enhanced Ne/Fe abundance ratio. These results are generally consistent with statistical contrasts between the X-ray emission properties of classical (rapidly accreting) vs. weak-lined (weakly accreting or non-accreting) T Tauri stars.

Then, we present analysis of Chandra High Energy Transmission Grating Spec-

troscopy (HETGS) relatively long integration, high spectral resolution data for a sample of nine young stars, including classical, weak-lined, and post-T Tauri stars as well as a young main sequence star. For five of these nine stars we observed significant flaring during the Chandra observing epochs. We extracted spectra for each observation, and for the observations with significant flaring, we extracted separate spectra for the flaring and quiescent epochs. From these spectra, we measured the line fluxes of the strongest emission lines, most notably the Hydrogen-like Lyman line and the He-like triplet (forbidden, intercombination, and resonance) lines for Si, Mg, and Ne as well as strong Fe lines. From these line flux measurements, we were able to infer densities and temperatures from line flux ratios sensitive to these properties. In general, the quiescent state observations have higher densities (as inferred by the density-sensitive R ratio) than the flaring state observations. By measuring elemental abundance ratios, we find that all the observations of the stars in our sample have a high Ne/Fe ratio, but only one, TW Hya in quiescence, shows an enhanced Ne/O ratio. The X-ray emitting plasmas of the stars in our sample are therefore not likely to be depleted of grain forming elements.

ACKNOWLEDGEMENTS

A number of people deserve credit for their efforts and guidance that have directly contributed to the work included within this dissertation. First, and foremost, I thank my academic adviser, Professor David Weintraub, for his support and encouragement in the development and progress of this study. He has been an ideal advisor in every way, and I only wish I had always been a model student under him. I consider myself very fortunate to have studied under his guidance. Among many other things, he introduced me to a group of mentors that have been invaluable in putting this thesis together. To begin with, I thank Professor Joel Kastner at the Rochester Institute of Technology who introduced me to the world of X-ray astronomy. In addition, I could not have possibly understood all the nuances of X-ray astronomy (not that I claim to even now) without the mentorship and guidance of Dr. David Huenemoerder and Dr. Norbert Schulz of the Massachusetts Institute of Technology, as well as Dr. Paola Testa of Harvard University's Center for Astrophysics. Not only did they kindly host me twice during my tenure as a graduate student, but have continued their collaboration with me, often going out of their way to promptly reply to emails about even the most trivial questions.

I would also like to thank the other members of my committee: Professor Robert Scherrer, Professor John Ayers, Professor Keivan Stassun and Dr. Robert Knop. This group of people has always encouraged me to meet my goals and expectations without ever making me feel like I was being tested. Rather, they were each truly mentors, contributing to my growth as a researcher. In 2006, I was offered a Spitzer Pre-

doctoral Fellowship at the California Institute of Technology. Once again, I have to thank my adviser, Professor Weintraub, for encouraging me to apply and also thank my committee for accommodating me while I was away from Vanderbilt. During my year there, I was able to learn an entire new skill set with a new project under the tutelage of Dr. Patrick Lowrance and Dr. Davy Kirkpatrick. My experience at Caltech gave me much perspective into the world of astrophysical research as well as opened the doors to many new opportunities and new friendships.

Speaking of friends, I want to thank all of you for your continued support, from those of you that first learned the meaning of "astrophysicist" from me in middle school, to my colleagues and mentors at UT and at Vanderbilt, and finally to my roommates, particularly Sarah, who supported me during the long hours of hard work required to write this dissertation.

There are not words enough to thank and acknowledge my family. My parents have always encouraged my dream to become an astrophysicist, and never once doubted that I had the ability to do so. From taking me to see Halley's Comet at age four to cutting out news articles about astronomy, they have inspired me to turn my lifelong interest in astronomy into a career and have shown nothing but joy in my successes thus far. Thank you also to my little brother, who has followed in my footsteps and declared physics as his major in college. Whether this is flattering or alarming, I haven't yet decided, but I thank him for the many useful discussions of basic physical concepts that have come up in putting this dissertation together. Finally, to my sister and brother-in-law, I could not possibly have survived this entire period of my life if I had not had your experiences in graduate school to draw from. You have been

invaluable in helping me make the right decisions and choose the best path over the past six years. Sis, you'll always be the first Dr. Shukla to me.

TABLE OF CONTENTS

LIST OF TABLES

LIST OF FIGURES

CHAPTER I

BACKGROUND

1.1 Introduction

Since their classification by Joy in 1945, T Tauri stars have become a pivotal group of objects studied in depth by astronomers as they endeavor to understand the birth of stars. T Tauri stars, named for their prototype, T Tau, range in mass from 0.5 to 2 solar masses, and as such are pre-main sequence solar analogs. Although T Tauri stars are optically visible, they are associated with nebulosity but are not completely enshrouded by dust and gas. These observational results suggest that the surrounding circumstellar material must be confined spatially, with much of that material most likely in relatively flat, circumstellar disks. These basic characteristics make them ideal objects for understanding the interactive processes between young, forming stars and the material that surrounds them.

One unique defining characteristic of T Tauri stars is that they exhibit chromospheric emission lines, the most prominent being Hα, the hydrogen Balmer line. The bulk of the Hα emission is thought to arise from shocks on the stellar surfaces of these young stars (Barrado y Navascués & Martín, 2003), which are attributed to accretion of material from circumstellar disks. Classification of T Tauri stars stems from measurements of the equivalent width of the Hα line. Originally, classical T Tauri stars (cTTS) were defined as having Hα EW $>$ 10 Å (i.e., enough Hα emission to indicate active accretion), and weak-lined T Tauri stars (wTTS) as having Hα EW

< 10 Å (i.e., a minimal amount of Hα emission, probably all due to coronal activity rather than accretion). However, the strength of the Hα line depends slightly on spectral type, so Martin (1997) proposed a classification scheme in which the Hα EW boundary separating cTTS and wTTS changes with spectral type and suggests using Hα EW thresholds of $\sim$5 Å for K-type stars, $\sim$10 Å for early-M type stars, and $\sim$20 Å for late-M type stars. Note, however, that Hα emission can be generated and vary depending on other stellar properties such as binarity, flare activity, and the strength of a stellar wind.

Other defining characteristics of cTTS, such as ultraviolet and infrared excesses, as well as the presence of forbidden emission lines, can also be used to distinguish cTTS from wTTS. CTTS in particular exhibit strong near-infrared excesses, with an excess defined as more emission in a wavelength range than expected from only the stellar photosphere. Near-infrared excesses occur when ultraviolet and optical light from the star are absorbed by dust grains surrounding the star and re-radiated at longer wavelengths. Thus the detection of near-infrared excess emission indicates the presence of dust in the inner regions of a circumstellar disk. Assuming that a single dust grain radiates nearly as a blackbody, the peak wavelength of emission from a dust grain corresponds to the temperature of that dust grain. For a population of dust grains in a circumstellar disk, near-infrared emission in the wavelength range of one to ten microns corresponds to dust grains with temperatures of hundreds to a few thousands of Kelvins. These grains are thought to be found within one astronomical unit (AU) of the star. Similarly, mid-infrared and far-infrared emission indicates the presence of cooler dust grains that are found at increasingly larger distances from the

central star.

T Tauri stars are also known to be sources of thermal continuum emission at submillimeter wavelengths (Weintraub et al., 1989). Submillimeter continuum emission is indicative of the presence of cold dust grains located at distances of tens to hundreds of AU from the star. Most stars that possess near-infrared excesses also show evidence of submillimeter emission. However, some wTTS possess weak submillimeter excesses, as much as an order of magnitude weaker than the submillimeter flux seen toward cTTS (Beckwith et al., 1990), but no near-infrared excesses. Submillimeter continuum emission can also be used to calculate the dust mass and total mass of these circumstellar disks (Hildebrand, 1983). Polarization studies can also show if the grains in these circumstellar disks are aligned.

Radio emission from CO molecules is the most prominent tracer of circumstellar gas associated with T Tauri stars. In addition to probing gaseous regions through the emission of radio lines of gas tracers, the detection of radio continuum emission can provide information about a young star's magnetic field. In wTTS, there is evidence for moderately variable, nonthermal radio emission that is being emitted from relatively small volumes. Since this radio emission is circularly polarized, the emission process may be synchrotron emission from electrons spiraling about stellar magnetic field lines (Feigelson & Montmerle, 1999).

T Tauri stars are also strong X-ray emitters. The ratio of X-ray luminosity to bolometric luminosity, which is typically in the range from 10^{-4} to 10^{-3}, is much greater than that which is observed for main sequence stars (Montmerle, 2002). Early type stars (O3 - A5) generally show a ratio of X-ray to bolometric luminosity of

$\sim 10^{-7}$, whereas in late type stars (G to M), the ratio is $\sim 10^{-6}$, though for these stars the X-ray luminosity strongly depends on rotation rate (Pallavicini et al., 1981). Typical X-ray luminosities of TTS range from $L_X \sim 10^{30}$ to $L_X \sim 10^{31}$ erg s^{-1}, three to four orders of magnitude greater than the average X-ray solar luminosity ($L_X \sim 10^{27}$ erg s^{-1}). Since young stars are such strong X-ray emitters (among stars), early X-ray observations with satellites like Einstein and ROSAT were responsible for finding large populations of wTTS that lacked previously identified optical and infrared counterparts. According to Montmerle (2002), about 75% of the known TTS population has been detected in X-ray emission. The origin of the X-ray emission is still unknown, but most likely stems from a combination of coronal activity caused by a dynamo and shocks produced by magnetically funneled accretion of material from the circumstellar environment onto the star. This dissertation further investigates the emission of X-rays from T Tauri stars and the role of X-ray emission in characterizing key steps in early stellar evolution.

1.2 X-ray studies of young stars

Young stars and low-mass pre-main sequence (T Tauri) stars are well-established as strong X-ray sources. Almost certainly, the production of hard (E $\geq$ 1 keV) X-rays in the environments of young stars is linked to magnetic reconnection events. The stimulus of the magnetic reconnection events that generate the X-rays, however, is still a subject of considerable debate (see discussions in Preibisch & Feigelson (2005) and Telleschi et al. (2007b)). X-ray production in active stars can be attributed to many processes. In young stars, X-rays are thought to be produced by the heating

and confinement of coronal plasma by a strong magnetic field. However, multiple processes may contribute to coronal heating. In young stars, both dynamo activity and star-disk interactions can, in principle, produce X-rays, but it remains to be established whether and to what degree both processes contribute to the observed X-ray emission. If accretion of material from the surrounding disk onto the star produces a distinct X-ray signature, X-ray emission characteristics of cTTS and wTTS should differ, since cTTS are thought to be actively accreting material from their disks while wTTS are not actively accreting.

High-resolution X-ray spectra for the classical T Tauri stars TW Hya (Kastner et al., 2002; Stelzer & Schmitt, 2004), BP Tau (Schmitt et al., 2005), and V4046 Sgr (Günther et al., 2006) indicate that the cooler (log T $\sim$6.5) X-ray emitting plasma from these stars is produced via accretion-generated shocks. Robrade & Schmitt (2006) find that accretion shocks contribute to the observed X-ray emission of several cTTS (TW Hya, BP Tau, CR Cha, SU Aur) though the fraction of X-rays generated by accretion rather than dynamo activity varies from source to source. Long-term X-ray and infrared light curves obtained from observations of V1647 Ori during its accretion-powered optical/IR eruption in 2003-2004 (Kastner et al., 2006) also favor accretion as the ultimate source of the magnetically-derived X-ray emission seen toward this pre-main sequence object. On the other hand, statistical studies of X-ray properties derived from low-resolution imaging spectra, which show that the mean X-ray luminosity of cTTS is two to three times lower than that of wTTS (Flaccomio et al., 2003; Preibisch et al., 2005; Feigelson et al., 2005; Günther et al., 2006; Telleschi et al., 2007b) — and that rapid rotation and strong X-ray emission are positively cor-

related for main sequence stars (Randich, 2000) and pre-main sequence stars (Stelzer & Neuhäuser, 2001; Stassun et al., 2004) — point to pre-main sequence stellar dynamo activity as the source of the X-rays. However, Feigelson et al. (2003) found that pre-main sequence stellar rotation and X-ray emission were slightly anti-correlated. Indeed, accretion may play a role in the apparent suppression of the X-ray luminosities of cTTS relative to wTTS. Telleschi et al. (2007b) suggest that this effect may be due to cooling of cTTS coronal material by accretion streams.

One of the more interesting lines of evidence in this debate is that presented in a study by König et al. (2001) of multiple T Tauri stars in Taurus. They found statistical evidence in ROSAT data that primaries are more X-ray luminous and produce harder X-rays than secondaries. They also found that, in cases for which rotational velocities and bolometric luminosities were known, primaries are more rapidly rotating and/or more luminous. Stronger X-ray emission, they concluded, is due either to higher bolometric luminosity or faster rotation.

Spatially-resolved X-ray observations of stars in wTTS/cTTS binary systems have the potential to be especially valuable for determining differences in the X-ray properties of these two classes of pre-main sequence stars, as the component stars in such systems are likely to have similar ages. Such observations have been rendered feasible by the subarcsecond spatial resolution of the Chandra X-ray Observatory. In the first example of such an observation, the borderline wTTS/cTTS system Hen 3-600 was studied by Huenemoerder et al. (2007) with the Chandra High Energy Transmission Grating Spectrograph (HETGS). Signatures of accretion were found in these X-ray gratings spectroscopy data. The results — though somewhat ambiguous — implicate

the more rapidly accreting component in the Hen 3-600 binary as the source of these signatures.

1.3 High-resolution X-ray spectroscopic studies

The launching of the latest generation of X-ray observatories (Chandra and XMM-Newton) with instruments capable of high-resolution X-ray spectroscopy has allowed for in-depth X-ray wavelength studies of young stars. In particular, studies of cTTS that are thought to be actively accreting have shed light as to the X-ray properties associated with accreting stars. In studying stars with evidence of disks, accretion and star-disk interactions (assuming the star and disk are connected via magnetic fields) can also be considered as mechanisms for generating X-ray emission. Even with the sensitivity of these instruments, observations of individual sources are time-intensive, and thus very few TTS have been observed with either XMM-Newton or Chandra. For this study, we have selected a sample of X-ray bright, young stars observed with the high-resolution X-ray spectrometer on Chandra. Some of these observations have been analyzed and the interpretations published, though at varying levels of depth, and others of these observations have not been studied at all. The basic properties of each star included in our sample (§1.3.1 - §1.3.9) as well as a few other examples of T Tauri star high resolution X-ray studies with other instruments (§1.3.10) are outlined below.

1.3.1 *TW Hya*

TW Hya is the nearest known cTTS, at a distance of 56 parsecs, and is the namesake member of the TW Hya association (Kastner et al., 1997). Not only is TW Hya the closest cTTS, but it is known to have a dusty and gaseous circumstellar disk from which it is strongly accreting, as is evident from its large Hα equivalent width of -220 Å (Webb et al., 1999). In addition, Hughes et al. (2008) found, from submillimeter observations from the Submillimeter Array, that a dust disk around TW Hya extends to 60 AU, and Weinberger et al. (2002) has observed scattered light out to a distance of $\sim$230 AU from the central star. Based on their analysis of line ratios of high-resolution X-ray data obtained from Chandra for TW Hya, Kastner et al. (2002) found that (1) the temperature distribution derived from fluxes of temperature-sensitive, He-like ions is sharply peaked at log $T = 6.5$ and (2) the density-sensitive line ratios of Ne IX and O VIII (see §3.1.1 for further explanation) indicate plasma densities of log $n_e > 12$. This plasma density is more than an order of magnitude higher than density estimates obtained for coronally active, late-type stars. Together, these results strongly suggest that the X-rays from the cTTS TW Hya are generated by accretion streams that connect the circumstellar disk to the star. This result has received strong support from the analysis of XMM-Newton observations of TW Hya (Stelzer & Schmitt, 2004). Stelzer & Schmitt (2004) find that the forbidden line of the O VII triplet at 22.1 Å is very weak or not present in the spectrum of TW Hya. They suggest the low value of the flux ratio between the forbidden to intercombination *(f/i)* line ratio[1] for O VII indicates an extremely high

[1]The *f/i* ratio will be further discussed in Chapter 3.

density for the X-ray emitting plasma and possibly a high radiation field in which that material is immersed. The photosphere of TW Hya is cool, but the *f/i* ratio is significantly smaller than the *f/i* ratios observed in other cool stars.

1.3.2 *HD 98800*

HD 98800 is a quadruple system also located in the TW Hya association but at a slightly closer distance of 47 parsecs. The system consists of two visual binaries, each of which has a spectroscopic binary companion. Although HD 98800 shows a copious amount of infrared excess (Sylvester et al., 1996), no Hα emission signature has been detected around it, which suggests that one member of the system harbors a dusty disk but that no active accretion is occurring. This component would be a wTTS. Sylvester et al. (1996) also find excess emission in the HD 98800 system at submillimeter wavelengths, which is consistent with the presence of the dusty disk, as indicated by the infrared observations. Kastner et al. (2004) report, from Chandra high-resolution X-ray observations, that the X-ray emitting plasma seen toward HD 98800 is at a much lower density than for TW Hya, $\log n_e \leq 11$, which is a typical electron density for coronae. If high-density observed in an X-ray emitting plasma is indeed indicative of accretion-generated X-rays, then these results suggest that the X-ray emission from HD 98800 is not generated via accretion.

1.3.3 *Hen 3-600*

Like TW Hya and HD 98800, Hen 3-600 is also a member of the nearby TW Hya association at distance of 34 parsecs. It is a close binary system, with a separation of

only 1.4". The Hen 3-600 system exhibits both near and mid-infrared excesses, and the bulk of the excess emission is thought to come from a disk surrounding the primary component. The primary component is thought to be actively accreting and has the second largest Hα equivalent width (Hα EW = -22 Å) in the TW Hya association, following only TW Hya itself (Huenemoerder et al., 2007). The secondary component has a smaller Hα EW of -7 Å. Though the primary component has a strong evidence of accretion, it has a low accretion rate (Muzerolle et al., 2000).

Chandra high-resolution observations by Huenemoerder et al. (2007) of Hen 3-600 suggest the presence of a high density X-ray emitting plasma. As for TW Hya, they suggest that this high density is due to accretion shocks. Huenemoerder et al. (2007) further suggest that the density diagnostic of the ratio of the forbidden (f) to inter-combination (i) line strengths of He-like ions (see section 3.1.1 for more details) may provide a distinguishing criterion for determining whether accretion is a mechanism by which X-rays are produced by young stars (Huenemoerder et al., 2007).

1.3.4 *SU Aur*

SU Aur, first defined as a wTTS based on Hα equivalent width by Herbig & Bell (1988), is a young star in the Taurus-Auriga star forming region. SU Aur has a spectral type of G2, which is an earlier spectral type than is found for most T Tauri stars, meaning that its photosphere is warmer than those of most T Tauri stars and thus SU Aur produces a brighter continuum (Bertout et al., 1988). The Hα equivalent width for SU Aur is variable, but in general is lower than those found in other cTTS. However, the bright continuum masks the bulk of the Hα emission (Johns

& Basri, 1995). Akeson et al. (2002) model infrared and millimeter fluxes observed interferometerically to show that SU Aur harbors a massive disk that extends to ∼400 AU from the central star. Given the above characteristics, we believe that SU Aur is more appropriately classified as a cTTS, and we consider it a cTTS in this dissertation.

SU Aur has been observed with the high-resolution spectrometers aboard both Chandra and XMM-Newton, but only the XMM-Newton results have been published. Robrade & Schmitt (2006) were unable to measure the O VII triplet due to strong circumstellar absorption and the presence of an extremely hot plasma. They were able to measure the O VII Lyα line definitively, which indicates that if the O VII triplet exists, it should have been detected. Since it is not detectable, Robrade & Schmitt (2006) assume that the environment of SU Aur does not contain large amounts of cool X-ray emitting plasma.

1.3.5 *DoAr 21*

DoAr 21 is a young star in the Rho Ophiuchus star-forming region which is at a distance of ∼160 parsecs. DoAr 21 is generally classified as a wTTS because of its weak Hα emission (-0.6 Å) (Bouvier & Appenzeller, 1992) and lack of an infrared excess (Barsony et al., 2005). Submillimeter observations conducted by Andre & Montmerle (1994) reveal no evidence of cold circumstellar material surrounding DoAr 21. However, Bary et al. (2002) detect emission from molecular hydrogen centered at the rest wavelength of the star and in a small unresolved beam centered on the star, which they interpret as evidence for the presence of a gaseous disk around the

star, though the star does not appear to be actively accreting from the disk. Imanishi et al. (2002) analyzed Chandra imaging spectra of DoAr 21 and found the spectra to be well fit with a one temperature model. No analysis of the Chandra high-resolution X-ray spectra has been published.

1.3.6 *V987 Tau*

At a distance of 128 parsecs, V987 Tau is a member of the Taurus-Auriga star-forming region, and its youth is confirmed by a high Li abundance (Pasquini et al., 1991). V987 Tau is classified as wTTS based on its Hα line, which is seen in absorption, with an equivalent width of 1.01 ± 0.14 Å (Nguyen et al., 2009), and is thus not thought to be actively accreting from a circumstellar disk. Furlan et al. (2006) find no significant infrared excess around V987 Tau, but weak submillimeter emission has been detected toward the star, indicating the possibility that V987 Tau is surrounded by a cold dust disk (Andrews & Williams, 2005). A high-resolution X-ray observation of V987 Tau using the high-resolution spectrometer aboard XMM-Newton was analyzed by Scelsi et al. (2005). The Chandra high-resolution X-ray observation was analyzed by Audard et al. (2005). Both groups found similar results for the X-ray emitting plasma, that it had approximately the same density as other coronally active sources.

1.3.7 *HIP 92680*

HIP 92680, also known as PZ Telescopii, is located in the Tucana association, a star-forming region at a close distance of $\sim$45 parsecs (Zuckerman & Webb, 2000).

It has an estimated age of ∼20 Myr and is known to be rapidly rotating (P_{rot} = 0.94 days) (Argiroffi et al., 2004). It is a K0V (Houk, 1978), and the spectral signatures of strong Li and Hα seen in emission indicate that this star is relatively young (Soderblom et al., 1998). Argiroffi et al. (2004) classify HIP 92680 as a post-TTS with X-ray properties distinct from both young accreting stars like TW Hya and older, coronally active sources. By determining the radius from radial velocity (v sin i) measurements and the rotation rate, Barnes et al. (2000) also find HIP 92680 to be young, since the radius determined is larger than the radius one would expect from a main sequence star with the same mass as HIP 92680. The Chandra high-resolution observation of HIP 92680 was previously analyzed by Argiroffi et al. (2004). They compare their results to the study of TW Hya by Kastner et al. (2002) and to the study of the zero-age main sequence star AB Dor by Güdel et al. (2001). They find the X-ray properties of HIP 92680 to be more similar to AB Dor than to TW Hya. For more details on the analysis by Argiroffi et al. (2004), see Chapter 4.

1.3.8 *V824 Ara C*

V824 Ara C is the closest star in our sample, at a distance of just 31 parsecs, and is a member of the Beta Pictoris moving group. It is a rapidly rotating post-TTS with a period of 1.68 days (Martin & Brandner, 1995). V824 Ara C is a companion to V824 Ara A and B, all three of which are classified as pre-main sequence stars due to their high Li abundances (Pasquini et al., 1991). In the triplet system, V824 A and B are a spectroscopic binary, and V824 C is widely separated from the pair by 33" (Schuetz et al., 2009). No evidence of mid-infrared excess emission has been detected toward

the V824 Ara system (Schuetz et al., 2009). V824 Ara C was previously studied by Ness et al. (2004) who find a plasma density of log n_e = 11.6 ± 0.13 for the star, which is consistent with plasma densities found in the other coronally active stars in their study.

1.3.9 *BO Mic*

BO Mic is the only main sequence (core hydrogen burning) star in our sample. It is a nearby star (44 parsecs) located in the Pleiades moving group (the Local Association) and is known to have an age greater than 20 and less than 150 Myr (Montes et al., 2001). BO Mic has an equatorial rotation velocity of v sin i = 128 km s^{-1}, which earned it the nickname "Speedy Mic." It is one of the most active stars in the solar neighborhood, has been known to flare, and has a coronal iron abundance that is subsolar, all of which are properties often found in observations of other active stars (Singh et al., 1999). Wolter et al. (2008) found, over a two day imaging observation of BO Mic, that the Hα EW varied from 4.4 to 5.4 Å. The changes in Hα correlate well with variations in X-ray flux over the same period, but correlate only weakly with changes in photospheric emission over that same period. Ness et al. (2004) were able to place an upper limit on the density of the X-ray emitting plasma in BO Mic by measuring the*f/i* ratio from the Chandra high-resolution spectra. They find the density to be log n_e <11.2 from the O VII He-like triplet, and log n_e <12.5 from the Ne IX He-like triplet.

Table I.1. Summary of Properties of Chandra HETG Observations in Sample

Star	Spectral Type	distance (pc)	Hα EW (Å)	Li (Å)	IR excess	Sub-mm excess	Environment
TW Hya	K8Ve	56	-220[1]	0.39[1]	yes[2]	yes[3]	disk + accretion
SU Aur	G2III	152	-5.0 ± 1.9[4]	...	yes[5]	yes[5,6]	disk + accretion
HD 98800	K4	47	0[1]	0.36[1]	yes[2]	...	disk, no accretion
V987 Tau	G2III	128	1.01 ± 0.14[4]	yes[7]	no[8]	yes[9]	cold disk, no accretion
DoAr 21	K0	160	-0.6[10]	...	no[11]	no[12]	gas disk, no accretion
Hen3-600	M3	34	-21.8[1]	0.53[1]	yes[2]		disk, accretion
HIP 92680	K0Vp	50	0.1[13]	yes[13]	no[14]	...	no disk, no accretion
V824 Ara C	M4.5	31	-6.2[15]	yes[7]	no[16]	...	no disk, no accretion
BO Mic	K0V	44	∼5.0[17]	...	no[18]	no[18]	no disk, no accretion

Note. — The basic properties of sources at different wavelengths as well as a summary of the circumstellar environment are listed. The spectral type and distance for each star were taken from X-Atlas (http://cxc.harvard.edu/XATLAS/). 1) Webb et al. (1999), 2) Weinberger et al. (2002), 3) Hughes et al. (2008), 4) Nguyen et al. (2009), 5) Akeson et al. (2002), 6) Sylvester et al. (1996), 7) Pasquini et al. (1991), 8) Furlan et al. (2006), 9) Andrews & Williams (2005), 10) Bouvier & Appenzeller (1992), 11) Barsony et al. (2005), 12) Andre & Montmerle (1994), 13) Soderblom et al. (1998), 14) Argiroffi et al. (2004), 15) Martin & Brandner (1995), 16) Schuetz et al. (2009), 17) Wolter et al. (2008), 18) Dunstone et al. (2006)

1.3.10 *Other stars studied with high-resolution X-ray spectroscopy*

BP Tau is a K5 cTTS that displays excess continuum emission at ultraviolet wavelengths (Bertout et al., 1988). Optical variability has been observed in BP Tau but differs from the optical variability seen in typical flare stars. The slow, smooth observed changes in the optical and ultraviolet are thought to be the result of inhomogeneous accretion from the disk to the stellar surface (Gullbring et al., 1996). Schmitt et al. (2005) analyze the XMM-Newton high-resolution spectrum of BP Tau and find a weak detection of the O VII forbidden line, similar to that observed in TW Hya. They also note an absence of strong emission in the iron lines at 15 Å and 17 Å. They conclude that BP Tau shows evidence for X-ray emitting plasmas at two different temperatures. They interpret the low-temperature component of the X-ray emission as due to an accretion shock and the higher temperature hot plasma component as due to either magnetic coronal activity or magnetic interactions between the corona and the disk.

CR Cha is a K2 cTTS in the Chamaeleon star forming region. Robrade & Schmitt (2006) find again a low f/i ratio, though with a large error in the measurement. They calculated the G ratio, $((f+i)/r)$ (see Section 3.1.1 for more details), to be 2.9 ± 2.2. The error in the measurements of f, i, and r, which in turn lead to a large error in the value of G, may be due to strong interstellar absorption (2.7×10^{21} cm^{-2}; Gauvin & Strom (1992)).

1.4 Summary

Though several high-resolution X-ray studies of young stars have been conducted, no clear picture has yet emerged of robust X-ray signatures that correlate to the physical mechanisms producing the various X-ray emitting plasma. The analyses of the X-ray spectra of the nine stars described in sections 1.3.1 through 1.3.9, which are presented in this dissertation, have been done in a globally consistent fashion, in order to determine if there are observational X-ray characteristics that correlate with the evolutionary status, as determined by observations at other wavelengths.

CHAPTER II

IMAGING SPECTROSCOPY OBSERVATIONS

2.1 The Chandra X-ray Observatory

The Chandra X-ray Observatory (CXO), launched into a high-earth orbit in 1999, is a world-class X-ray observation facility, with which much of the data for this dissertation was obtained. The observatory has a mirror consisting of four pairs of nested reflecting surfaces. The surfaces are coated with iridium and reflect incoming X-rays at grazing angles. The photons are then detected by one of two focal plane instruments, the High Resolution Camera (HRC) and the Advanced CCD Imaging Spectrometer (ACIS). In addition, there are two sets of transmission gratings, each optimized for different energy ranges, the Low Energy Transmission Grating (LETG) and the High Energy Transmission Grating (HETG). Chandra can achieve a spatial resolution of about one arcsecond and is sensitive to X-rays in the 0.1 to 10 keV (120-0.12 Å) range. Because it is in an elliptical orbit, Chandra can observe over long, uninterrupted integration times. This, combined with its sensitivity, allows for the observation of faint X-ray sources.

Two instruments aboard Chandra are particularly conducive to observing young stars. ACIS has the capability of obtaining imaging and spectroscopic data. In many cases, the incident X-ray flux is low enough that only one X-ray photon will be detected for every 100 or more pixels sampled, yielding a relatively high energy resolution $E/\Delta E \sim 50$ (Chartas et al., 1998). ACIS has four imaging chips (ACIS-

I) and six spectroscopic chips (ACIS-S). Each chip has a pixel size of 0.49" and a field of view of ∼8' × 8'. The ACIS-I3 and ACIS-S3 chips are back-illuminated, which allows for increased sensitivity to X-rays in the 0.3 - 10 keV range. The High Energy Transmission Grating Spectrometer (HETGS) can be placed between the incoming X-rays and ACIS (Canizares et al., 2005). HETGS utilizes gold transmission gratings just behind the mirrors that disperses the incident X-rays. Using HETGS in conjunction with ACIS, one is able to achieve an energy resolution of E/ΔE of ∼100 to ∼1000 (Chartas et al., 1998). This allows for the identification of individual X-ray emission lines that can be measured and used to determine temperature, ionization levels, and composition. Analysis techniques of HETGS data will be discussed in Chapter 3.

2.2 Observations and Data Processing

High angular resolution imaging observations of binary T Tauri systems can be done with CXO/ACIS and such observations have the potential to make a major contribution to solving the puzzles as to how T Tauri stars produce X-rays. We carried out a study of one close binary T Tauri system, V710 Tau, with ACIS. The results presented here were published in Shukla et al. (2008).

Images of the binary T Tauri system V710 Tau were taken by Chandra on 29 December 2004 (ObsID 5425; 9043 s exposure) and again on 4 April 2005 (ObsID 5426; 8976 s exposure). For each observation the target was positioned on the back-illuminated CCD S3 (ACIS-S3). The photon event data were processed using the standard Chandra data processing pipeline, CIAO, version 3.2. Circular spectral

extraction regions of radius 1.66" that encompass each source individually, without significant overlap, were defined. Similarly, using four circular regions, each of radius 5.0", the background flux level centered about the binary system was defined. Since the background flux level was taken from the area surrounding the binary system, the same background regions were used for both stars in each observation. Using these regions, background-subtracted spectra were extracted using the CIAO psextract science thread[1]. The data were further processed utilizing CCD subpixel event repositioning (SER) techniques, designed to optimize Chandra/ACIS spatial resolution (Li et al., 2003). The improved ACIS-S3 images obtained after SER processing more clearly resolve the binary but do not affect the outermost portions of the point spread functions (PSFs) of the two stars where the PSFs overlap. Hence, spectral analysis (section 3.2) was performed on the event data prior to SER processing.

2.3 Results

2.3.1 *ACIS-S3 Multiepoch Imaging and Light Curves*

As is evident in Figure 2.1, the Chandra images cleanly resolve the X-ray binary system and demonstrate that both V710 Tau N and V710 Tau S are sources of X-rays. These X-ray data (see count rates in Table II.1) reveal that the cTTS is the brighter X-ray source of the pair in December 2004 and that the two stars were nearly equal in X-ray brightness in April 2005.

ACIS measures the number of X-ray photons that strike a pixel at a particular energy. The data is recorded in an *events list*, which contains the (x,y) position,

[1]http://cxc.harvard.edu/ciao/

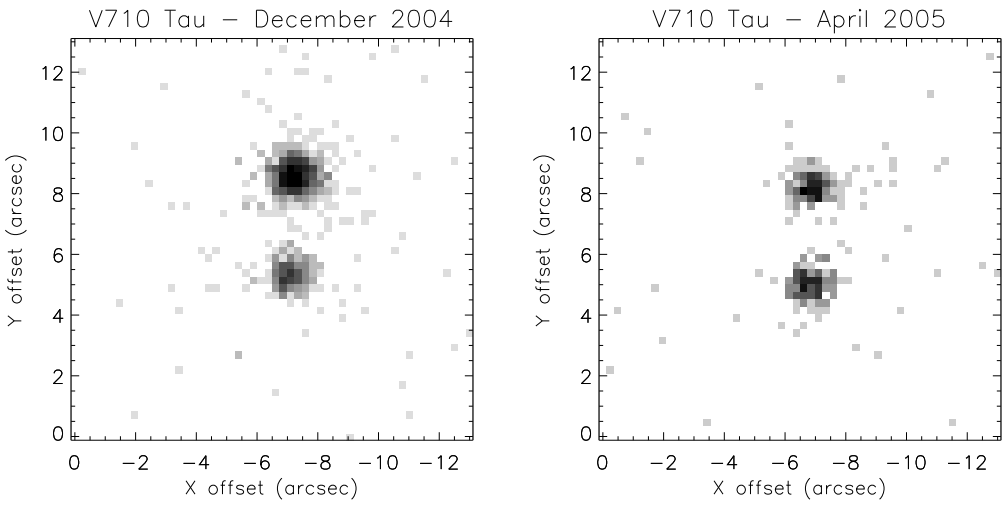

Figure 2.1: Chandra/ACIS-S3 X-ray images of the V710 Tau binary (3.17" separation) obtained 2004 December (left) and 2005 April (right). The grey-scale ranges of the images peak at 5.75 counts $ks^{-1}pixel^{-1}$ (December 2004) and 1.78 counts $ks^{-1}pixel^{-1}$ (April 2005).

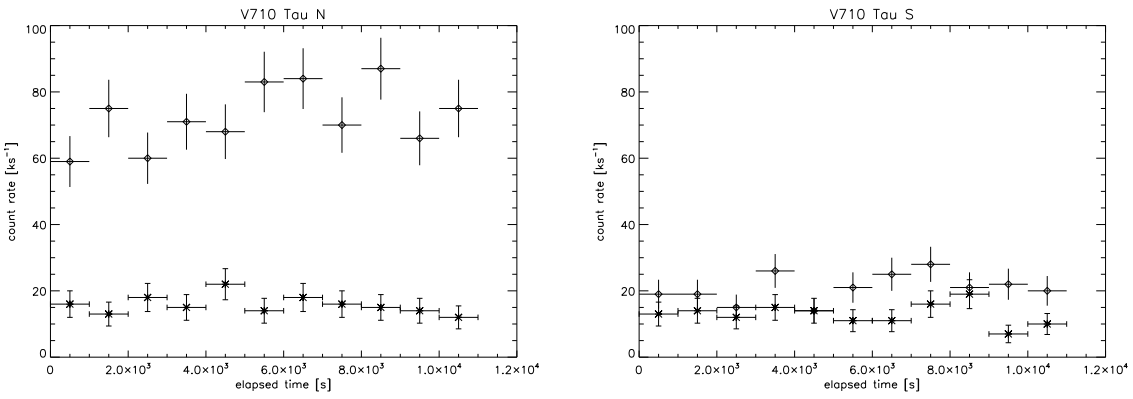

Figure 2.2: Light curves for V710 Tau N (left) and V710 Tau S (right) in December 2004 (diamonds) and April 2005 (crosses). Horizontal error bars indicate the width of the time bins (1000 s), and the vertical error bars indicate 1 σ uncertainties in count rate per 1000s time interval.

energy, and time of each photon as it strikes a pixel. The *count rate* of a particular observation are simply the number of X-ray photons detected per second. Count rates do not account for the energy of a particular photon, but only to the energy bin, either soft, or low-energy photons, or hard, higher energy photons. For our data, we calculated count rates for three distinct energy bins, optimized for the range of energies detected by ACIS in our data.

Within each 9 ks exposure, both stars appear to have nearly constant count rates (Table II.1, Figure 2.2), although, within the 3σ uncertainty range, the X-ray count rates may vary by as much as a factor of two on a 1 ks timescale. However, the count rates of both stars were larger in December 2004 than in April 2005. Specifically, the average X-ray count rate of V710 Tau S was $\sim$1.5 times greater in December than in April, while the X-ray flux of V710 Tau N was $\sim$5 times larger in the first-epoch observation. In addition, the ACIS hardness ratios (HRs) for the binary were calculated for the total counts over each observation according to the HR definitions in Getman et al. (2005) as HR = $(Cts_h - Cts_s/(Cts_h + Cts_s)$, where "h" and "s" refer to a harder and softer band respectively. Since our data had no counts beyond 5.0 keV, we used this as our upper energy cutoff as opposed to 8.0 keV used for the COUP sources. For HR1, the common definitions of s = 0.5-2.0 keV and h = 2.0-5.0 keV were used. In order to highlight the softer part of the spectrum HR2 is defined as s = 0.5-1.7 keV and h = 1.7-2.8 keV. Similarly, HR3 is defined with s = 1.7-2.8 keV and h = 2.8-5.0 keV to exemplify the harder portion of the spectrum. From the hardness ratios, one can determine what range of energies are primarily responsible for the X-ray flux at a given time. These ratios demonstrate that the emission from

Table II.1. Hardness Ratios

Observation	count rate cnts/ks	HR1	HR2	HR3
V710 Tau N (Dec)	74.3 ± 2.6	-0.66 ± 0.04	-0.64 ± 0.04	-0.39 ± 0.08
V710 Tau N (Apr)	15.3 ± 1.2	-0.83 ± 0.10	-0.82 ± 0.10	-0.56 ± 0.32
V710 Tau S (Dec)	23.8 ± 1.5	-0.94 ± 0.09	-0.91 ± 0.09	-0.60 ± 0.36
V710 Tau S (Apr)	14.8 ± 1.2	-0.96 ± 0.11	-0.94 ± 0.11	-1.00 ± 0.78

Note. — The hardness ratios were calculated as defined in Getman et al. (2005). HR3 of V710 Tau S in April is attributed to lack of counts in the hardest range. Errors for observations with low counts were estimated according to Gehrels (1986).

V710 Tau N was harder in the first observation than in the second. In contrast, the HRs of V710 Tau S remained constant to within the uncertainties, and its overall X-ray emission was somewhat softer than that from V710 Tau N, especially in December 2004 (Table II.1). Stelzer et al. (1999) define a flare as "whenever consecutive time bins are observed to build a rising or falling sequence of count rates and they deviate significantly (more than 5 σ) above the mean quiescent emission." By this definition, these data suggest that V710 Tau N was in a flaring state during the first observation, whereas V710 Tau S displayed less significant, if any, long-term flaring.

2.3.2 *Spectral Analysis*

Spectral analysis was performed with the X-ray data analysis tool XSPEC, version 11.3.1 (Arnaud, 1996). The spectral data in the region of 0.3 to 5.0 keV (essentially

no photons were detected from 5 to 10 keV) were fit with the MEKAL code describing thermal, collisionally excited plasmas (Mewe et al., 1985, 1986; Liedahl et al., 1995); the VMEKAL code, in which metal abundances can be adjusted individually; and the APEC code describing optically-thin plasmas in collisional ionization equilibrium(see section 3.1.1) (Smith et al., 2001). The intervening photoelectric absorption is incorporated through the WABS model (Morrison & McCammon, 1983). We find that the APEC and MEKAL model fits do not differ significantly; thus we only report the analysis performed with the MEKAL and VMEKAL models.

For each of the two observations of each component of the V710 Tau binary (hereafter denoted as N1 and S1 for the December 2004 and N2 and S2 for the April 2005 observations of the northern and southern components, respectively), we fit the X-ray spectrum with a thermal plasma model suffering intervening absorption. White & Ghez (2001) measure the visual extinction, A_V, for V710 Tau N and V710 Tau S to be 1.80 $\pm$ 0.36 and 1.82 $\pm$ 0.51 respectively. Hence, adopting the hydrogen column density conversion of Vuong et al. (2003), $N_H = 1.6 \times 10^{21} A_V$, we use the optically-derived value of $N_H = 0.29 \times 10^{22}$ cm^{-2} for our spectral modeling. Allowing N_H to vary underconstrains the model fitting and does not produce meaningful results for the model parameters. Previous studies (e.g., Giardino et al. (2006) and references therein) have found that plasma models with subsolar elemental abundances better reproduce the X-ray spectra of T Tauri stars than do models that assume solar abundances. We assume a subsolar abundance of $Z = 0.2\ Z_\odot$, which is nearly identical to the abundance value found for the combined spectrum of V710 Tau by Favata et al. (2003). Indeed, we find that single-component MEKAL plasma models provide

reasonable fits for all four spectra (Figures 3-5).

For the spectrum with the best signal-to-noise ratio, obtained from observation N1, we find that a two-component model improves the spectral fit significantly in comparison to a one-component model (Table II.2). A two-component model with both a cooler plasma component ($kT_1 \sim 0.5$ keV) and a hot plasma component ($kT_2 \sim 2.6$ keV) provides an improved fit, especially at energies below ~ 1 keV (Fig. 3). However, while such two-component models also provide adequate fits for the spectra resulting from observations N2, S1, and S2, we are unable to constrain the model normalizations, and thus the emission measures, for these three spectra. It therefore appears that three of the four observations of V710 Tau N and V710 Tau S are reasonably well-characterized by single-component, low-temperature ($kT \sim$ 0.7-1.1 keV) plasma models (Table II.2), whereas both the one- and two-component plasma models point to the presence of a dominant higher-temperature plasma ($kT \sim$ 2.1-2.6 keV) during the apparent flare on V710 Tau N captured in observation N1.

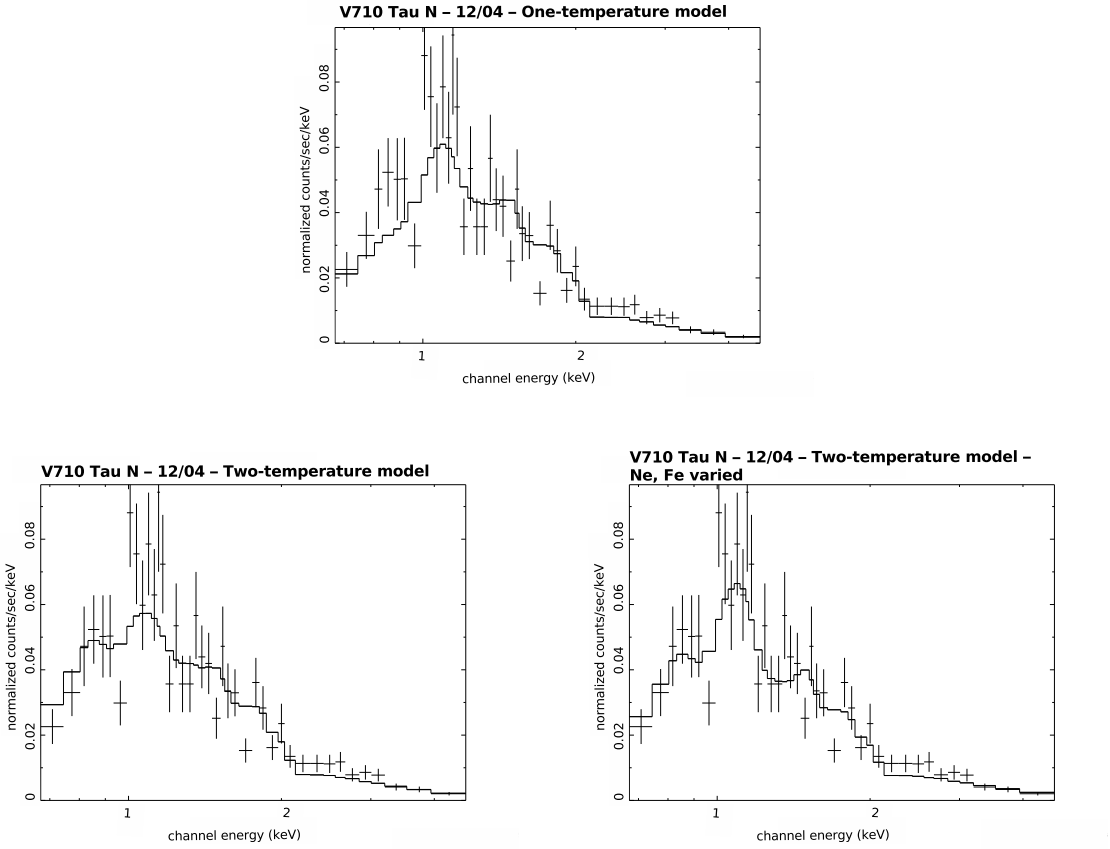

Figure 2.3: The model fits are a one-temperature plasma WABS(MEKAL)(top), two-temperature WABS(MEKAL)(bottom, left), and two-temperature WABS(VMEKAL) (bottom, right). The corresponding model parameters are listed in Table II.2. A two-temperature model (bottom panels) is needed to fit low-energy data points in the region < 1.0 keV. Note the improved fit in the $\sim 1.0 - 1.5$ keV range in the bottom right panel. The WABS(VMEKAL) (bottom right) model has a Ne abundance of 0.72 ± 0.92 $Z_\odot$ $Z_\odot$ and a Fe abundance of 0.54 $\pm$ 0.30 $Z_\odot$ (all other elements at Z = 0.2 $Z_\odot$), which slightly improves the fit in the region around 1 keV.

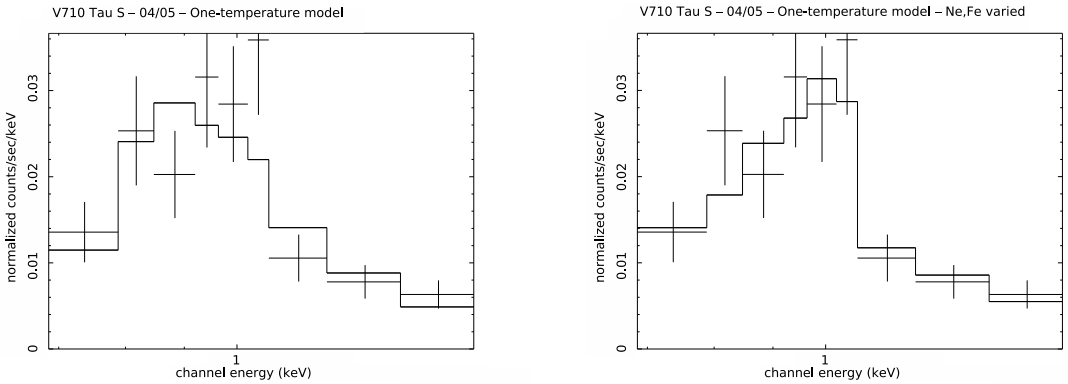

Figure 2.4: Single-temperature WABS(MEKAL) model with subsolar abundances (left) and a WABS(VMEKAL) model (right) with a Ne abundance of 0.78 $\pm$ 0.55 $Z_{\odot}$. The VMEKAL model provides a better fit at almost all energies.

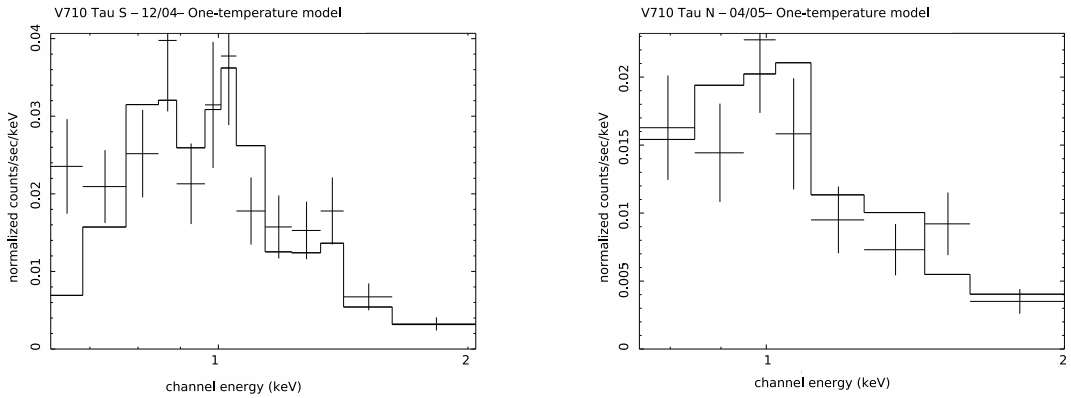

Figure 2.5: Single-temperature WABS(MEKAL) model fits for V710 Tau S, December 2004 (left) and V710 Tau N, April 2005 (right).

High-resolution X-ray spectroscopy of cTTS and wTTS (e.g., Kastner et al. (2002, 2004)) show that X-ray emitting plasmas in T Tauri stars exhibit a range of temperatures and strong abundance anomalies, in particular, enhanced Ne. To investigate whether the T Tauri stars in the V710 Tau binary display such anomalies, we performed spectral fits with VMEKAL models, in which individual abundances can be varied. Given that the two-temperature MEKAL models had unconstrained emission measures for N2, S1, and S2, we attempted fits of one-temperature plasma VMEKAL models to these spectra, with Ne and Fe allowed to vary. All other metal abundances were set to 0.2 $Z_{\odot}$. The single-component VMEKAL model slightly improves the fit for the S2 observation (Figure 2.4), however there is no improvement for S1 and N2 (Figure 2.5). A two-component VMEKAL model with an enhanced Ne abundance significantly improves the fit for the N1 observation, particularly in the $\sim 1-1.5$ keV spectral region (Figure 2.3). We find both Ne and Fe to be slightly overabundant

Table II.2. Model parameters and results

Obs.	Model	$F^1_{X,abs.}$ $(10^{-13}$ erg cm^{-2}s$^{-1})$	$L^2_{X,intr.}$ log (erg s^{-1})	kT_1 (keV)	kT_2 (keV)	EM^2_1 (10^{53} cm^{-3})	EM^2_2 (10^{53} cm^{-3})	d.o.f.	χ^2
N1	1T-MEKAL	3.16 - 3.67	$29.9^{+1.07}_{-1.19}$	2.13 ± 0.18	...	1.47 ± 0.12	...	39	1.77
N1	2T-MEKAL	3.11 - 3.75	$29.9^{+1.31}_{-0.89}$	0.51 ± 0.27	2.64 ± 0.38	0.30 ± 0.18	1.25 ± 0.21	37	1.67
N1	2T-VMEKAL	3.09 - 3.80	$29.9^{+1.23}_{-0.86}$	0.50 ± 0.19	3.15 ± 0.59	0.12 ± 0.12	1.40 ± 0.29	35	1.59
N2	1T-MEKAL	0.41 - 0.58	$29.08^{+0.85}_{-0.72}$	1.01 ± 0.087	...	0.31 ± 0.06	...	6	1.16
S1	1T-MEKAL	0.69 - 0.95	29.28 ± 0.81	0.76 ± 0.054	...	0.56 ± 0.08	...	11	2.3
S2	1T-MEKAL	0.48 - 0.65	$29.13^{+0.84}_{-0.82}$	0.78 ± 0.065	...	0.42 ± 0.07	...	7	1.12
S2	1T-VMEKAL	0.22 - 0.60	$29.10^{+0.05}_{-0.38}$	0.58 ± 0.21	...	0.61 ± 0.63	...	5	0.89

Note. — N_H was set to the optically-derived value of 0.29 x 10^{22} cm^{-2}. 1) The absorbed X-ray flux ranges are based on 68% Bayesian confidence ranges. 2) $L_{X,intr.}$ and emission measure (EM) were computed assuming a distance of 140 pc to the V710 Tau system.

with respect to the nominal abundances, though the precise values are very uncertain due to poor photon counting statistics. Given the spectral resolution of the CCD data, we are unable to discern whether Ne IX or Ne X, the dominant ions in the high-resolution spectra of accreting stars, is primarily responsible for the excess emission. However the abundances from the VMEKAL fitting suggest that the Ne/Fe ratio may be enhanced in the X-ray emitting plasma for V710 Tau N during the flare event.

CHAPTER III

HIGH RESOLUTION X-RAY SPECTROSCOPY OBSERVATIONS

3.1 Background

While many of the X-ray studies of young stars have been done with low resolution X-ray data, the results from these studies are largely statistical (see Chapter 2). Very high spectral resolution X-ray data are necessary in order to more thoroughly characterize the X-ray emission from individual stars. The high-resolution spectrometer instrument aboard the Chandra X-ray Observatory enables observers to resolve and measure individual emission lines from various highly ionized elements present in many astrophysical objects. Using the spectral line measurements, we are able to model the X-ray emission from young stars and correlate properties of X-ray emission with physical processes ongoing in young stars.

Utilizing high-resolution data from Chandra, line fluxes of highly ionized elements can be measured and used to derive temperatures, densities, and elemental abundances of the X-ray emitting plasmas. These characterizations can shed light on the mechanisms that generate X-rays from young stars and may lead to discovery of key characteristics that can be used to better understand the processes by which stars form. The current nature of the physical environment, such as the presence of a circumstellar disk and evidence for the level of accretion activity, of each of these stars has been determined over the last several decades primarily through optical and infrared observations. Often, the nature of the physical environment is taken as equiv-

alent to evolutionary status (i.e., pre-main sequence stars are born with thick massive disks; as they mature, the disks disperse or dissipate). By measuring the line emission from each star, it is possible to characterize the X-ray emission from stars in different physical environments and therefore perhaps at different evolutionary epochs.

High resolution spectroscopic studies of young stars at high energies are uncommon since such observations are limited to stars that are "strong" emitters of X-rays. Even for young X-ray bright stars, large investments of observing time with Chandra are needed since the X-ray brightest T Tauri stars are still faint in X-rays when compared to other high energy and temperature astrophysical phenomena such as neutron stars and active galactic nuclei. Currently, only two instruments are capable of such observations, the Reflection Grating Spectrometer (RGS) on the X-ray Multi Mirror telescope (XMM-Newton, a European Space Agency mission) and HETGS on Chandra. Of these, HETGS has the highest spectral resolution over a larger wavelength range. These instruments are the first to obtain high-resolution X-ray spectra from objects beyond our solar system, providing data to which astronomers are able to apply X-ray plasma diagnostics.

3.1.1 *Theory of X-ray emission lines*

Hot plasmas in collisional ionization equilibrium (CIE) are the dominant source of X-ray emission from young stars. Assuming a plasma is in CIE implies that the plasma is optically thin to its own radiation, such that radiative excitations can be neglected and collisional processes are the dominant excitation mechanisms. The de-excitation process is radiatively dominated. Collisional excitation of the first excited state (n=2)

from the ground state of highly ionized species is the primary means of producing X-ray emission lines (Porter & Ferland, 2007). Since these plasmas are typically hot and rarefied, forbidden transitions are normally allowed. Forbidden transitions, as the name implies, are forbidden since the probability of a forbidden transition is much lower than for a permitted transition in the electric dipole approximation. At high densities, like those observed on Earth, an electron excited to an upper (forbidden) energy level has a very low probability of radiatively decaying to a lower energy state and will likely decay due to a collision. In rarefied plasmas, however, the densities are so low that collisions are rare. As a result, electrons are able to radiatively decay to lower energy levels, which allow us to observe radiation in "forbidden" emission lines. Thus, observation and analysis of forbidden lines can be used as a diagnostic of plasma density.

Atoms in X-ray emitting plasmas are highly ionized. *Hydrogen-like* ions have one valence electron (e.g., neon stripped of nine of its ten electrons is H-like, and is designated as Ne X) and *Helium-like* ions have two valence electrons (e.g., neon stripped of eight electrons is He-like and is designated as Ne IX). Gabriel & Jordan (1969) first showed how ratios of the intensities of various lines involving transitions between the n=2 and n=1 levels of He-like ions could be used to measure temperatures and densities in collisionally ionized plasmas. In CIE plasmas, the electron kinetic energy is roughly equal to the ionization potentials of the species that are present (Porter & Ferland, 2007). The He-like emission lines are observed in "triplets" of resonance, forbidden, and intercombination lines.

The resonance line is the line of longest wavelength associated with a transition

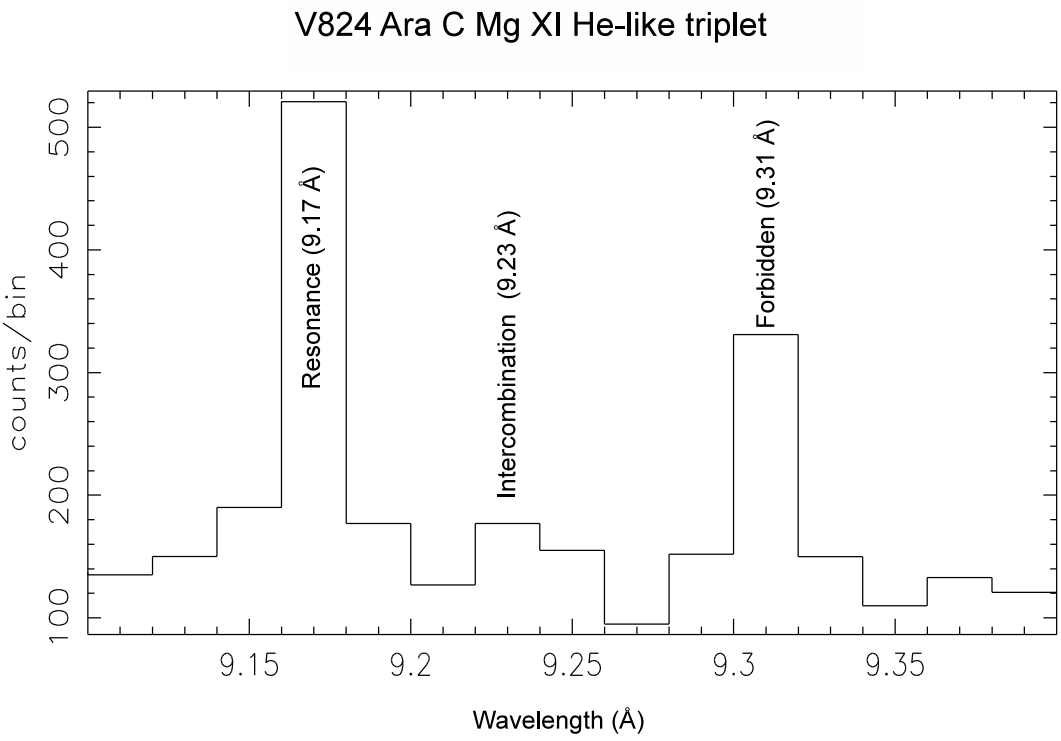

Figure 3.1: He-like triplet showing the r, i, and f lines of Mg XI in the spectrum of V824 Ara C.

between the ground state and an excited state and always has the highest energy (and shortest wavelength) of the three lines in the triplet (Figure 3.1). The intercombination line is defined as the line emitted in a transition between energy levels that have different values of the total spin quantum number; it is always intermediate in energy and wavelength between the r and f lines. Forbidden line transitions occur when an electron moves from a metastable state to a lower energy level and are the lowest energy and longest wavelength line in a given triplet. These three lines correspond specifically to the following transitions:

- resonance line (r): $1s^2\ ^1S_0\ -\ 1s2p\ ^1P_1$
- intercombination line(s) (i): $1s^2\ ^1S_0\ -\ 1s2p\ ^3P_{2,1}$
- forbidden line (f): $1s^2\ ^1S_0\ -\ 1s2s\ ^3S_1$

In He-like ions, electron-nucleus and electron-electron Coulomb interactions are not the only contributing sources to the energy structure. Therefore, one can have multiple levels with the same principle quantum number. The separations of these levels are determined by direct and exchange electrostatic interactions between electrons. These conditions allow for the combination of S, the total spin angular momentum of the electrons, and L, the total orbital angular momentum, into the total angular momentum, J (J = S + L). Atomic states that have the same electron configuration but different values of L and S have different energies. Thus, in addition to the electron term, (e.g., $1s^2$), we can describe the notation of the resonance, intercombination, and forbidden lines of a He-like ion in terms of a spectroscopic "term," $^{2S+1}$L, where

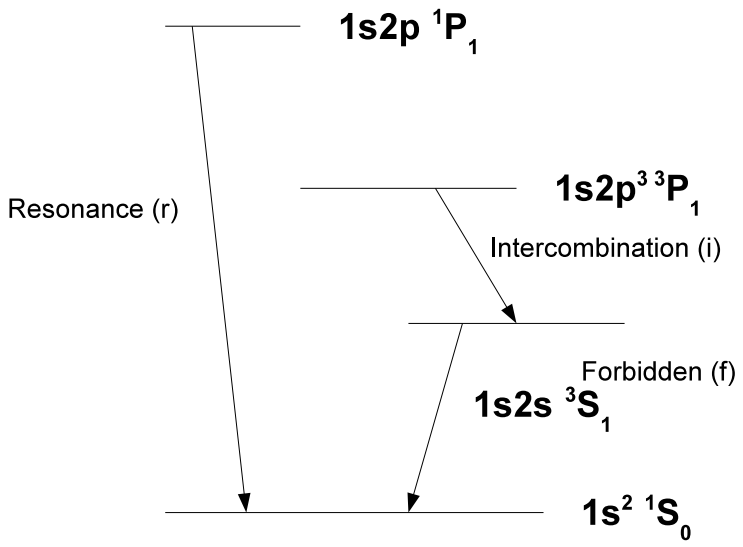

Figure 3.2: Simplified diagram of the resonance, intercombination, and forbidden lines of a He-like triplet (Ness et al., 2002b)

the quantity 2S+1 is known as the multiplicity. When L and S are coupled (i.e., the vector sum is taken), then the level can be denoted as $^{2S+1}\mathrm{L}_J$. The spectroscopic term, L, is defined as S, P, D, F and so on (0, 1, 2, 3 etc.). So, the resonance and intercombination lines have the same transition between electron terms, but different spectroscopic terms ($^1P_1$ for the resonance line, and $^3P_{2,1}$ for the intercombination lines (one with a J=1, one with a J=2). The forbidden line has a different electronic and spectroscopic configuration than the resonance and intercombination lines. The levels of these lines are illustrated in Figure 3.2.

Measurements of these He-like triplet line fluxes can be used to calculate ratios

sensitive to temperature and density. These ratios were first developed as diagnostics for solar plasmas by Gabriel & Jordan (1969). The R ratio, defined as R = f/i where f and i are the line fluxes of the forbidden and intercombination lines respectively, is considered a density diagnostic, with the value of R inversely correlated with electron density (n_e). At higher densities, the value of R decreases, since fewer forbidden transitions are observed. If the strength of the forbidden line is much stronger than the strength of the intercombination line, the R ratio implies a low density and gives an upper limit for n_e. Conversely, a low value for the R ratio implies a high density and yields a lower limit for n_e (Porquet, 2005). Therefore, in order to probe a particular density regime, the value of the R ratio must be of order one, indicating a n_e in the range of the critical density for a given ion. Different ions probe different density regimes, as demonstrated in Figure 3.3.

The G ratio, which is considered a temperature diagnostic, is defined as G = $(f+i)/r$ and is sensitive to temperature since the collisional excitation rates do not have the same dependence on temperature for the resonance line as for the forbidden and intercombination lines (Porquet, 2005). The G ratio is inversely proportional to the temperature; as the estimated temperature of the X-ray emitting plasma increases, the value of r (i.e., the strength of the resonance line) increases relative to the combined strengths of the f and i lines, and consequently the value of the G ratio decreases. Thus, the G ratio is inversely proportional to effective temperature due to the different effective temperature distributions of collisional excitation rates (Porquet, 2005).

These three lines are very useful as density diagnostics for several reasons. Since

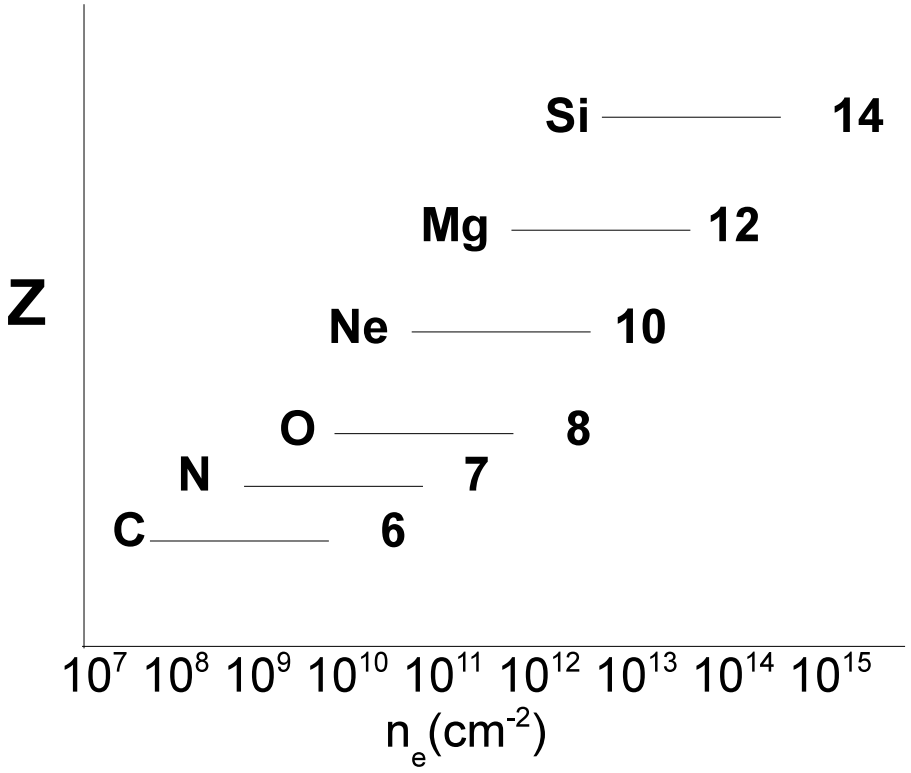

Figure 3.3: Each He-like triplet probes different densities of X-ray emitting plasmas. The atomic number, Z, is indicated to the right of the density range of each ion.

the emission of all three lines come from the same ion, the line fluxes do not depend on differences in abundances. He-like ions are stable over large temperature ranges, and each set of He-like ions (e.g., Si XIII, Ne IX) is sensitive in a particular density and temperature regime, making them ideal diagnostics for probing different plasmas. The densities are inferred from the formula given in Equation 1, where n_e is the electron density, R_0 is the low-density limit (for which n_e=0), ϕ/ϕ_c is the radiation term, and N_c is the electron density at which the R ratio reaches half of its low-density value (Pradhan & Shull, 1981; Ness et al., 2002a, 2004). The radiation term, ϕ/ϕ_c, describes the influence of external radiation fields, where ϕ is related to the ultraviolet flux in the line emitting region, and ϕ_c is dependent on the electron temperature for a given ion.

$$\frac{f}{i} = \frac{R_0}{1 + \phi/\phi_c + n_e/N_c} \tag{3.1}$$

Generally, it is assumed that the excitation from the *f* level to the *i* level is purely collisional and thus the radiation term can be ignored. In some cases, for instance when there is intense UV radiation from the stellar surface, photons with the right energy can cause excitation from the forbidden to intercombination states. It is therefore important to be aware that for low-Z ions (e.g., C, N, O), the forbidden and intercombination lines are sensitive to UV radiation, and if the radiation term is ignored, a falsely high plasma density may be inferred. The ions used in our analysis (Ne, Mg, Si, S, Fe) have high enough Z values such that we can ignore the influence of ultraviolet radiation.

3.2 Instrumentation and Software

The High Energy Transmission Grating has 336 gold grating facets on a movable assembly that can be placed behind the mirrors on Chandra. The grating consists of both a high-energy grating (HEG) and a medium-energy grating (MEG). The grating spacing is 2000 Å for HEG and 4000 Å for MEG. The HETGS gratings are designed to detect X-rays in the energy range from 0.4 to 10 keV. The HEG and MEG gratings are sensitive to slightly different energy ranges (0.4-5.0 keV for MEG and 0.8-10.0 keV for HEG) and are oriented at slightly different angles. X-rays diffracted by the gratings are detected by the Advanced Charge-Coupled Device Imaging Spectrometer (ACIS). Both the resolution of the ACIS detector and the sharp mirror focus of ACIS allow for high-resolution X-ray spectroscopy. The HEG can achieve a spectral resolution of ~ 0.012 Å, and the MEG can achieve a spectral resolution of ~ 0.023 Å.

The specific software package, the Interactive Spectral Interpretation System (ISIS), used by X-ray astronomers to analyze HETGS data was developed by Houck & Denicola (2000). ISIS is specially designed to facilitate the analysis of high resolution grating spectrographs. ISIS also provided an interaction with a database of atomic structure parameters (the Astrophysical Plasma Emission Database, APED) and plasma emission models (the Astrophysical Plasma Emission Code, APEC) (Smith et al., 2001).

Chandra records the position, energy/wavelength, and arrival time of each photon detected by the CCD in a file known as the photon event file. We extracted spectra for each of the stars in our sample from photon event files in the Chandra X-ray

Observatory web archives using CIAO version 3.2. For each observation, we extracted plus and minus first order spectra of both HEG and MEG. We combined the data in such a manner that we could read the individual instrumental response files for each order. The combined spectra were used for the analysis we report for these stars. The full HETGS spectra for each observation are shown in Figure 3.4. Figure 3.5 shows the full spectrum of V824 Ara C with the strongest emission lines noted and described in the figure caption.

3.3 Light Curves and Temporal Analysis

We have analyzed high-resolution Chandra ACIS-S/HETGS long integration spectra for a sample of nine young stars, including two classical, four weak-lined, and two post-T Tauri stars as well as one young main-sequence star. The sample stars are listed in Table III.1 along with the exposure times for each observation. The light curves, which depict changes in the X-ray count rate over time, are plotted in the panels of Figures 3.6 and 3.7.

Our continuous observations spanned about 10 hours (36 ks) to 30 hours (108 ks). Over integration periods of tens of hours, many active stars will flare, and thus it is necessary to note any change in overall X-ray luminosity for the duration of each observation. X-ray flares are often diagnosed by a sudden increase in X-ray luminosity to several times the level of X-ray emission during quiescence (Favata et al., 2005). The hard X-ray flux (H) in particular rises rapidly during a flare and is sometimes accompanied by a change in soft X-ray flux (S). For this study, hard X-rays are defined as X-rays produced in the range of 1.5 to 8 Å and soft X-rays in

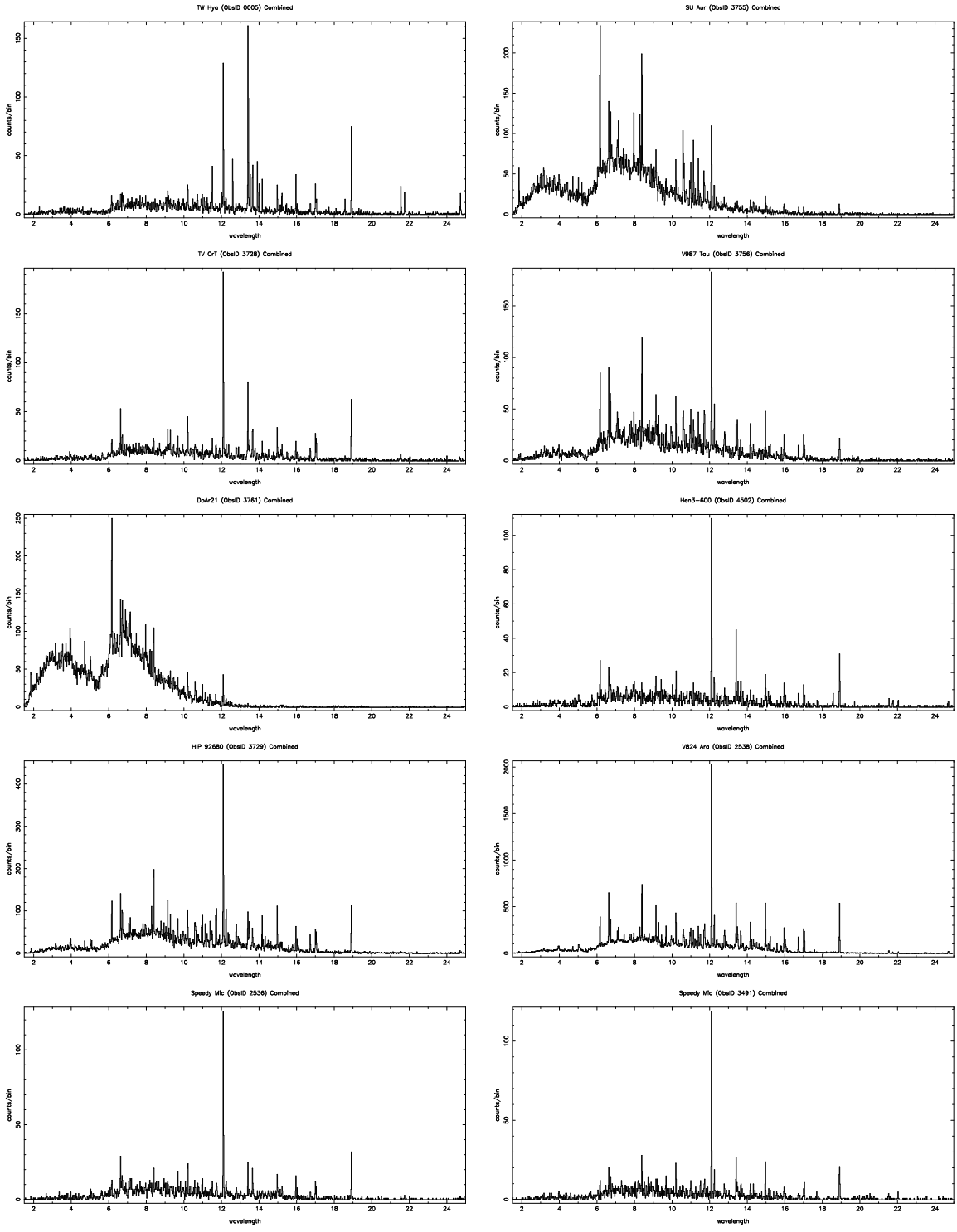

Figure 3.4: Each panel depicts a full spectra for all of the observations listed in Table III.1. Each spectra is shown over a wavelength range of 1.5 - 25 Å. The y-axis for each panel is in counts/bin and is optimized for each observation. From left to right, the observations and maximum count rates are TW Hya (160), SU Aur (260), HD 98800 (90), V987 Tau (180), DoAr 21 (250), Hen 3-600 (110), HIP 92680 (440), V824 Ara C (2000), BO Mic 1 (120), BO Mic 2 (120). The most prominent line in each spectra is the Ne X H-like Lyα line.

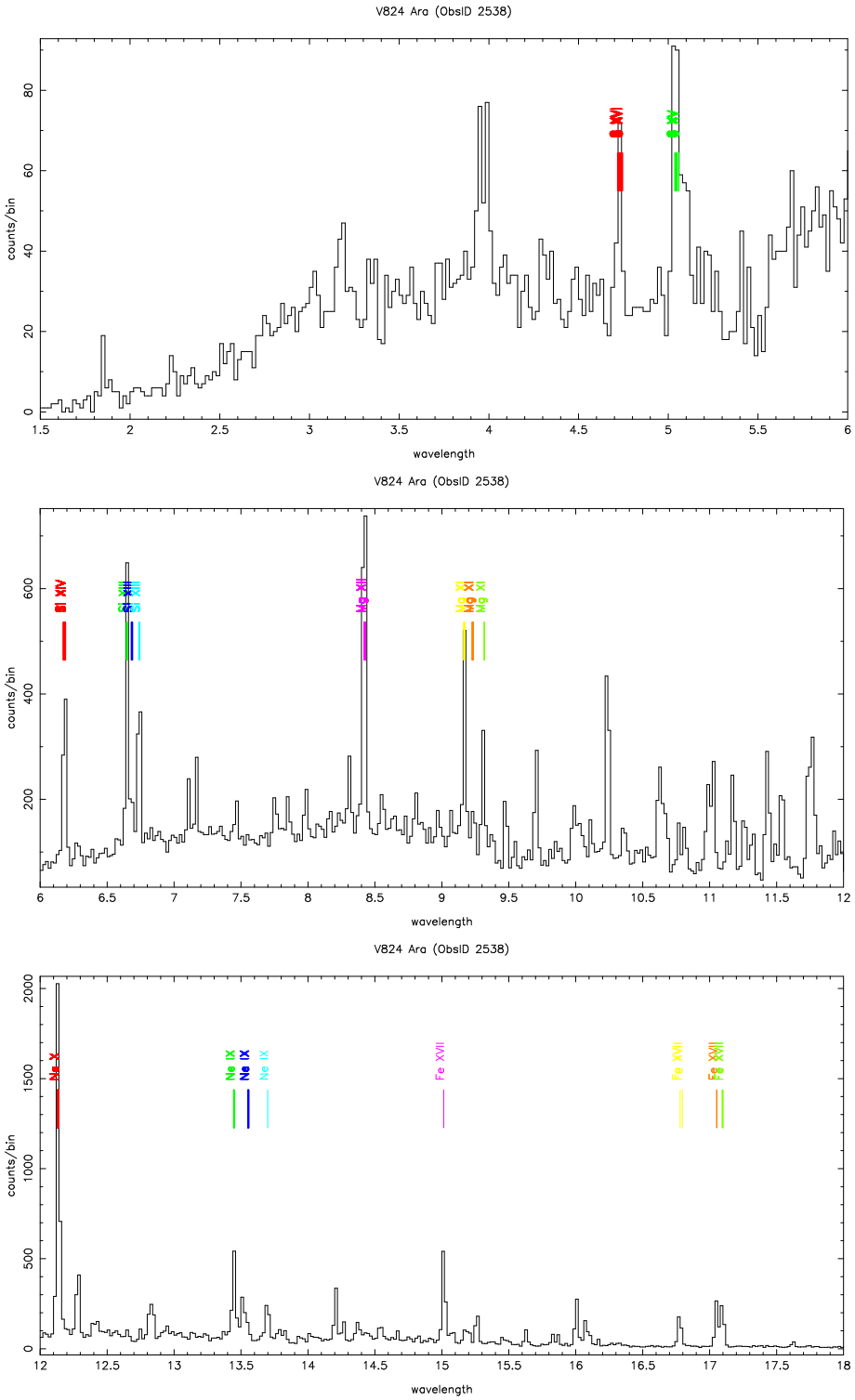

Figure 3.5: These three panels show the full spectrum from 1.5 - 18 Å of V824 Ara C, the brightest X-ray source in our sample. The lines used in our study are noted; from left to right these are S XVI (4.73 Å), S XV (5.04 Å), Si XIV (6.18 Å), Si XIII (6.65 Å, 6.69 Å, 6.74 Å), Mg XII (8.42 Å), Mg XI (9.17 Å, 9.23 Å, 9.31 Å), Ne X (12.14 Å), Ne IX (13.45 Å, 13.55 Å, 13.70 Å), and Fe XVII (15.01 Å, 16.78 Å, 17.05 Å, 17.09 Å).

the range of 8 to 18 Å. This type of flare event is usually followed by a slower, often exponential, decay back to the quiescent luminosity (Favata et al., 2005). For each star in our sample, the light curves for the full observation were produced using the ISIS script *aglc* (Huenemoerder, 2007). Hardness ratios are defined as (H - S)/(H + S), where H corresponds to the number or count rate of higher energy photons and S refers to the number or count rate of lower energy photons. Changes in these ratios, which by definition are constrained to fall in the range from -1 to +1, can be used, like a color index, to detect changes in the energy produced by the X-ray emitting plasma. For instance, if the hardness ratio increases for a given epoch, then the star is producing more high-energy than low-energy photons during this period of time. Such a change would suggest that the temperature of the X-ray emitting plasma has increased or that a plasma volume with a higher temperature has become active. If the hardness ratio stays constant, but the overall X-ray luminosity increases, then there is no change the distribution of energies of the X-ray photons produced by the X-ray generation plasma. In this case, the plasma temperature would not have changed but a greater volume of plasma must be active at this temperature in order to generate the increase in overall X-ray brightness. These ratios are plotted in the panels below each light curve in Figures 3.6 and 3.7. Although there are some variations in hardness ratio, the hardness ratios stay fairly constant throughout each observation.

For the stars in our sample, we found five of the nine sources to have significant flares. Interestingly, all of the observed flares occurred in the stars classified as cTTS and wTTS in our sample. TW Hya experienced a significant flare at 28 ks, at which

time the hard X-ray flux quadrupled and the soft X-ray flux doubled. This flare had a very rapid rise time and then began fading almost immediately, returning to near-quiescence after about 10 ks. At the onset of the flare, the hardness ratio indicates that the X-ray flux became harder (e.g., as the hardness ratio become harder, the value approached +1). SU Aur began to flare at the beginning of the observation until about 50 ks, nearly half the duration of the observation. For SU Aur, during the flare both the hard and soft X-ray count rates increased by more than a factor of ten without any noticeable change in hardness ratio. HD 98800 (labeled with its alternate name TV CrT in Figure 3.6) began to flare 78 ks into the observation and continued to flare for about 10 ks. DoAr 21 experienced a 40 ks flare, beginning 50 ks into the observation. The X-ray flux increased by more than a factor of ten, but there is no change in the hardness ratio. V987 Tau flared from the beginning of the observation to about 30 ks, and then again, but for a shorter duration, from 50 ks to 60 ks. The second flare is accompanied by a slight change in hardness ratio toward a harder X-ray flux.

Table III.1. Observations with HETGS from *Chandra*

Star	Type	Exp. Time (ks)	HEG counts	MEG counts	log L_X (erg s^{-1})
TW Hya	cTTS	47.694	1184	382.3	30.19
SU Aur	cTTS	98.509	6846	15103	30.90
HD 98800	wTTS	98.892	1372	4244	29.79
V987 Tau	wTTS	100.457	2788	7806	30.90
DoAr 21	wTTS	90.990	8829	15790	31.66
Hen3-600	wTTS	99.407	913	2507	29.42
HIP 92680	post-TTS	73.899	5508	16172	30.50
V824 Ara C	post-TTS	94.226	17795	56405	30.52
BO Mic[1]	MS star	34.397	832	4262	29.88
		34.599	707	2282	29.85

Note. — The current classification (classical, weak-lined, post T Tauri, or main sequence) are listed. The exposure times denote the actual amount of time each star was observed which is slightly less than the time requested. The fourth and fifth columns list the number of counts (photons detected on the ACIS CCD) detected by the high and medium energy gratings (HEG and MEG) respectively over the duration of each individual observation.[1]Two separate observations of BO Mic were analyzed.

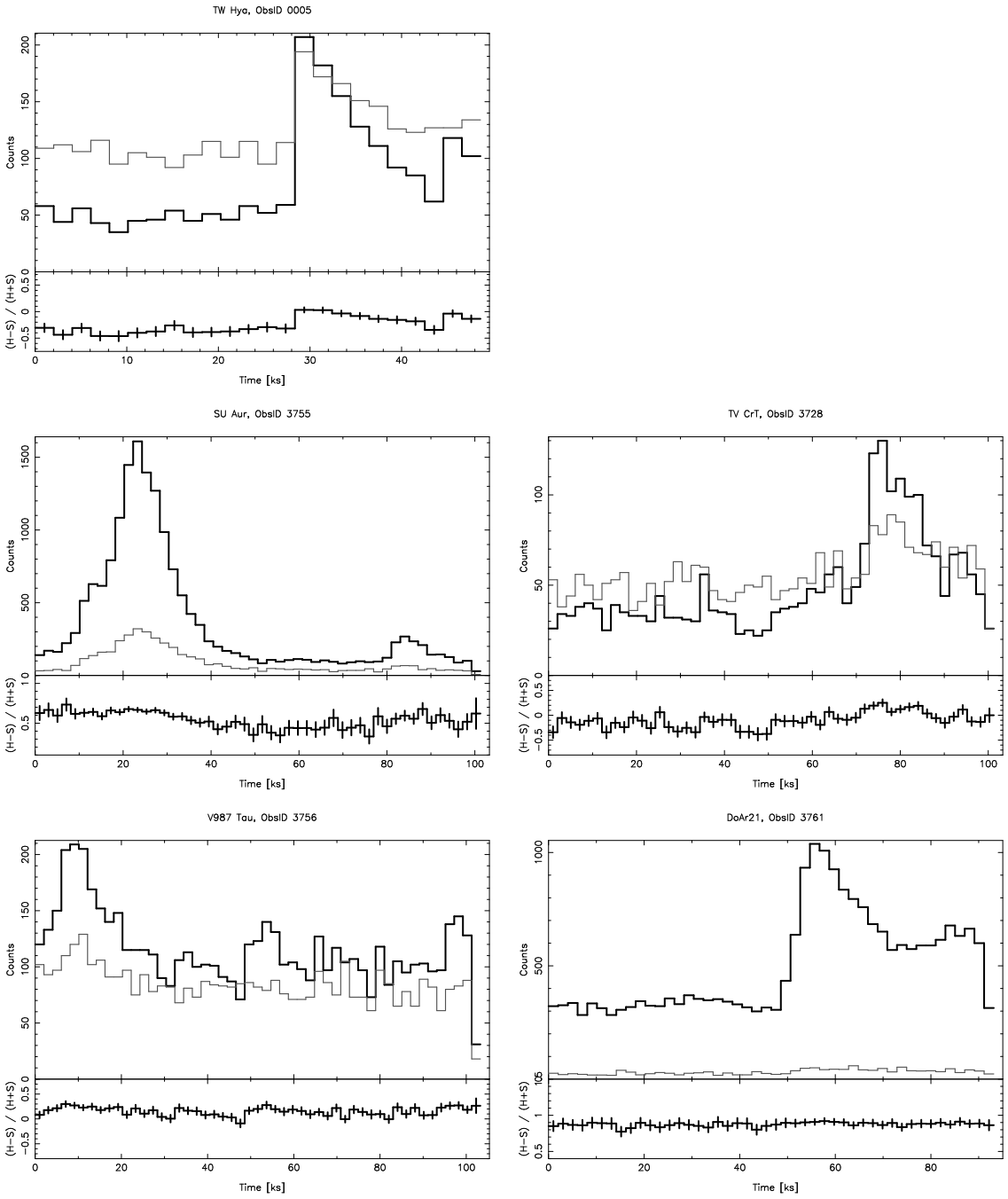

Figure 3.6: Light curves for full integration times for sources determined to flare over the course of the observation in the sample. The light curve for HD 98800 is listed under an alternate name for the star, TV CrT. The dark black line in each panel denotes hard X-rays and the gray line denotes soft X-rays. The temporal evolution of the hardness ratios are plotted in the bottom panel of each figure.

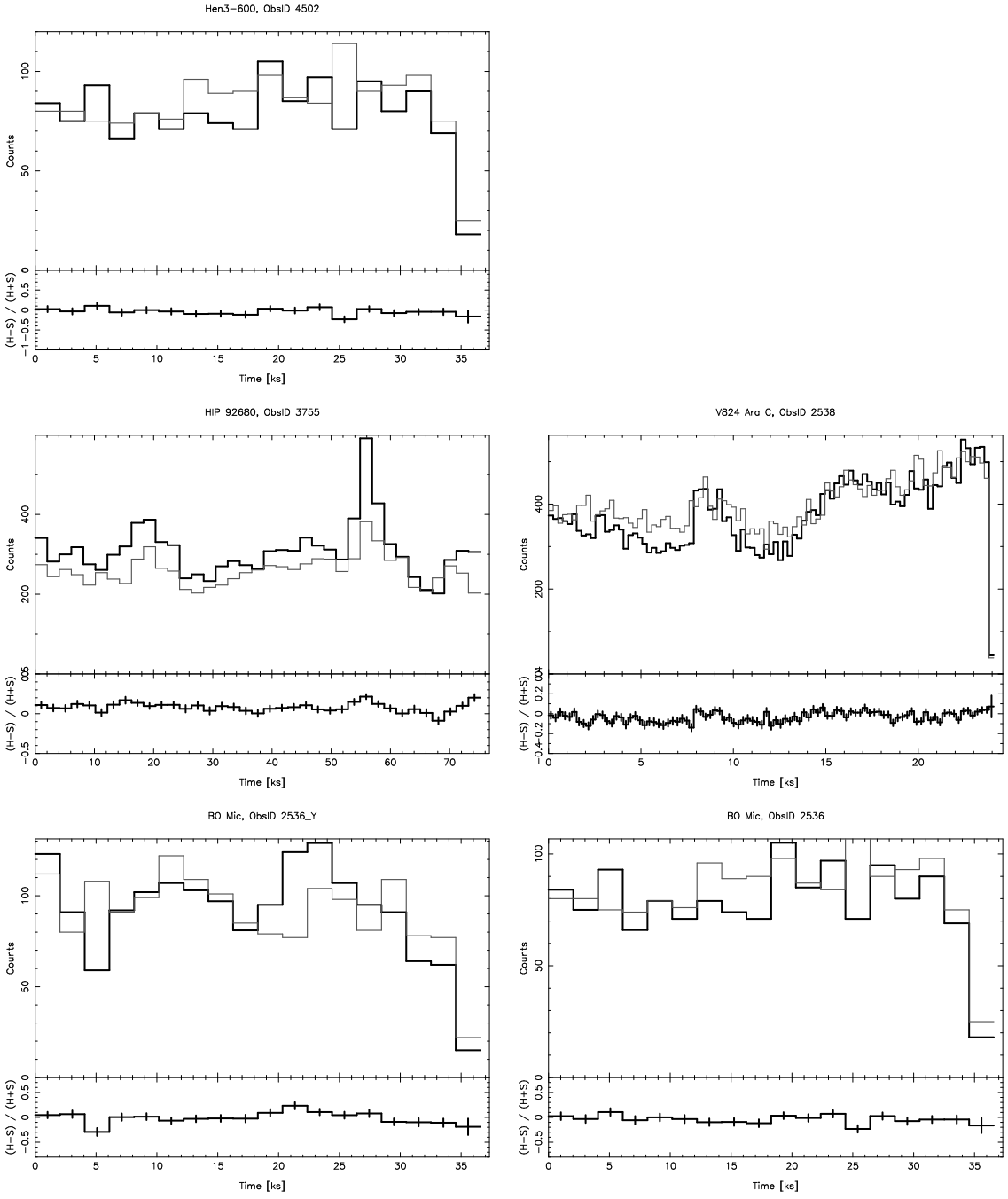

Figure 3.7: Light curves for full integration times for non-flaring sources in the sample. The dark black line in each panel denotes hard X-rays and the gray line denotes soft X-rays. The temporal evolution of the hardness ratios are plotted in the bottom panel of each figure.

3.4 Line flux measurements

For each observation with significant flaring over the observation period, we extracted separate flaring (fl) and quiescent (qu) spectra. We then measured line fluxes for the flaring and quiescent spectra individually, as well as line fluxes for the combined spectra.

Although HETGS spectra are primarily dominated by emission lines, we need to account for some continuum emission in order to measure individual line fluxes. In order to do this, we fit each spectrum with a model continuum with three temperature components. In addition, we accounted for absorption using hydrogen column density (N_H) values from the literature (listed in Table III.2). The absorption was then entered into the *wabs* function in XSPEC used in conjunction with ISIS. The continuum model, determined from continuum emissivities in the Astrophysical Plasma Emission Database (APED)(Smith et al., 2001), was then fit to the line-free regions of the spectra.

Once a continuum was determined and removed, we were able to measure individual line fluxes. See Tables III.3 and III.6 for a list of all the lines, and their respective wavelengths, for which we measured line fluxes. For each line, a Gaussian was fit to a small region of wavelength space that encompassed the theoretical wavelength of the emission line to be measured (Figure 3.8). All of the lines used in our analysis were in the region from 2.5 to 15 Å where the sensitivity ranges of HEG and MEG overlap. Thus we were able to use the combined HEG and MEG data to extract spectra for all of our source observations. Our results for the line fluxes obtained from the He-like

Table III.2. Hydrogen column density (N_H)

Star	N_H [10^{22}cm^{-2}]	Source
TW Hya	0.020	Stelzer & Schmitt (2004)
SU Aur	0.117*	Telleschi et al. (2007b)
HD 98800	0.048*	Akeson et al. (2007)
V987 Tau	0.061*	Telleschi et al. (2007b)
DoAr 21	1.04	Vuong et al. (2003)
Hen3-600	0.010	Huenemoerder et al. (2007)
HIP 92680	0.001	Argiroffi et al. (2004)
V824 Ara C	6.00×10^{-4}	Pasquini et al. (1989)
BO Mic	0.47*	Makarov (2003)

Note. — N_H used in determining the continuum as well as the source in the literature are listed. For some sources (denoted with *), the literature quoted a visual extinction (A_V) which we then converted to N_H using $N_H = 1.6 \times 10^{21}$ A_V(Vuong et al., 2003).

triplets of Si XIII, Mg XI, and Ne IX are presented in Table III.3.

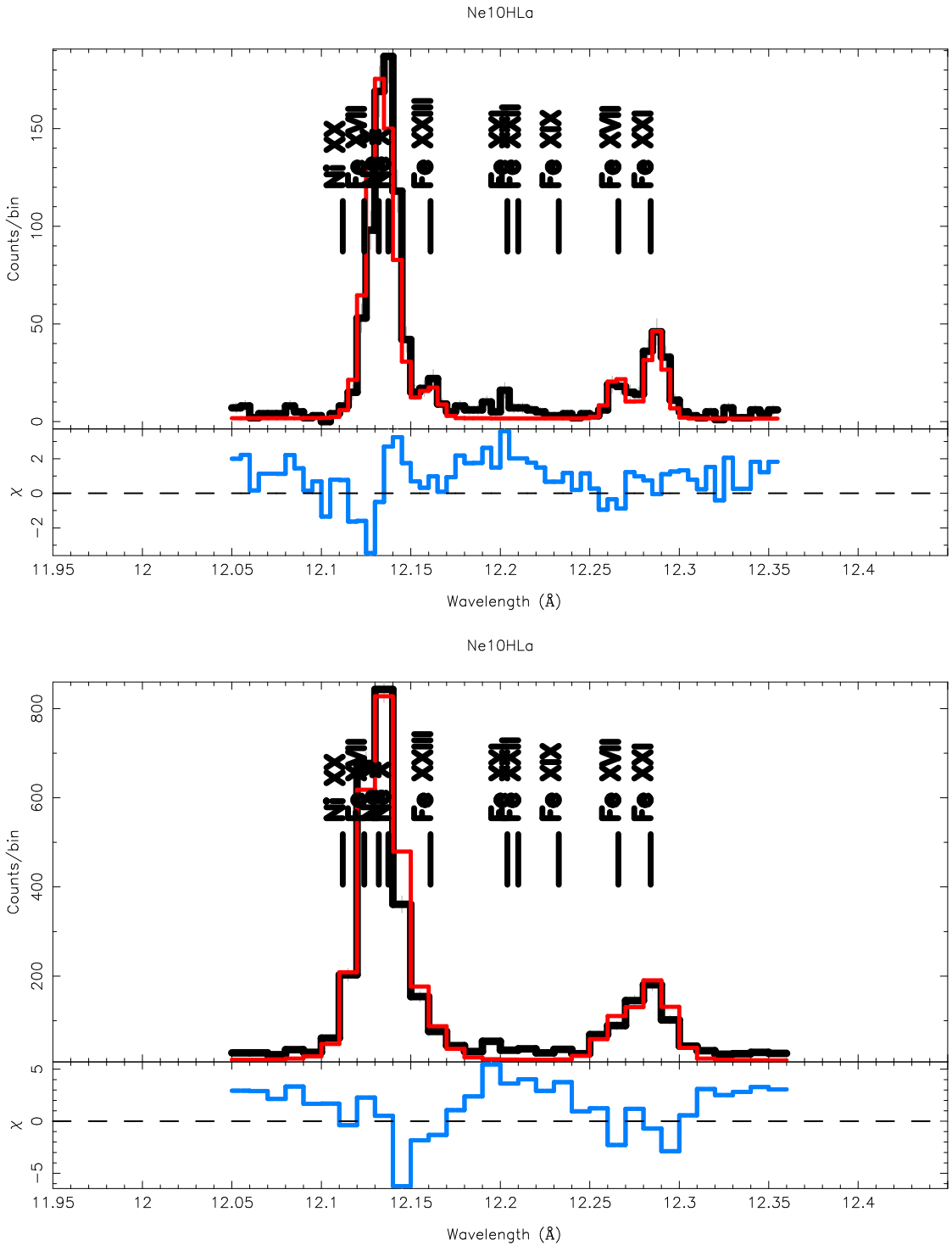

Figure 3.8: The top panel shows the HEG spectrum and the bottom panel the MEG spectrum in the region around 12 Å where the Ne X HLyα line emits. The black line is the data and overplotted in red are the Gaussian fits to the lines. We also simultaneously fit iron lines in the region to obtain a better fit.

Table III.3. Line flux measurements for He-like triplet (*r*,*i*,*f*) lines of the Si XIII, Mg XI, and Ne IX lines

Observation	Si XIII (10^6 photon cm^{-1} s^{-1})	Mg XI (10^6 photon cm^{-1} s^{-1})	Ne IX (10^6 photon cm^{-1} s^{-1})
λ (Å)	6.65/6.69/6.74	9.17/9.23/9.31	13.45/13.55/13.7
TW Hya (*r*)	1.76 ± 0.67	2.37 ± 2.43	153.3 ± 18.08
(*i*)	3.02 ± 0.78	0.40 ± 0.56	108.8 ± 9.91
(*f*)	2.45 ± 0.72	1.46 ± 0.76	58.64 ± 7.60
TW Hya - fl (*r*)	4.41 ± 1.93	2.83 ± 3.06	115.7 ± 37.81
(*i*)	2.58 ± 1.69	1.01 ± 1.45	119.60 ± 19.70
(*f*)	5.32 ± 1.70	0.62 ± 1.16	73.35 ± 16.11
TW Hya - qu (*r*)	0.66 ± 0.64	0.73 ± 0.86	184.6 ± 22.5
(*i*)	< 0.45	< 0.51	116.2 ± 12.0
(*f*)	0.58 ± 0.68	0.49 ± 0.71	56.88 ± 9.06
SU Aur (*r*)	7.73 ± 1.03	6.36 ± 6.39	6.68 ± 4.45
(*i*)	0.76 ± 0.74	0.07 ± 0.44	2.91 ± 2.10
(*f*)	5.47 ± 0.86	2.74 ± 1.04	4.22 ± 2.81
SU Aur - fl (*r*)	18.61 ± 1.56	15.17 ± 15.22	3.96 ±3.74

Table III.3 (cont'd)

Observation	Si XIII (10^6 photon cm^{-1} s^{-1})	Mg XI (10^6 photon cm^{-1} s^{-1})	Ne IX (10^6 photon cm^{-1} s^{-1})
(*i*)	6.71 ± 1.06	3.12 ± 1.04	9.60 ± 3.47
(*f*)	14.79 ± 1.22	9.61 ± 1.50	14.93 ± 4.58
SU Aur - qu (*r*)	5.42 ± 1.38	4.76 ± 4.89	3.16 ± 3.91
(*i*)	1.21 ± 0.83	0.47±0.76	< 6.39
(*f*)	1.23 ± 0.90	1.83 ± 1.22	3.81 ± 3.91
HD 98800 (*r*)	3.23 ± 0.57	2.13 ± 2.15	38.05 ± 5.60
(*i*)	0.16 ± 0.25	0.38±0.42	8.58 ± 2.50
(*f*)	0.99 ± 0.38	1.81 ± 0.55	24.34 ± 3.91
HD 98800 - fl (*r*)	2.94 ± 1.37	1.31 ± 1.17	40.98 ± 12.86
(*i*)	0.33 ± 0.64	0.58 ± 0.86	2.58 ± 3.35
(*f*)	1.94 ± 0.98	2.48 ± 1.34	29.64 ± 9.16
HD 98800 - qu (*r*)	5.24 ± 0.87	2.36 ± 2.40	36.38 ± 5.81
(*i*)	0.96 ± 0.52	0.45 ± 0.49	9.65 ± 2.90
(*f*)	1.46 ± 0.51	1.33 ± 0.56	19.51 ± 4.24
V987 Tau (*r*)	6.13 ± 0.75	6.88 ± 6.91	14.67 ± 3.79

Table III.3 (cont'd)

Observation	Si XIII (10^6 photon cm^{-1} s^{-1})	Mg XI (10^6 photon cm^{-1} s^{-1})	Ne IX (10^6 photon cm^{-1} s^{-1})
(*i*)	0.47 ± 0.40	2.71 ± 0.74	9.97 ± 2.89
(*f*)	4.81 ± 0.70	4.22 ± 0.85	12.85 ± 3.10
V987 Tau - fl (*r*)	8.75 ± 1.26	7.52 ± 7.61	17.81 ± 6.35
(*i*)	< 0.84	3.56 ± 1.16	7.29 ± 7.0
(*f*)	5.17 ± 1.03	3.69 ± 1.21	13.31 ± 4.67
V987 Tau - qu (*r*)	4.11 ± 0.89	5.75 ± 5.82	8.84 ± 4.61
(*i*)	0.62 ± 0.54	2.22 ± 1.24	14.40 ± 4.48
(*f*)	5.84 ± 1.00	4.74 ± 1.65	13.34 ± 4.55
DoAr 21 - fl (*r*)	...	<3.09	33.87 ± 31.04
(*i*)	...	<1.95	14.68 ± 23.66
(*f*)	...	<2.4	<65.25
DoAr 21 - qu (*r*)	16.99 ± 2.98	10.70 ± 10.91	12.68 ± 29.70
(*i*)	9.26 ± 2.59	2.50 ± 3.14	<17.58
(*f*)	16.76 ± 2.77	17.97 ± 4.75	16.83 ± 26.49
Hen 3-600 (*r*)	1.60 ± 0.38	1.84 ± 1.85	20.25 ± 3.94

Table III.3 (cont'd)

Observation	Si XIII (10^6 photon cm^{-1} s^{-1})	Mg XI (10^6 photon cm^{-1} s^{-1})	Ne IX (10^6 photon cm^{-1} s^{-1})
(*i*)	1.29 ± 0.35	0.55 ± 0.34	3.81 ± 1.47
(*f*)	0.74 ± 0.28	0.51 ± 0.30	10.09 ± 2.49
HIP 92680 (*r*)	12.51 ± 1.28	14.60 ± 14.66	48.96 ± 7.87
(*i*)	2.93 ± 0.85	4.50 ± 1.22	18.73 ± 5.20
(*f*)	10.07 ± 1.15	11.41 ± 1.58	48.53 ± 6.32
V824 Ara C (*r*)	50.99 ± 2.11	56.86 ± 57.09	218.4 ± 18.13
(*i*)	10.56 ± 1.23	11.89 ± 1.79	70.61 ± 8.06
(*f*)	29.81 ± 1.65	35.94 ± 2.45	176.20 ± 12.82
BO Mic 1 (*r*)	7.97 ± 1.59	4.61 ± 4.80	135.4 ± 31.69
(*i*)	1.87 ± 1.01	0.73 ± 1.10	31.21 ± 14.38
(*f*)	4.28 ± 1.28	5.98 ± 2.24	159.40 ± 31.19
BO Mic 2 (*r*)	4.60 ± 1.26	5.58 ± 5.74	178.4 ± 34.88
(*i*)	0.51 ± 0.64	4.97 ± 1.98	32.67 ± 14.29
(*f*)	3.62 ± 1.14	4.04 ± 1.95	92.38 ± 23.69

Note. — The theoretical wavelengths for each triplet are listed in the first row of the table. Errors represent 68% confidence limits. Upper limits are with 99% confidence.

In this group of measurements, the intercombination line is generally the weakest line, and therefore the most difficult from which to measure line fluxes. From the line measurements in Table III.3, we are able to derive R (R = f/i) and G (G = $(f+i)/r$)) ratios that can indicate the density and temperature regime of the plasmas where these lines are formed. Table III.4 lists the R and G ratios as well as the electron densities and temperatures inferred from these ratios. The errors for Table III.4 are calculated using the standard propagation of errors techniques. For the R ratio, the error is as follows:

$$(dR/R)^2 = (df/f)^2 + (di/i)^2 \tag{3.2}$$

Similarly, the error on the G ratio was calculated using the following formulae. First, the error of the numerator (N), f+i, was calculated, and then used to calculate the error on the ratio, (f+i)/r .

$$(dN)^2 = (df)^2 + (di)^2 \tag{3.3}$$

$$(dG/G)^2 = (dN/fN)^2 + (dr/r)^2 \tag{3.4}$$

Once we calculated the R and G ratios for each observation, we used the theoretically predicted line fluxes in the APEC database (Smith et al., 2001) to infer temperatures and densities from these ratios (see §4.2.1 for more detail). For ratios with large errors, we were only able to estimate upper limits for either the densities or temperatures. Some R and G ratios indicated temperatures and densities more than three sigma below the theoretically predicted values so we do not estimate a temperature or density for those ratios, indicated by the long dash in Table III.4.

Table III.4. Inferred temperature and density properties

Star	He-like triplet	R ratio (f/i)	G ratio (f+i)/r	log n_e	log T
TW Hya (all)	Si XIII	0.81 ± 0.13	3.10 ± 0.26	<14.0	—
	Mg XI	3.68 ± 1.31	0.78 ± 0.74	<14.5	6.5-7.75
	Ne IX	0.54 ± 0.09	1.09 ± 0.05	12.4 ± 0.13	<6.25
TW Hya (fl)	Si XIII	2.06 ± 0.57	1.79 ± 0.09	13.75 ± .5	—
	Mg XI	0.61 ± 1.19	0.58 ± 1.18	13.5 ± 0.75	6.5-7.75
	Ne IX	0.61 ± 0.15	1.67 ± 0.27	12.5 ± 0.25	< 6.35
TW Hya (qu)	Si XIII	—	—	—	—
	Mg XI	—	—	—	—
	Ne IX	0.49 ± 0.12	0.94 ± 0.01	12.45 ± 0.15	<6.25
SU Aur (all)	Si XIII	7.19 ± 0.97	0.81 ± 0.22	—	6.5-7.75
	Mg XI	3.08 ± 0.30	0.84 ± 0.98	<12.75	6.25-7.5
	Ne IX	1.45 ± 0.28	1.07 ± 0.17	11.75 ± 0.15	<6.85
HD 98800 (all)	Si XIII	6.17 ± 1.53	0.36 ± 0.52	<14.1	—
	Mg XI	4.72 ± 1.05	1.03 ± 0.91	<12.75	6.25-7.5
	Ne IX	2.84 ± 0.24	0.87 ± 0.13	<12.75	6.3 ± 0.2

Table III.4 (cont'd)

Star	He-like triplet	R ratio (f/i)	G ratio (f+i)/r	log n_e	log T
HD 98800 (fl)	Si XIII	5.97 ± 1.90	0.77 ± 0.54	<14.5	6.5-7.75
	Mg XI	4.25 ± 1.38	2.33 ± 0.53	<14.25	<6.7
	Ne IX	—	0.79 ± 0.23	—	<6.7
HD 98800 (qu)	Si XIII	1.53 ± 0.42	0.77 ± 0.54	13.6 ± 0.4	6.5-7.75
	Mg XI	2.98 ± 1.01	0.75 ± 0.83	<14.5	6.25-7.5
	Ne IX	2.02 ± 0.21	0.80 ± 0.19	11.5 ± 0.13	6.3 ± 0.3
Hen3-600 (all)	Si XIII	0.57 ± 0.27	1.27 ± 0.20	14.00 ± 0.15	—
	Mg XI	0.94 ± 0.18	0.58 ± 0.81	13.25 ± 0.5	6.5-7.75
	Ne IX	2.65 ± 0.30	0.69 ± 0.21	11.15 ± 0.15	6.55 ± 0.35
V987 Tau (all)	Si XIII	10.16 ± 0.83	0.86 ± 0.17	—	6.5-7.75
	Mg XI	1.56 ± 0.18	1.01 ± 0.98	12.68 ± 0.13	6.25-7.5
	Ne IX	1.29 ± 0.16	1.56 ± 0.05	11.88 ± 0.13	—
V987 Tau (fl)	Si XIII	—	0.59 ± 0.21	—	7.0 ± 0.25
	Mg XI	1.03 ± 0.05	0.96 ± 0.96	13.00 ± 0.1	6.25-7.5
	Ne IX	1.83 ± 0.89	1.16 ± 0.44	11.6 ± 0.6	6.25-7.25

Table III.4 (cont'd)

Star	He-like triplet	R ratio (f/i)	G ratio $(f+i)/r$	log n_e	log T
V987 Tau (qu)	Si XIII	9.45 ± 0.86	1.57 ± 0.10	—	—
	Mg XI	2.14 ± 0.44	1.21 ± 0.92	12.0 ± 0.5	6.25-7.5
	Ne IX	0.93 ± 0.14	3.14 ± 0.41	12.2 ± 0.2	—
HIP 92680 (all)	Si XIII	3.44 ± 0.27	1.04 ± 0.11	<13.1	<6.75
	Mg XI	2.54 ± 0.23	1.09 ± 0.99	12.38 ± 0.12	6.25-7.5
	Ne IX	2.59 ± 0.24	1.37 ± 0.06	10.8 ± 0.5	—
V824 Ara C (all)	Si XIII	2.82 ± 0.10	0.79 ± 0.06	<13.1	6.65 ± 0.10
	Mg XI	3.02 ± 0.13	0.84 ± 1.0	<11.5	6.25-7.5
	Ne IX	2.5 ± 0.1	1.13 ± 0.02	11.75 ± 0.05	—
BO Mic (1)	Si XIII	2.28 ± 0.45	0.77 ± 0.31	<14.5	6.5-7.75
	Mg XI	8.14 ± 1.45	1.46 ± 0.92	—	6.25-7.5
	Ne IX	5.11 ± 0.42	1.41 ± 0.05	—	—
BO Mic (2)	Si XIII	7.05 ± 1.20	0.90 ± 0.33	—	6.5-7.75
	Mg XI	0.81 ± 0.27	1.61 ± 0.93	13.1 ± 0.3	6.26-7.5
	Ne IX	2.83 ± 0.35	0.70 ± 0.23	10.8 ± 0.45	6.55 ± 0.45

Note. — The R (density-sensitive) and G (temperature-sensitive) ratios for Si XIII, Mg XI, and Ne IX are listed for each observation. For stars observed to flare, the ratios determined from the full spectrum (all), flaring (fl), and quiescent (qu) states are listed in separate rows.

3.4.1 *Temperature estimates from line ratios*

Estimating the coronal temperature of an X-ray emitting plasma can be determined by several methods. Previous studies, such as Kastner et al. (2004) and Huenemoerder et al. (2007) employed emission measure distribution analysis to derive both the thermal structure and elemental abundances for their respective objects of study, TW Hya and Hen 3-600. The differential emission measure (DEM) summarizes the temperature structure of the coronae of stars. However, determining the DEM through modeling requires many assumptions. For one, the measured line fluxes are assumed to be Gaussian and thus have symmetric statistical uncertainties as measured from the fitted fluxes (Huenemoerder et al., 2006). This was not the case for many of our lines, particularly for measurements made in the flaring and quiescent spectra for which the average count rates were lower. In addition, the standard emission measure distribution does not include any density dependence and thus ignores the contribution from the strong density-sensitive line of the He-like triplets. For each star in our sample, a subset of the lines would need to be selected from which to determine the DEM. Since line strengths of various transitions are different for the stars in our sample, the determination of the DEM is unique to each observation. Since the focus of this study is to compare these stars using globally-consistent analysis techniques, we do not use DEM modeling as a technique for estimating temperatures.

Another method that is useful in determining the temperature of an X-ray plasma is to use the ratios of strong line fluxes. In particular, the ratios of line fluxes from adjacent ionization states of a particular element (e.g., the H-like Lyman α (HLα

line and the He-like resonance (Her) lines represent adjacent ionization states) are indicative of plasma temperature, irrespective of elemental abundances (Ness et al., 2004). In Chandra HETGS spectra, the H-like and He-like lines of silicon, magnesium, neon, and oxygen are particularly strong and can be used to estimate temperature. This method is particularly useful for comparisons between multiple sources as we are doing in this study and has been previously employed by Ness et al. (2004) and Testa et al. (2007). The temperatures determined from these ratios are only valid for isothermal plasmas, which is not expected from the X-ray emitting plasmas of the stars in our sample, but are still advantageous in making comparisons among sources. The ratios of the H-like Lyman α line to the He-like resonance line for Si XIII, Mg XI, and Ne IX, and the temperatures derived from these ratios are listed in Table III.5. The inferred temperatures are from the predicted formation temperatures of the ratio for each ion taken from the APEC database (Smith et al., 2001).

For the Si ratios, the temperatures inferred from this method are consistent with the temperatures derived from the G ratio for each observation except for the two post-T Tauri stars in the sample. For HIP 92680, the G ratio provides an upper limit of log T $<$6.75, but the Lyα/Her ratio implies a temperature of log T = 7.15 $\pm$ 0.01, and similarly for V824 Ara C, the G ratio sets an upper limit of log T $<$6.75, but the Lyα/Her ratio indicates a temperature of log T = 7.08 $\pm$ 0.004. In both cases, the temperature derived from the Lyα/Her ratio is much higher than the upper limit imposed by the G ratio. The temperatures inferred from the Mg Lyα/Her ratio are consistent with those derived from the G ratios, mainly because the temperatures were not well-constrained because of large error on the line flux measurements of

the G ratios. The Ne Lyα/Her ratio temperatures are also consistent with the G ratio temperatures for all observations except those of TW Hya and HD 98800. For these stars, the Ne Lyα/Her ratios consistently yield a higher temperature than the G ratios for the full observations as well as the flaring and quiescent states. For TW Hya, the Lyα/Her derived temperatures are systematically higher than the upper limits set by the G ratio by a factor of log T $\sim$0.3. In the case of HD 98800, the full spectrum and quiescent states have the same temperatures inferred from the G ratio (6.3 $\pm$ 0.2 and 6.3 $\pm$ 0.3 respectively) and the Lyα/Her ratio (6.74 $\pm$ 0.02 and 6.75 $\pm$ 0.02 respectively) but the two methods differ by log T $\sim$0.45. Since the difference in temperatures are systematic, the differences in temperatures are most likely due to differences in the theoretical calculations that predict the temperatures by the two different methods.

Table III.5. Temperature-sensitive ratio of H-like Lyα to He-like resonance and inferred temperatures

Star	state	Si ratio	log T(K) - Si	Mg ratio	log T(K) - Mg	Ne ratio	log T(K) - Ne
TW Hya		1.30 ± 0.21	$7.16^{+0.03}_{-0.04}$	0.47 ± 0.52	$6.96^{+0.07}_{-0.10}$	0.50 ± 0.09	6.58 ± 0.01
TW Hya	fl	1.65 ± 0.33	$7.20^{+0.05}_{-0.07}$	2.32 ± 0.56	$7.24^{+0.10}_{-0.15}$	1.19 ± 0.31	$6.69^{+0.04}_{-0.05}$
TW Hya	qu	2.48 ± 0.84	$7.27^{+0.12}_{-0.28}$	1.39 ± 0.72	$7.14^{+0.11}_{-0.21}$	0.50 ± 0.09	6.58 ± 0.01
SU Aur		2.86 ± 0.12	7.30 ± 0.2	2.76 ± 0.16	$7.28^{+0.03}_{-0.04}$	7.52 ± 0.66	$7.01^{+0.11}_{-0.20}$
SU Aur	fl	2.06 ± 0.06	7.24 ± 0.1	2.04 ± 0.09	7.21 ± 0.02	19.2 ± 0.94	$7.22^{0.17}_{0.53}$
SU Aur	qu	1.40 ± 0.16	7.17 ± 0.03	1.76 ± 0.27	$7.18^{+0.05}_{-0.06}$	12.3 ± 1.22	$7.11^{0.19}_{0.29}$
HD 98800		0.38 ± 0.30	$6.99^{+0.03}_{-0.04}$	0.73 ± 0.19	7.02 ± 0.03	1.73 ± 0.13	6.74 ± 0.02
HD 98800	fl	1.26 ± 0.27	$7.15^{+0.04}_{-0.05}$	2.88 ± 0.80	$7.28^{+0.13}_{-0.29}$	1.82 ± 0.29	$6.75^{+0.04}_{-0.05}$
HD 98800	qu	0.23 ± 0.37	$6.93^{+0.03}_{-0.04}$	0.21 ± 0.78	$6.84^{+0.08}_{-0.15}$	1.75 ± 0.14	6.75 ± 0.02

Table III.5 (cont'd)

Star	state	Si ratio	log T(K) - Si	Mg ratio	log T(K) - Mg	Ne ratio	log T(K) - Ne
V987 Tau		1.15 ± 0.04	7.14 ± 0.01	1.52 ± 0.11	7.15 ± 0.02	4.45 ± 0.25	$6.91^{+0.04}_{-0.05}$
V987 Tau	fl	1.00 ± 0.03	$7.12^{+0.004}_{-0.003}$	1.67 ± 0.16	7.17 ± 0.03	3.89 ± 0.34	$6.88^{+0.05}_{-0.07}$
V987 Tau	qu	1.21 ± 0.10	7.15 ± 0.02	1.49 ± 0.17	7.15 ± 0.03	7.14 ± 0.51	$7.00^{+0.09}_{-0.14}$
DoAr21		3.59 ± 0.59	7.34 ± 0.03	—	—	—	
DoAr21	fl	2.67 ± 0.41	7.29 ± 0.03	3.69 ± 1.32	$7.34^{+0.07}_{-0.10}$	4.26 ± 3.8	$6.90^{+0.12}_{-0.32}$
DoAr21	qu	3.99 ± 1.66	$7.37^{+0.07}_{-0.11}$	—	—	—	
Hen3-600		1.30 ± 0.13	7.16 ± 0.02	0.70 ± 0.15	$7.02^{+0.02}_{-0.03}$	1.69 ± 0.18	$6.74^{+0.02}_{-0.03}$
HIP 92680		1.21 ± 0.04	7.15 ± 0.01	1.65 ± 0.09	7.17 ± 0.02	3.97 ± 0.16	6.88 ± 0.03
V824 Ara C		0.78 ± 0.03	7.08 ± 0.004	1.33 ± 0.04	7.13 ± 0.01	2.85 ± 0.08	6.83 ± 0.01

For each ion, the X-ray luminosity and Lyα to He-like resonance are linearly correlated (Figure 3.9). We also find that for increasing Z (from Ne to Mg to Si), the slope of the relationship between Lyα/Her and log L_X decreases. Ness et al. (2004) found the same result for ions of Si, Mg, Ne, and O for a large sample of active stars.

3.5 Abundances

In addition to R and G ratios, relative abundances are another useful diagnostic that can be derived from the line flux measurements of these observations. In other studies utilizing high-resolution X-ray data from Chandra, abundances are derived from differential emission measure (DEM) distributions (i.e., Huenemoerder et al. (2007)). However, these studies generally include great uncertainties in the actual shape of the DEM and thus great uncertainties in determining abundance measurements.

Another technique, first proposed by Pottasch (1967), employs the measurement of the H-like and He-like lines of silicon, magnesium, oxygen, and neon as well as Ne-like Fe XVII. Ratios of these particular line fluxes do not strongly depend on temperature. Recent studies by Drake & Testa (2005) and Schmitt & Ness (2002) have utilized this technique. For a given element, the peak formation temperature of the H-like ion always exceeds that of the corresponding He-like ion. However, as atomic mass increases, the peak formation temperatures of both H-like and He-like ions also increases (Liefke et al., 2008). Because of this behavior, pairs of H-like and He-like ions of successive elements, such as neon and magnesium and magnesium and silicon, have similar peak formation temperatures (Figure 3.10).

Table III.5 (cont'd)

Star	state	Si ratio	log T(K) - Si	Mg ratio	log T(K) - Mg	Ne ratio	log T(K) - Ne
BO Mic - 1		0.39 ± 0.31	$6.99^{+0.03}_{-0.05}$	1.77 ± 0.37	$7.18^{+0.06}_{-0.09}$	2.21 ± 0.22	$6.78^{+0.03}_{-0.04}$
BO Mic - 2		0.71 ± 0.21	7.07 ± 0.03	1.59 ± 0.28	$7.16^{+0.05}_{-0.06}$	1.54 ± 0.18	$6.73^{+0.02}_{-0.03}$

Note. — The line fluxes used to calculate these ratios can be found in Table III.6. The inferred temperatures are based on theoretical data from the APEC database.

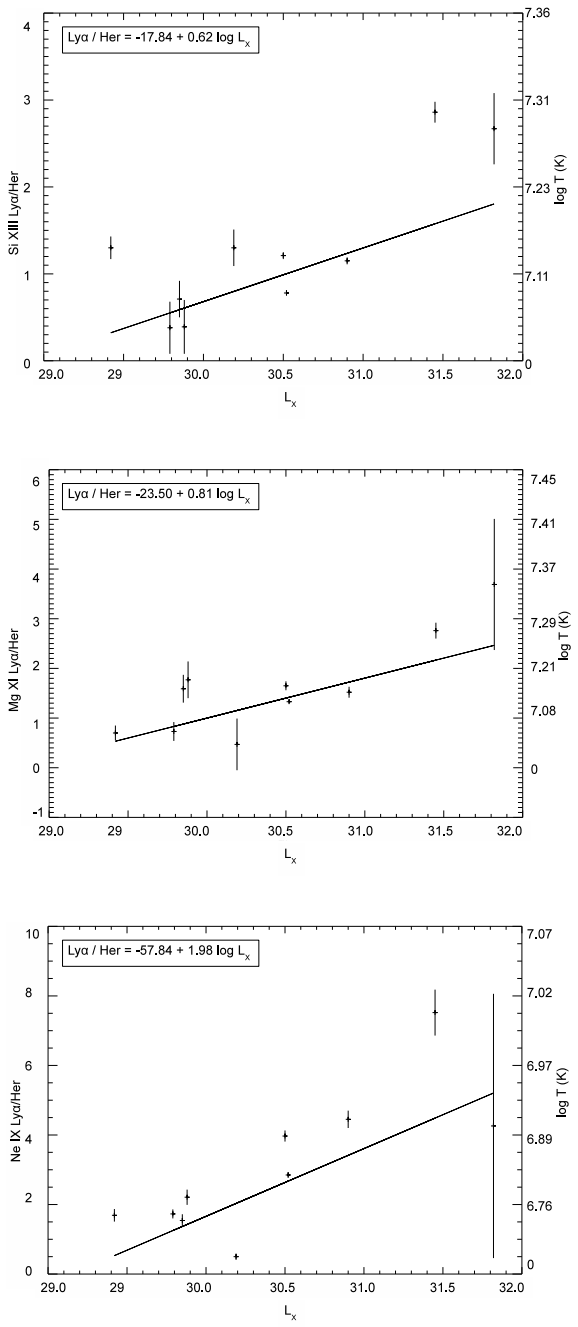

Figure 3.9: Log L_X is plotted against the Lyman α to He-like resonance line ratios for Si XIII, Mg XI, and Ne IX. Average temperatures inferred from the APEC database are listed along the y-axis on the right side of each plot. The equation for the best fit line is in the top left corner of each plot, and the best fit line is shown in each figure.

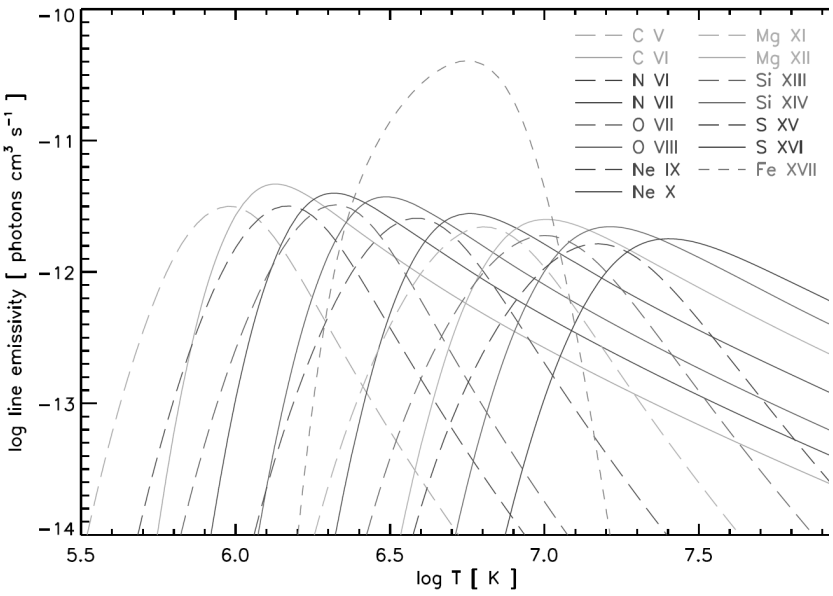

Figure 3.10: Line emissivity curves for different H-like and He-like ions as well as Fe XVII at 15.01 Å (Liefke et al., 2008).

Table III.6. Line flux measurements used for determining abundance ratios

Star	Line	Wavelength Å	Flux 10^6 (photon cm^{-1} s^{-1})
TW Hya	S HLyα	4.73	0.01 ± 0.35
	S He-r	5.04	0.53 ± 0.71
	Si HLyα	6.18	2.30 ± 0.73
	Si He-r	6.65	1.76 ± 0.67
	Mg HLyα	8.42	1.12 ± 0.71
	Mg He-r	9.17	2.37 ± 0.87
	Ne HLyα	12.10	76.0 ± 5.88
	Ne He-r	13.45	3.35 ± 2.69
	Fe XVII	15.01	53.8 ± 9.30
	Fe XVII	16.78	24.2 ± 6.60
	Fe XVII	17.05	62.0 ± 10.6
	Fe XVII	17.09	32.3 ± 8.12
SU Aur	S HLyα	4.73	7.06 ± 1.85
	S He-r	5.04	5.72 ± 1.50
	Si HLyα	6.18	22.2 ± 1.51

Table III.6 (cont'd)

Star	Line	Wavelength Å	Flux 10^6 (photon cm^{-1} s^{-1})
	Si He-r	6.65	7.73 ± 1.03
	Mg HLyα	8.42	17.5 ± 1.31
	Mg He-r	9.17	6.36 ± 1.14
	Ne HLyα	12.14	50.2 ± 5.20
	Ne He-r	13.45	6.68 ± 4.45
	Fe XVII	15.01	23.3 ± 5.14
	Fe XVII	16.78	16.3 ± 5.96
	Fe XVII	17.05	20.6 ± 7.32
	Fe XVII	17.09	2.62 ± 3.92
Hen3-600	S HLyα	4.73	0.50 ± 0.41
	S He-r	5.04	1.75 ± 0.65
	Si HLyα	6.18	2.08 ± 0.41
	Si He-r	6.65	1.60 ± 0.38
	Mg HLyα	8.42	1.29 ± 0.39
	Mg He-r	9.17	1.84 ± 0.48

Table III.6 (cont'd)

Star	Line	Wavelength Å	Flux 10^6 (photon cm^{-1} s^{-1})
	Ne HLyα	12.14	34.2 ± 2.78
	Ne He-r	13.45	20.3 ± 3.94
	Fe XVII	15.01	19.4 ± 4.04
	Fe XVII	16.78	10.1 ± 3.18
	Fe XVII	17.05	14.4 ± 3.93
	Fe XVII	17.09	13.0 ± 3.80
HIP 92680	S HLyα	4.73	6.25 ± 1.76
	S He-r	5.04	±
	Si HLyα	6.18	15.2 ± 1.42
	Si He-r	6.65	±
	Mg HLyα	8.42	24.1 ± 1.61
	Mg He-r	9.17	±
	Ne HLyα	12.14	195 ± 8.19
	Ne He-r	13.45	±
	Fe XVII	15.01	110 ± 9.87

Table III.6 (cont'd)

Star	Line	Wavelength Å	Flux 10^6 (photon cm^{-1} s^{-1})
	Fe XVII	16.78	78.9 ± 10.6
	Fe XVII	17.05	103 ± 12.3
	Fe XVII	17.09	98.8 ± 12.5
HD 98800	S HLyα	4.73	0.001 ± 0.20
	S He-r	5.04	0.14 ± 0.41
	Si HLyα	6.18	1.24 ± 0.43
	Si He-r	6.65	3.23 ± 0.57
	Mg HLyα	8.42	1.55 ± 0.52
	Mg He-r	9.17	2.13 ± 0.59
	Ne HLyα	12.14	65.8 ± 4.29
	Ne He-r	13.45	38.1 ± 5.60
	Fe XVII	15.01	37.8 ± 6.45
	Fe XVII	16.78	20.7 ± 5.16
	Fe XVII	17.05	41.2 ± 7.44
	Fe XVII	17.09	45.6 ± 7.89

Table III.6 (cont'd)

Star	Line	Wavelength Å	Flux 10^6 (photon cm^{-1} s^{-1})
V987 Tau	S HLyα	4.73	2.06 ± 0.93
	S He-r	5.04	±
	Si HLyα	6.18	7.07 ± 0.82
	Si He-r	6.65	±
	Mg HLyα	8.42	10.5 ± 0.91
	Mg He-r	9.17	±
	Ne HLyα	12.14	65.3 ± 4.87
	Ne He-r	13.45	±
	Fe XVII	15.01	42.36 ± 6.37
	Fe XVII	16.78	27.6 ± 6.11
	Fe XVII	17.05	43.5 ± 8.03
	Fe XVII	17.09	31.4 ± 6.85
V824 Ara C	S HLyα	4.73	14.8 ± 2.25
	S He-r	5.04	25.5 ± 2.73
	Si HLyα	6.18	39.8 ± 19.8

Table III.6 (cont'd)

Star	Line	Wavelength Å	Flux 10^6 (photon cm^{-1} s^{-1})
	Si He-r	6.65	51.0 ± 2.11
	Mg HLyα	8.42	75.4 ± 2.44
	Mg He-r	9.17	56.9 ± 2.88
	Ne HLyα	12.14	622 ± 12.2
	Ne He-r	13.45	218 ± 18.1
	Fe XVII	15.01	425 ± 16.1
	Fe XVII	16.78	268 ± 16.6
	Fe XVII	17.05	371 ± 20.2
	Fe XVII	17.09	364 ± 19.8
BO Mic 1	S HLyα	4.73	1.45 ± 1.44
	S He-r	5.04	4.33 ± 1.99
	Si HLyα	6.18	3.08 ± 1.14
	Si He-r	6.65	7.97 ± 1.59
	Mg HLyα	8.42	8.18 ± 1.71
	Mg He-r	9.17	4.61 ± 1.96

Table III.6 (cont'd)

Star	Line	Wavelength Å	Flux 10^6 (photon cm^{-1} s^{-1})
	Ne HLyα	12.14	300 ± 24.7
	Ne He-r	13.45	135 ± 31.7
	Fe XVII	15.01	198 ± 40.3
	Fe XVII	16.78	229 ± 71.1
	Fe XVII	17.05	406 ± 151
	Fe XVII	17.09	359 ± 143
BO Mic 2	S HLyα	4.73	0.09 ± 0.57
	S He-r	5.04	1.58 ± 1.41
	Si HLyα	6.18	3.25 ± 1.13
	Si He-r	6.65	4.60 ± 1.26
	Mg HLyα	8.42	8.87 ± 1.82
	Mg He-r	9.17	5.58 ± 1.93
	Ne HLyα	12.14	274 ± 22.3
	Ne He-r	13.45	135 ± 31.7
	Fe XVII	15.01	207 ± 40.6

Table III.6 (cont'd)

Star	Line	Wavelength Å	Flux 10^6 (photon cm^{-1} s^{-1})
	Fe XVII	16.78	187 ± 64.9
	Fe XVII	17.05	253 ± 87.3
	Fe XVII	17.09	458 ± 113

Note. — Hydrogen-like Lyman *alpha* and resonance lines of S XVI, Si XIII, Mg XI, and Ne IX, and four Fe XVII lines. The theoretical wavelengths for each triplet are listed in the second column of the table. Errors represent 68% confidence limits.

Liefke et al. (2008) applied this technique to groups of H-like Ly α and He-like resonance lines for lines that can be easily measured from Chandra HETGS spectra. The abundance ratio of two elements is defined as the following:

$$\frac{A_1}{A_2} = \frac{f(A_1^{Z-1}) + C_1 * f(A_1^Z)}{C_2 * f(A_2^{Z-1}) + C_3 * f(A_2^Z)} \tag{3.5}$$

A_1 and A_2 are the two elements whose abundances are being compared, f(A^Z) is the flux measurement of the H-like ion, and f(A^{Z-1}) is the flux measurement of the He-like ion for both of the elements respectively. The constants C_1, C_2, and C_3 are listed in Table III.7. These coefficients, determined by Liefke et al. (2008), convert the measured line fluxes in photon flux units to absolute abundance ratios that are independent from any solar photospheric abundances.

A similar equation can be used to estimate abundance ratios relative to iron. In

Table III.7. Coefficients for abundance ratios (Liefke et al., 2008)

Ratio	C_1	C_2	C_3	C_4	C_5
S/Si	+0.42	0.15	+0.85	...	...
Mg/Ne	+0.18	-0.08	+0.87	...	...
Si/Mg	+0.32	+0.05	+0.86	...	...
Ne/Fe	...	...	...	+34.71	+0.46
Mg/Fe	...	...	...	+67.73	-0.30

Note. — Coefficient were derived by Liefke et al. (2008) and are used in Eqs. 5 and 6.

this case, four different Fe XVII lines are used. In order to determine abundance ratios that include Fe, one can determine the estimate of Fe abundance from the sum of four Fe XVII lines at 15.01 Å , 16.78 Å , 17.05 Å , 17.09 Å . The ratios involving Fe are determined by the following equation:

$$\frac{A}{A_{Fe}} = \frac{C_4 * (f(A^{Z-1} + C_5 * f(A^Z))}{\sum f(FeXVII)} \tag{3.6}$$

A is the element being compared to iron, and f(A^{Z-1}) is the flux of the He-like line and f(A^Z) for a given element. The coefficients C_4 and C_5 are listed in Table III.7.

The ratios calculated using Equations 1 and 2, are in terms of the abundances of the individual elements in each observation. In order to convert this to solar abundances, we used the ratios of solar photospheric abundances theoretically determined

Table III.8. Abundance ratios for combined spectra

Star	Mg/Ne	Si/Mg	S/Si	Ne/Fe	Mg/Fe
Hen3-600	0.15 ± 0.04	1.99 ± 0.75	2.27 ± 0.98	8.94 ± 1.60	1.44 ± 0.47
HIP 92680	0.23 ± 0.02	0.85 ± 0.10	1.70 ± 0.45	5.03 ± 0.46	1.06 ± 0.21
BO Mic 2536	0.05 ± 0.02	1.30 ± 0.39	3.01 ± 1.78	3.25 ± 0.74	0.10 ± 0.08
BO Mic 3491	0.07 ± 0.02	0.75 ± 0.26	1.09 ± 1.06	3.91 ± 0.75	0.15 ± 0.09
SU Aur	0.45 ± 0.08	1.01 ± 0.14	1.01 ± 0.29	6.72 ± 1.77	0.99 ± 0.82
SU Aur - fl	0.64 ± 0.09	1.19 ± 0.12	1.55 ± 0.25	6.47 ± 1.45	3.88 ± 1.08
SU Aur - qu	0.38 ± 0.13	1.11 ± 0.35	0.78 ± 0.75	6.28 ± 3.19	2.69 ± 1.93
HD 98800	0.09 ± 0.02	2.65 ± 1.01	0.21 ± 0.66	6.66 ± 0.88	0.64 ± 0.21
HD 98800 - fl	0.07 ± 0.05	1.31 ± 0.81	1.07 ± 1.56	12.3 ± 3.85	0.12 ± 0.53
HD 98800 - qu	0.10 ± 0.03	10.8 ± 7.70	0.27 ± 0.63	8.49 ± 1.26	1.14 ± 0.35
TW Hya	0.08 ± 0.03	2.44 ± 1.72	0.56 ± 0.81	3.15 ± 0.51	0.67 ± 0.26
TW Hya - fl	0.07 ± 0.04	1.22 ± 0.67	—	15.6 ± 5.03	0.30 ± 0.48
TW Hya - qu	0.03 ± 0.03	1.37 ± 1.73	—	19.9 ± 3.14	0.15 ± 0.24
V824 Ara C	0.27 ± 0.01	0.99 ± 0.05	1.78 ± 0.21	5.00 ± 0.24	1.35 ± 0.11
V987 Tau	0.32 ± 0.05	0.94 ± 0.14	0.68 ± 0.47	4.37 ± 0.64	1.45 ± 0.35
V987 Tau - fl	0.34 ± 0.07	1.09 ± 0.20	0.44 ± 0.45	5.86 ± 1.31	1.76 ± 0.63

by Asplund et al. (2005). Each element was calculated to have an abundance relative to hydrogen, which has an abundance of 10^{12} (Ne = $10^{7.84} \pm 10^{0.06}$, Mg = $10^{7.53} \pm 10^{0.09}$, Si = $10^{7.51} \pm 10^{0.04}$, S = $10^{7.14} \pm 10^{0.05}$, Fe = $10^{7.45} \pm 10^{0.05}$). By dividing each ratio by a correction factor determined by the solar photospheric abundances, we derive abundance ratios relative to solar (Table III.8).

Table III.8 (cont'd)

Star	Mg/Ne	Si/Mg	S/Si	Ne/Fe	Mg/Fe
V987 Tau - qu	0.27 ± 0.06	0.78 ± 0.20	0.96 ± 0.76	3.85 ± 0.80	1.29 ± 0.46
DoAr21	0.58 ± 0.28	1.96 ± 0.43	2.48 ± 0.49	—	—
DoAr21 - fl	0.30 ± 0.01	0.96 ± 0.20	2.13 ± 0.49	3.59 ± 3.62	—
DoAr21 - qu	0.02 ± 0.03	1.52 ± 0.75	1.06 ± 0.63	—	—

Note. — Each ratio has been multiplied by the solar photospheric abundances stated by Asplund et al. (2005), Mg/Ne(0.49), Si/Mg(0.95), S/Si(0.43), Ne/Fe(2.45), Mg/Fe(1.2).

The most notable result from this particular set of stars is that the Ne/Fe ratio is quite large. Having overabundant neon with respect to iron is different from what is found in previous studies of other active stars (e.g., Huenemoerder et al. (2001)). The Ne/Fe ratios for the flaring and quiescent states are significantly larger for TW Hya and HD 98800 but with larger errors as well. For SU Aur and V987 Tau, the flaring and quiescent states of each observation have similar abundance ratios within the errors. For TW Hya and HD 98800, the ratios significantly change from the ratios determined from the full spectrum and those determined from the flaring and quiescent states.

Using the technique described in Drake & Testa (2005), we were also able to calculate the Ne/O abundance ratio using the Ne IX He-like resonance, Ne X Lyman α, and O VIII Lyman α lines, listed in Table III.9. From Table III.9, we see that only TW Hya in quiescence, and HD 98800 and DoAr 21 in their flaring states, show

Table III.9. Ne/O abundance ratios for combined spectra

Star	Ne IX He-r	Ne X Lyα	O VIII Lyα	Ne/O
λ (Å)	13.42	12.14	18.97	
TW Hya	2.26 ± 0.27	1.24 ± 0.10	3.61 ± 0.33	0.68 ± 0.14
TW Hya - fl	1.71 ± 0.56	2.25 ± 0.24	3.72 ± 0.65	0.55 ± 0.33
TW Hya - qu	2.73 ± 0.33	1.51 ± 0.13	3.27 ± 0.39	0.90 ± 0.16
SU Aur	0.10 ± 0.07	0.82 ± 0.09	0.65 ± 0.15	0.34 ± 0.41
SU Aur - fl	0.06 ± 0.06	1.25 ± 0.11	0.75 ± 0.19	0.33 ± 0.38
SU Aur - qu	0.05 ± 0.06	0.63 ± 0.12	0.31 ± 0.19	0.45 ± 0.81
HD 98800	0.56 ± 0.08	1.08 ± 0.07	2.24 ± 0.23	0.32 ± 0.16
HD 98800 - fl	0.61 ± 0.19	1.22 ± 0.16	0.91 ± 0.27	0.87 ± 0.39
HD 98800 - qu	0.54 ± 0.09	1.04 ± 0.08	1.39 ± 0.17	0.50 ± 0.18
V987 Tau	0.22 ± 0.06	1.07 ± 0.08	1.01 ± 0.16	0.37 ± 0.23
V987 Tau - fl	0.26 ± 0.09	1.13 ± 0.13	0.82 ± 0.20	0.53 ± 0.35
V987 Tau - qu	0.13 ± 0.07	1.03 ± 0.10	1.14 ± 0.24	0.25 ± 0.34
DoAr21 - fl	0.50 ± 0.46	2.36 ± 0.49	1.20 ± 0.33	0.71 ± 0.64
Hen3-600	0.30 ± 0.06	0.56 ± 0.05	0.98 ± 0.14	0.39 ± 0.21
HIP 92680	0.72 ± 0.12	3.19 ± 0.13	4.16 ± 0.31	0.29 ± 0.13

a high Ne/O ratio, and the latter two have significant errors on the abundance ratio that do not distinguish them from the rest of the sample. The average Ne/O ratio for this sample of stars is 0.44, similar to what was found by Drake & Testa (2005) with another sample of twenty-one coronally active cool stars. These results will be discussed at length in §4.2.5.

Table III.9 (cont'd)

Star	Ne IX He-r	Ne X Lyα	O VIII Lyα	Ne/O
V824 Ara C	3.23 ± 0.27	10.2 ± 0.20	14.36 ± 0.49	0.33 ± 0.07
BO Mic 2536	2.00 ± 0.47	4.91 ± 0.40	37.11 ± 5.2	0.07 ± 0.23
BO Mic 3491	2.64 ± 0.52	4.49 ± 0.36	34.31 ± 4.9	0.10 ± 0.22

Note. — All fluxes are in units of erg cm^{-2} s^{-1}. The ratios were calculated by the method described in Drake & Testa (2005).

CHAPTER IV

DISCUSSION

4.1 Imaging Spectroscopy of V710 Tau

4.1.1 *Spatially-resolved vs. unresolved X-ray spectroscopy of the binary*

The results of our spectral fitting for the individual X-ray-emitting components of the V710 Tau wTTS/cTTS binary (§3.2) can be compared with previous results obtained for this system from XMM-Newton EPIC observations, in which the binary is unresolved. In the spectral analysis performed by Favata et al. (2003), the V710 Tau N/S combined X-ray spectrum was well-fit by an absorbed two-component plasma model, with $kT_1 = 0.63 \pm 0.05$ keV and $kT_2 = 1.24 \pm 0.10$ keV and a coronal metal abundance Z = 0.22 ± 0.07 $Z_{\odot}$. Favata et al. (2003) further improved the model fit by varying the individual relative metal abundances; this analysis suggested a Ne abundance of 0.98 ± 0.45 $Z_{\odot}$, nearly a factor of five above the derived Fe abundance. The results from Favata et al. (2003) are nearly identical to ours for both temperature and abundance values and the indication of enhanced Ne, which strongly suggests that the composite spectrum modeled by Favata et al. (2003) is dominated by the X-ray spectrum of V710 Tau N.

Giardino et al. (2006) fit the unresolved XMM-Newton EPIC low-resolution spectra of V710 Tau for eleven observations. Each observation was fit independently with an absorbed, single-component plasma model, resulting in best-fit values of kT ranging from 0.41 ± 0.24 to 1.03 ± 0.06 keV and N_H ranging from 0.10 ± 0.18 x 10^{22}

cm^{-2} to 0.71 $\pm$ 0.27 x 10^{22} cm^{-2}.

Our results are consistent with both the Favata et al. (2003) and Giardino et al. (2006) analyses, but further indicate *(a)* in quiescence, *both* components of the V710 Tau binary are relatively soft ($kT \sim 1.0$ keV) X-ray sources and *(b)* harder ($kT \sim 2.5$ keV) X-ray emission is only present during the apparent flare on V710 Tau N in 2004 December, based on both one- and two-component plasma model fits. The latter result suggests that neither binary component was flaring during the 2000 September and 2004 March XMM observations analyzed by Favata et al. (2003) and Giardino et al. (2006). Indeed, these authors report no variability in the unresolved V710 Tau X-ray source during these XMM exposures.

Our spectral fitting results for V710 Tau N are also consistent with the findings of Wolk et al. (2005), who used two-component plasma models to describe X-ray emission from strongly flaring T Tauri stars in Orion. Wolk et al. (2005) found that a "hot" plasma component (median $kT \sim 7$ keV) in conjunction with a "cool" plasma component (kT ~0.7 - 0.9 keV) describes such sources well and, furthermore, that the cool component is unaffected by the magnetic activity that presumably causes the flaring. The same behavior is apparent for V710 Tau N.

4.1.2 *Accretion signatures in the X-ray emission from V710 Tau?*

Evidence is growing that stellar mass accretion plays a role in the production of some of the X-rays from some T Tauri stars. Some of this evidence comes from analysis of TTS X-ray plasma temperatures. Kastner et al. (2002) and Huenemoerder et al. (2007) interpreted the presence of very low temperature (0.15-0.25 keV) plasmas

in high-resolution X-ray spectra of TW Hya and the borderline wTTS/cTTS binary Hen3-600, respectively, as an accretion signature. High-resolution X-ray spectra of other cTTS have also revealed the presence of "soft excesses" associated with these stars that are ascribed to accretion processes (Telleschi et al., 2007b). A complementary effect is apparently seen in low-resolution (CCD) X-ray spectroscopy. Specifically, CCD spectral studies of statistically significant TTS samples indicate a trend wherein cTTS exhibit a deficit of X-ray emission relative to wTTS; this deficit, which has also been explained in terms of disk stripping (e.g., Jardine et al. (2006); Gregory et al. (2007)) or field complexity in the photosphere (e.g., Johns-Krull (2007)), is evidently accompanied by an enhancement of high-T_X emission in cTTS (Telleschi et al. 2007a and references therein). Telleschi et al. (2007a) interpret these results as indicating that the accreting material in cTTS cools active regions to low temperatures, decreasing the X-ray luminosity — while increasing the average X-ray temperature — of cTTS relative to wTTS.

Though one must be cautious in placing results for individual objects in the context of statistical trends, our spectral modeling results for the individual components of the V710 Tau system are consistent with the contrast in T_X between cTTS and wTTS that is apparent in the XMM-Newton Taurus cloud survey data presented in Telleschi et al. (2007a). Specifically, in both quiescent and flaring states, V710 Tau N consistently exhibits higher plasma temperatures than V710 Tau S (Table II.2), and these results for T_X for V710 Tau N and S fall within the respective ranges determined for cTTS and wTTS in Taurus (see Figure 14 of Telleschi et al. (2007a)).

Our results, like those of Favata et al. (2003), point to the likelihood of enhanced

Ne/Fe abundance ratios in the X-ray emitting plasma of V710 Tau N and, possibly, V710 Tau S. In the case of the cTTS TW Hya, such an anomalous Ne/Fe ratio has been interpreted as an X-ray signature of accretion (e.g., Stelzer & Schmitt (2004)). However, high Ne/Fe ratios have also been observed in coronally active stars, and for those stars the enhancements are usually attributed to the inverse FIP (first ionization potential) effect (e.g., Argiroffi et al. (2005)). The plasma Ne/O ratio may be a more effective diagnostic of accretion activity (Drake et al. (2005)), but we are unable to constrain this ratio for either component of the V710 Tau binary from our observations.

4.2 High Resolution X-ray Spectroscopy

4.2.1 *Density and temperature implications from the He-like triplet ratios*

For the stars in our sample, several previous studies have reported similar measurements. However, the goal of this project is to analyze this set of the nine stars (ten HETGS observations) in our sample in a globally consistent way. This is the first consistent comparison of these stars in which the data has been reduced and analyzed using the same techniques. In this section, we will compare our results to previous results and then present our interpretation of our results.

The He-like triplets (forbidden (f), intercombination (i), and resonance (r) lines of Si, Mg, and Ne for each observation were used to determine the ratios R = f/i and G = $(f+i)/r$. Using theoretical calculations from Brickhouse (private communication), the R and G ratios can be correlated with densities and temperatures. Figures 4.1,

4.2 and 4.3 depict the G vs. R ratios for Si XIII, Mg XII and Ne IX He-like ions respectively. The temperature-sensitive G ratios are plotted along the x-axes, and the density-sensitive R ratios are plotted on the y-axes. Overplotted are grids consisting of temperature, in log T approximately parallel to the x-axis, and density in log n_e approximately parallel to the y-axis for the three He-like ions. The grid values correspond to the temperature and density of an X-ray plasma that would produce the given *r*, *i*, and *f* line fluxes for each of these three ionized species respectively, that in turn, would yield the given R and G ratios. The theoretically calculated range of temperatures (log T of 6.5-7.75 K, 6.25-7.5 K, and 6.25-7.25 K for Si XIII, Mg XI, and Ne IX, respectively) and densities (log n_e of 12.25-14.50, 11.0-14.5, and 10.75-13.25 for Si XIII, Mg XI, and Ne IX, respectively) represented by the grids are indicative of the environments thought to be capable of producing these He-like emission lines, according to the model calculations of Brickhouse. Thus, by plotting G versus R, one obtains an estimate of the temperature and density of the X-ray emitting plasma that is producing that particular He-like triplet.

For each observation of each star, we plotted the G versus R ratio with one-sigma error bars for the Si XIII, Mg XI, and Ne IX triplets (Figures 4.1 - 4.3). Each observation falls into one of four categories based on the position of the point (G, R) on the plots. One, the calculated R and G ratios fall on the grid, in which case the temperature and density values are quoted with one-sigma error bars (Table III.4). Two, the G ratio lies within the temperature range predicted by the APEC catalog, but the R ratio does not. For this case, we estimate a temperature with one-sigma error bars, and if a three-sigma R value falls on the grid, we estimate an upper limit

for the density. Similarly for the third case, if R ratio corresponds to a density in the range of predicted densities, but the temperature does not, we estimate densities with one-sigma error bars and three-sigma upper limits for the temperature. Last, if the (G, R) point for a given observation is more than three-sigma from the theoretically predicted values shown on the grid for a given ion, we make no temperature or density estimate for that observation. Table III.4 in Chapter 3 contains a list of the R and G ratios for each observation as well as the inferred temperatures and densities based on the criteria above. We note two important things, based on Figures 4.1, 4.2, and 4.3. First, not all measured (G, R) points fall within the theoretically predicted temperature and density ranges, even if the line flux measurements for the R and G ratios are robust (e.g., V824 Ara C). Second, no obvious trend emerges as far as the physical properties of the X-ray emitting plasmas of the various types of stars in our study. The individual results for each star are discussed below. In each section for each star, we first discuss the densities inferred from the R ratios of Si XIII, Mg XI, and Ne IX, then the inferred temperatures from the G ratios of each ion, and finally the consistency and implications of each set of measurements.

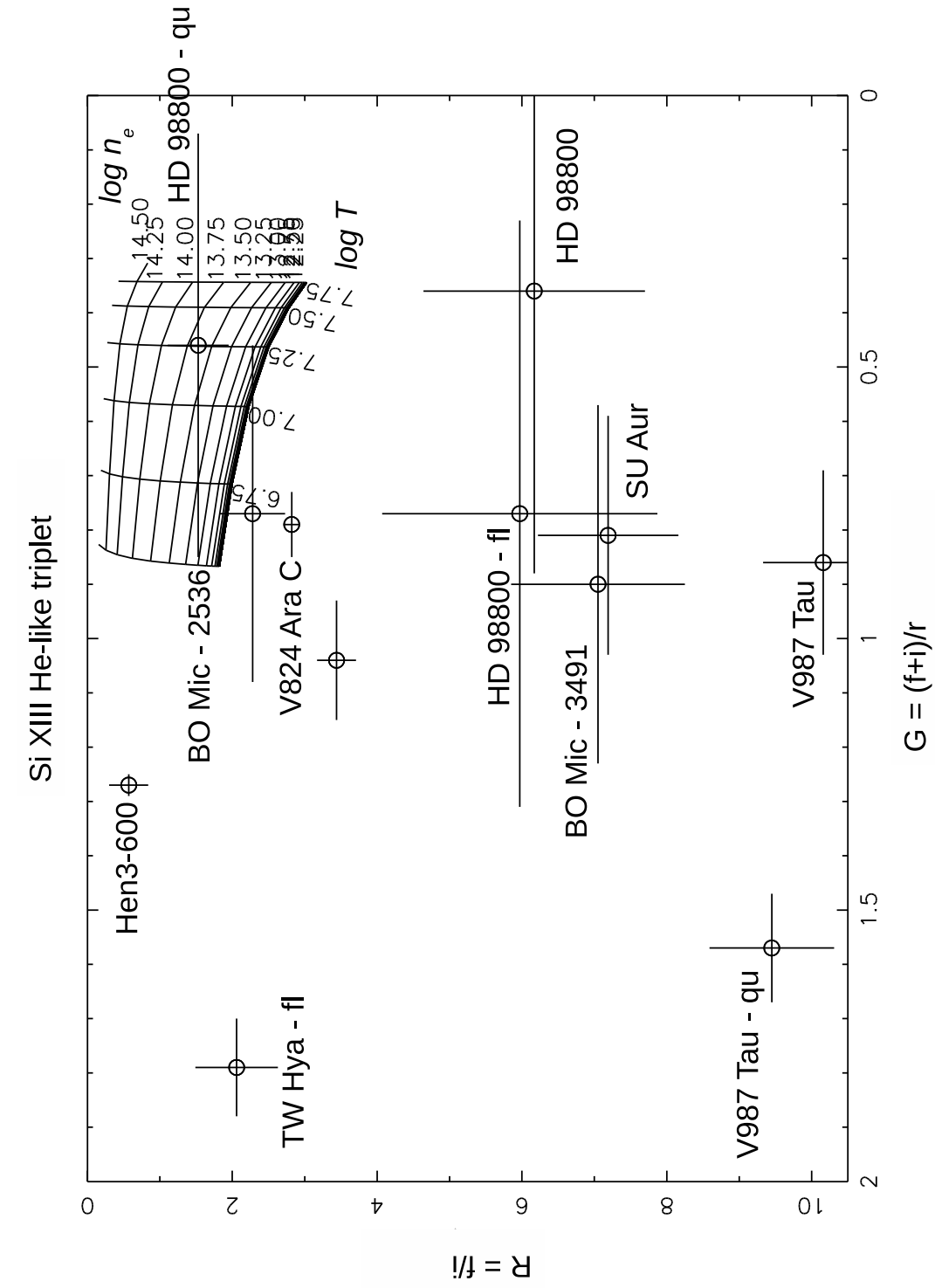

Figure 4.1: The corresponding grid consists of lines of constant log T and constant log n_e from Brickhouse (private communication).

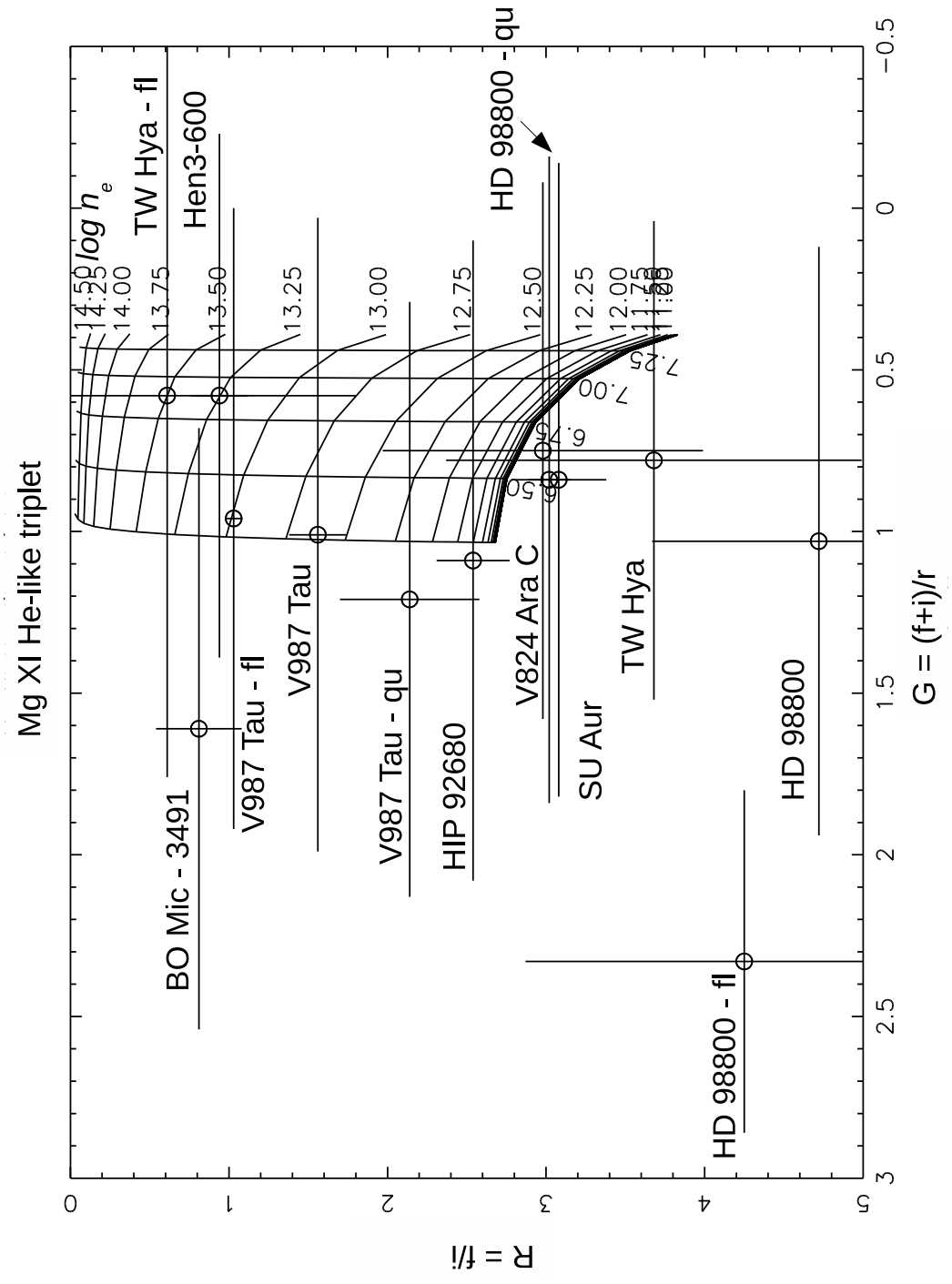

Figure 4.2: See Figure 4.1 caption for more detail.

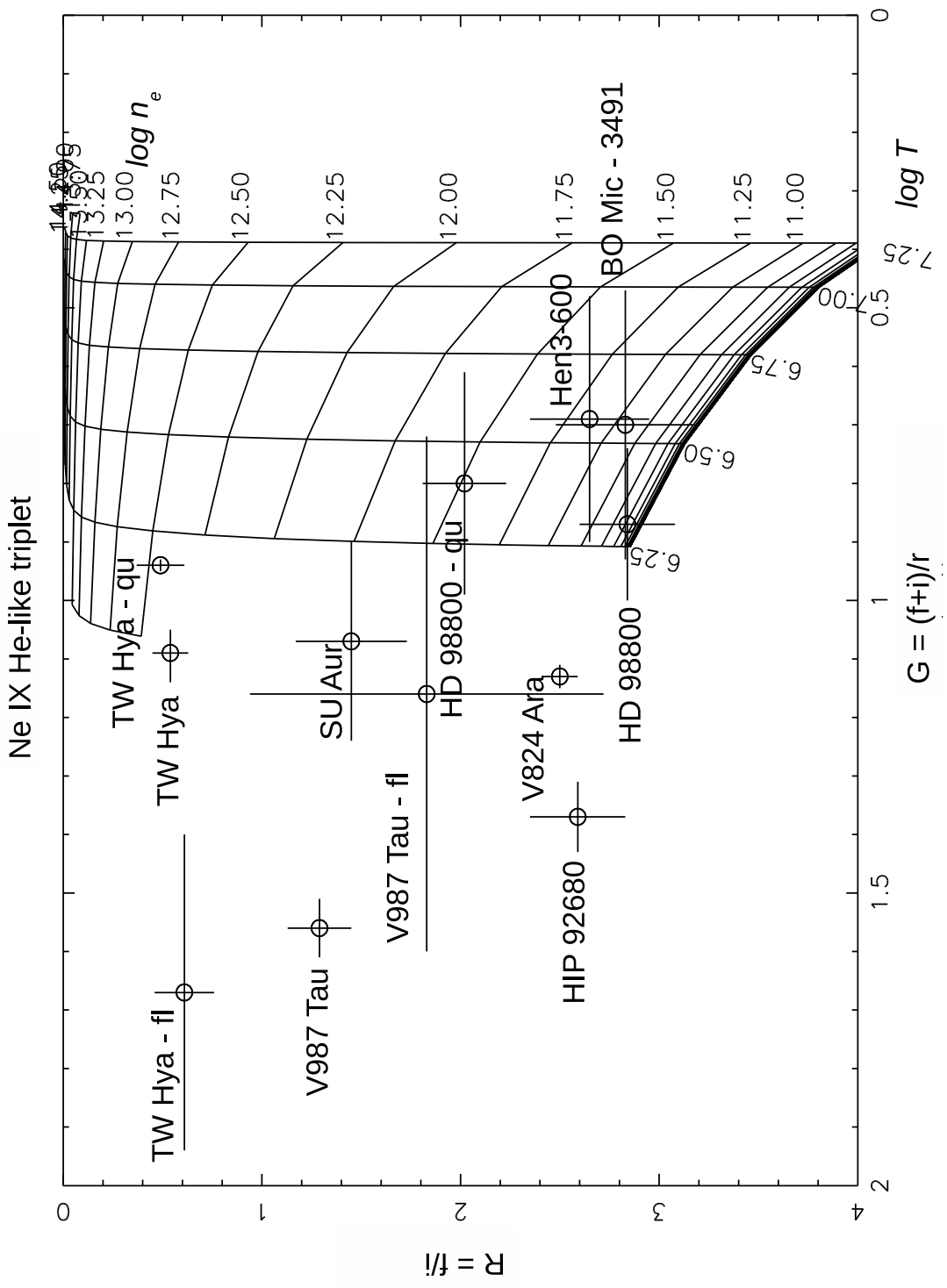

Figure 4.3: See Figure 4.1 caption for more detail.

4.2.1.1 TW Hya

TW Hya is the most well studied star with high-resolution X-ray spectroscopy in our sample, and arguably has the most unique X-ray properties. TW Hya is a strongly accreting cTTS (Hα EW $\geq$ -220 Å). Kastner et al. (2002) were the first to observe TW Hya with Chandra HETGS. They studied both the flaring and quiescent states of the 48 ks observation, but found little difference in either T or n_e between the two states, based on observations of the Ne IX He-like triplet. However, both states indicate a ubiquitously unusually high density, at least two orders of magnitude higher than densities inferred for other active late-type stars observed with Chandra HETGS. They suggest that the unusually high density of TW Hya is associated with mass accretion from its circumstellar disk. Based on high-resolution observations using RGS on XMM-Newton, Stelzer & Schmitt (2004) also find $n_e \sim 10^{13}$ cm^{-3} based on He-like triplets of nitrogen (N VI), oxygen (O VII), and neon (Ne IX). The same XMM-Newton RGS data set was reanalyzed by Robrade & Schmitt (2006). They similarly find a density three orders of magnitude higher than the low-density limit (Ness et al., 2002b) of the R = (f/i) ratio. They suggest this high density is due to an additional hot ($\sim$10 MK) component and, like Kastner et al. (2002), choose an accretion shock as a more likely scenario for generating the X-ray emitting plasma than strong UV radiation fields that likely cannot be produced in the photospheres of cool stars (Robrade & Schmitt, 2006).

We measured the f, i and r lines for Si XIII, Mg XI, and Ne IX for the full spectrum, and separate flaring and quiescent state spectra, for TW Hya. The errors

for the Si XIII and Mg XI He-like lines make it difficult to constrain a density for the full spectrum and quiescent state due to low signal-to-noise ratios; however the R = (f/i) ratios for Ne IX in all three states indicate log $n_e \sim$ 12.15 - 12.75. In addition, the density inferred from the Si XIII measurements of the flaring state, log $n_e = 13.75 \pm 0.5$, is also consistent with the density inferred from the Ne IX triplet. Although the error bars overlap, the quiescent state plasma has a slightly lower R ratio than the flaring state plasma. The density results from the Ne IX triplet are in good agreement with results from the studies of Kastner et al. (2002) and Stelzer & Schmitt (2004). In addition, our analysis of the Si XIII R ratio also confirms a high density present in the X-ray emitting plasma of TW Hya.

The inferred temperatures for TW Hya from the G = (f+i)/r ratio are more difficult to constrain. One-sigma errors in the Mg XI He-like triplet lines for all three states span the entire range of plausible temperatures. The limited signal-to-noise ratios in the Mg XI triplet may be due to the resonance line blending with the Ne X H Lyα series, since the Mg XI triplet measurements have uniformly large errors in the G ratio for all of our sources. The Si XIII line indicates unreasonably cool temperatures, indicating either poor statistics in the measurements or difficulties in determining the atomic data. Although all three spectra (full observation, flaring state and quiescent state) of TW Hya have low R ratios as determined from the Ne IX He-like triplets, the G ratios indicate quite a bit of variation in temperature. Analysis of the line ratios measured from the full spectrum of TW Hya indicate a temperature of log T <6.25, consistent with the findings of Kastner et al. (2004). The flaring state Ne IX He-like triplet indicates a very cool temperature with an

upper limit of log T <6.35, and the quiescent state Ne IX He-like triplet indicates a temperature of log T ∼6.25 with very small error. All three Ne IX G ratios for the full spectrum, flaring and quiescent states, are in good agreement and indicate an X-ray emitting plasma with a log T <6.35. All high-resolution X-ray observations thus far — including ours — consistently indicate a relatively cool and high-density plasma in TW Hya. Based on the temperatures inferred from the G-ratios of Si XIII, Mg XI, and Ne IX, we do not find evidence of a hotter plasma component in TW Hya seen in the XMM-Newton observation of TW Hya by Stelzer & Schmitt (2004).

4.2.1.2 SU Aur

The majority of the SU Aur observation is dominated by a large flare; as a result, after separating the flaring and quiescent state spectra, the remaining counts in the quiescent spectrum are insufficient to ascertain line fluxes so we instead measure the relevant line fluxes from the full spectrum. SU Aur was previously observed by XMM-Newton and the RGS spectrum was analyzed by Robrade & Schmitt (2006).

Our measurements of the Si XIII He-like triplet provide no constraints on either the temperature or density due to large uncertainty in the line measurements, most likely due to the strong continuum emission in this region of the spectrum. The Mg XI triplet does provide an upper limit on the density of log n_e <12.75. The Ne IX does provide a good constraint on the density, $n_e = 11.75 \pm 0.15$, which is consistent with the Mg IX upper limit, and similar to densities found in other coronally active stars. The Ne IX triplet G ratio also places an upper limit on the temperature of log T <6.85. Although SU Aur is known to be actively accreting material, we do not find

any evidence of a high density plasma indicative of accretion, as seen for TW Hya. Since the spectrum of SU Aur is dominated by a flare, the X-ray emission produced may be largely coronal in origin.

4.2.1.3 HD 98800

HD 98800 was first observed by Chandra HETGS and the results were published in comparison to TW Hya in Kastner et al. (2004). The R ratio determined by Kastner et al. (2004) from the Ne IX He-like triplet is considerably higher than that found for TW Hya. The R ratio indicates a lower density than found for TW Hya of log n_e $\sim$11.25. Since this density is consistent with those found in coronally active sources, Kastner et al. (2004) conclude that a coronally active X-ray emitting plasma is the dominant source of X-ray emission in HD 98800.

Like TW Hya, HD 98800 exhibits significant flaring so, again, we measured the He-like triplets of Si XIII, Mg XI and Ne IX for the full spectrum and also from spectra derived from the flaring and quiescent states. Only the quiescent state observation of the Si XIII and Ne XI lines provide robust density measurements but they are not in good agreement. The Si XIII triplet suggests a density of log n_e = 13.6 $\pm$ 0.4 while the Ne IX triplet suggests a density of log n_e = 11.5 $\pm$ 0.13. The upper limits set by the Si XIII triplet for the full spectrum and flaring state are similarly high, log n_e <14.1 and log n_e <14.5 respectively. The upper limits set by the Mg XI triplet for the flaring and quiescent states are also high (log n_e <14.25 and log n_e <14.5), but this may be caused by larger uncertainty in these measurements. The Mg XI and Ne IX triplet R ratios derived from the full spectrum set an upper limit of log n_e

<12.75 for the density. This is consistent with the other upper limits and also with the lower density indicated by the Ne IX triplet for the quiescent state. Since the independent measurements of the R ratio from the Si XIII and Ne IX triplets in the quiescent state indicate densities nearly two orders of magnitude apart, there may be two X-ray emitting plasmas of differing densities detected during the quiescent state. However, since Kastner et al. (2004) also find a lower density from the Ne IX triplet, it is also possible that the high density obtained from the quiescent state Si XIII measurement is due to a systematic error in measuring the Si line fluxes.

For both the Si XIII and Mg XI G ratios, the one-sigma error bars span the entire temperature range except for the flaring state observation of the Mg XI triplet, for which we can place an upper limit of log T <6.7 on the temperature. For the Ne IX triplet, the quiescent state temperature, log T = 6.3 ± 0.3, does not differ from the temperature derived from the full spectrum, log T = 6.3 ± 0.2. These three measurements are consistent with one another and indicate that a cool plasma is responsible for the emission of the Mg XI and Ne IX triplets during both flaring and quiescence.

4.2.1.4 Hen 3-600

Hen 3-600 is a multiple T Tauri star system whose components were individually studied in depth by Huenemoerder et al. (2007). For our study, we did not separate the components of the 1.4" binary. Huenemoerder et al. (2007) find a R = (f/i) value of ∼1 ± 0.5, corresponding to a log n_e ∼ 10.75 for the O VII He-like triplet and an upper limit of log n_e <11.75 from the Ne IX triplet. The n_e derived from our Ne

IX He-like triplet indicated a similar density, log n_e = 11.15 ± 0.15. The Mg XI triplet yields a density of log n_e = 13.25 ± 0.5, an order of magnitude higher than the density found with the Ne XI triplet. The Si XIII triplet again yields a very high density (log n_e = 14.00 ± 0.50), but the corresponding G ratio yields a temperature outside the theoretically probable temperature ranges which gives us some concern that we have a yet-unidentified systematic error in measuring the Si XIII line fluxes. The Ne IX triplet G ratio denotes a relatively cool temperature log T = 6.55 ± 0.35, which is consistent with the Mg XI temperature of log T ∼ 6.9, though the error spans the entire temperature range due to uncertainty in the resonance line measurement. Hen 3-600 A has a large Hα EW, indicating that it is most likely still accreting, which would be consistent with the high density measurements from Si XIII and Mg XI. However, the density derived from the Ne IX triplet, which is consistent with Huenemoerder et al. (2007), indicates a density more similar to coronally active sources that are not accreting. Since Hen 3-600 is a multiple system, it is possible that we are probing two different plasmas with different densities, one indicating accretion activity onto the cTTS component, and the other lower density plasma produced from coronal activity on either Hen 3-600 A or B.

4.2.1.5 V987 Tau

V987 Tau, a wTTS, shows significant flaring during the Chandra HETGS observation, so we analyzed the full spectrum and flaring and quiescent state spectra individually. The R ratios from the Si XIII triplet do not indicate a plasma density predicted by the APEC catalog. The densities from the Mg XI triplet are all in good

agreement, log $n_e = 13.0 \pm 0.1$, log $n_e = 12.0 \pm 0.5$, and log $n_e = 12.68 \pm 0.13$, for the flaring, quiescent and full spectra respectively. The quiescent state R ratio indicates a slightly lower density than the flaring state. The densities from the Ne IX triplet are also in good agreement with each other, log $n_e = 11.6 \pm 0.6$, log $n_e = 12.2 \pm 0.2$, and log $n_e = 11.88 \pm 0.13$, for the flaring, quiescent and full spectra respectively, but are lower than the densities predicted by the Mg XI triplet R ratio. The densities are more consistent with the densities found in coronally active stars, and we see no evidence for a high density plasma component that would be indicative of accretion activity.

The G ratio for the Si XIII triplet for the flaring state yields a high temperature of log T = 7.0 ± 0.25, whereas this triplet provides no constraint on the temperature for either the quiescent state or full observation. The errors in the Mg XI triplet again span the entire range of plausible X-ray temperatures predicted to produce Mg XI emission. The Ne IX triplet G ratio for the flaring state indicates a temperature in the range of log T = 6.25-7.25. Though the measurements of the G ratios for the quiescent state and full spectrum have low errors, the G ratios fall far below the predicted temperatures that produce the Ne IX lines. Since the temperature of the X-ray emitting plasma is notably cooler during quiescence than during the flared state, the emission from the cooler plasma may be suppressed during the flares.

4.2.1.6 HIP 92680

The R = (f/i) ratios for HIP 92680, also known as PZ Tel, have been previously measured by Argiroffi et al. (2004). Our measurements for the He-like triplets of Si

Table IV.1. Comparison of Argiroffi et al. (2004) He-like measurements

He-like triplet	Argiroffi et al. (2004) R = (f/i)	log n_e	this work R = (f/i)	log n_e
Si XIII	3.5 ± 2.1	< 13.5	3.44 ± 0.27	<13.1
Mg XI	1.7 ± 0.8	12.6 ± 0.6	2.54 ± 0.23	12.38 ± 0.12
Ne IX	3.0 ± 1.4	< 11.8	2.59 ± 0.24	10.8 ± 0.5

XIII, Mg XI, and Ne IX are all in good agreement with the Argiroffi et al. (2004) measurements of the same lines (Table IV.1) though we have been able to measure these lines to greater accuracy. The inferred densities we derive from the Mg XI and Ne IX triplets are in good agreement with the densities derived by Argiroffi et al. (2004).

Argiroffi et al. (2004) do not derive temperatures from G ratios in their study. We find that the X-ray emitting plasma of HIP 92680 has a cool temperature. The G ratio derived from the Si XIII triplet is log T <6.75. The Mg XI triplet again provides no constraint on the temperature due to uncertainty in the measurements, and the G ratio for Ne IX is below the range of theoretically predicted temperatures. The densities are consistent with coronally produced plasmas, which we expect since HIP 92680 is not actively accreting.

4.2.1.7 V824 Ara C

V824 Ara C is a companion to a binary system, V824 Ara A/B. All three components are members of the Beta Pictoris Moving Group, with an estimated age of ~ 12 Myr (Rebull et al., 2008). The HETGS spectrum of V824 Ara C is one of the most strongly exposed, partially due to its proximity (d = 31.4 pc). Audard et al. (2004) present a preliminary analysis of various He-like triplets in the HETGS observations of V824 Ara C and they find that the dominant X-ray emitting plasma has log $n_e <$ 10. They also note, however, that a high density plasma may exist in a small volume.

The R ratio from the Si XIII triplet is well constrained and indicates that the X-ray emitting plasma has a density below log n_e <13.1. The Mg XI triplet similarly indicates a low density, log $n_e < 11.5$. The Ne IX line fluxes in the V824 Ara C spectrum are very strong, and thus provide strong constraints on values of the R and G ratios. The density is well-constrained to a value of log $n_e = 11.75 \pm 0.05$, consistent with the upper limits placed on the densities derived from the Si XIII triplet, but higher than the upper limit placed by the Mg XI triplet and the density cited by Audard et al. (2004). Only the G ratio for the Si XIII triplet is well constrained and corresponds to a temperature of log T = 6.65 $\pm$ 0.1. Like our other observations, the G ratio for the Mg XI triplet has an error bar that spans the entire range of plausible temperatures. Although the value of the Ne IX G ratio has very low errors, the temperature indicated is below the range theoretically predicted to produce these Ne IX lines, implying some error in the theoretical predictions. From these results, the X-ray emitting plasma of V824 Ara C has a density comparable to other coronally

active sources and a relatively cool temperature that is likely on the order of a few million degrees.

4.2.1.8 BO Mic (a.k.a. Speedy Mic)

BO Mic is a rapidly rotating, zero-age main-sequence star. Ness et al. (2002b) find the X-ray plasma from BO Mic to be generally low density, with the O VII triplet indicating log $n_e < 11.2$ and the Ne IX triplet indicating log $n_e < 13.00$. They note that the Ne IX triplet measurements do not account for blending with iron lines, but also show for other sources in their sample that the plasma density derived from the Ne IX triplet is systematically higher than the O VII triplet even if blended lines are accounted for.

We separately analyzed two observations of BO Mic, each of ∼34 ks, observed one day apart, and the two observations yield surprisingly different results. From the Si XIII He-like triplet, we obtain an upper limit of log n_e <14.5, but the second observation R ratio falls below the theoretically predicted density range. For Mg XII, we see the opposite, the first observation yields a very high R ratio below the theoretically predicted temperature range, and the second observation yields a relatively high density of log $n_e = 13.1 \pm 0.3$. The Ne IX lines also yield a high R ratio below the predicted densities for the first observation and a log $n_e = 10.8 \pm 0.45$, which is in agreement with the upper limit derived by Ness et al. (2002b). Only the G ratio from the second observation provides any constraint on the temperature range and yields a temperature of log $T = 6.55 \pm 0.45$. Both the temperature and density derived from the Ne IX line fluxes in the second observation are consistent with coronally

active sources. The observations of BO Mic were taken a day apart, yet we find marked differences in the strengths of specific line fluxes. It is interesting that we were unable to resolve the Mg XI intercombination line in the first observation, and it is very strong in the second observation. A longer integration time observation of BO Mic may indicate whether this phenomenon is random variability or if there are two different plasmas producing the different Mg XI triplet line fluxes observed here.

4.2.2 *Correlation of R and G ratios with Hα EW*

To further analyze the R and G ratios, we plot these ratios against Hα EW(equivalent width), which serves as a proxy for accretion activity for young stars. If any significant correlation between accretion activity and either density or temperature exists, it should be apparent from Figures 4.4 - 4.6. No linear correlation is apparent from the data, but there are several interesting properties of individual sources and groups of sources.

4.2.2.1 R ratios and inferred densities

From the Si XIII R ratios, a high density (low R value) is apparent for TW Hya and Hen 3-600, the two stars in our sample with the highest Hα EW that are also accreting. However, SU Aur, BO Mic, V824 Ara C, and the quiescent state of HD 98800 also show high densities. TW Hya, HD 98800 and SU Aur have two distinct X-ray emitting plasmas of different densities in their flaring and quiescent states. From these three examples, the flaring state observation has an R ratio indicative of a slightly lower density than the quiescent state observation. This is also seen for

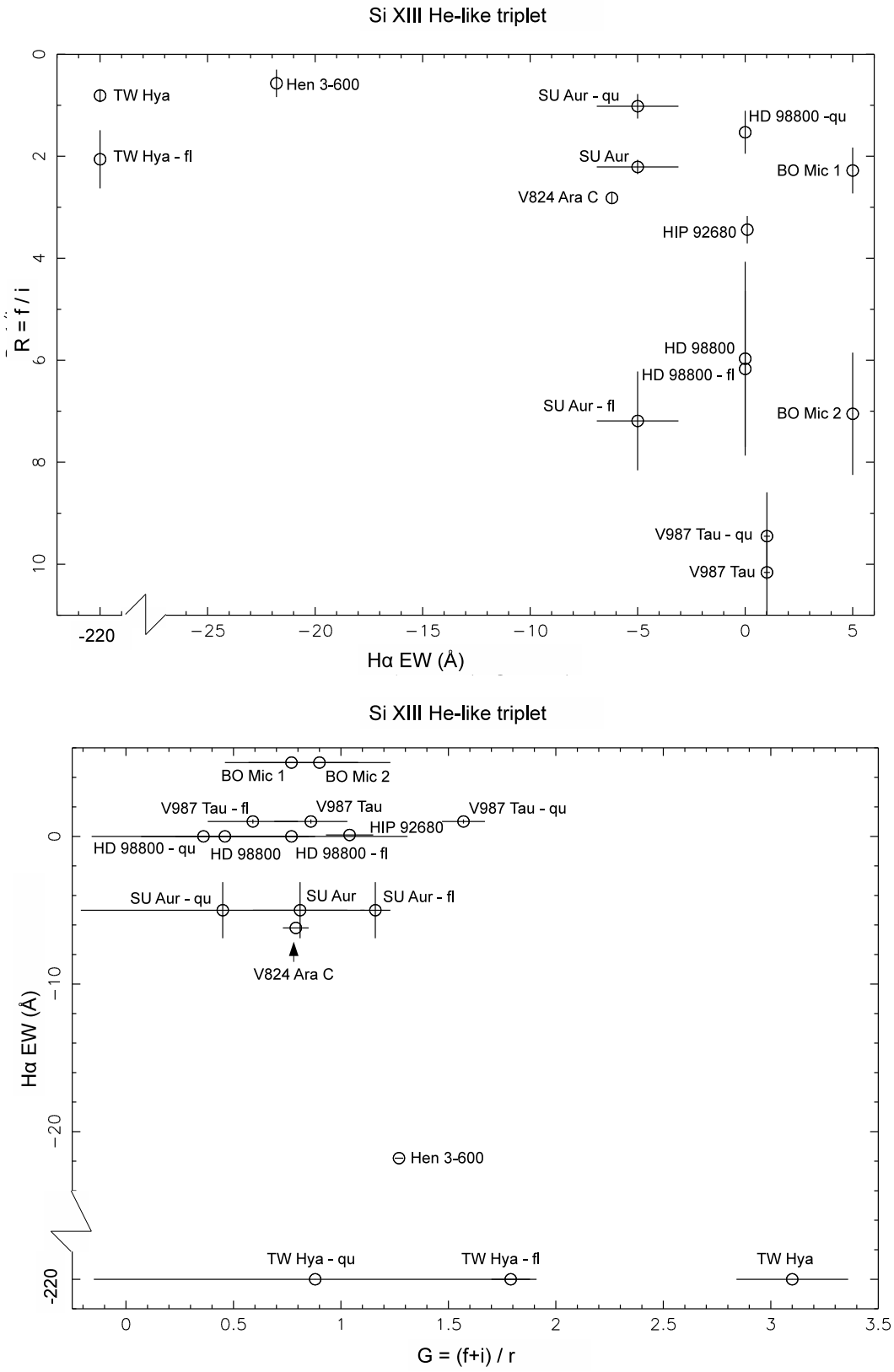

Figure 4.4: R and G ratio versus Hα EW for the Si XIII triplet

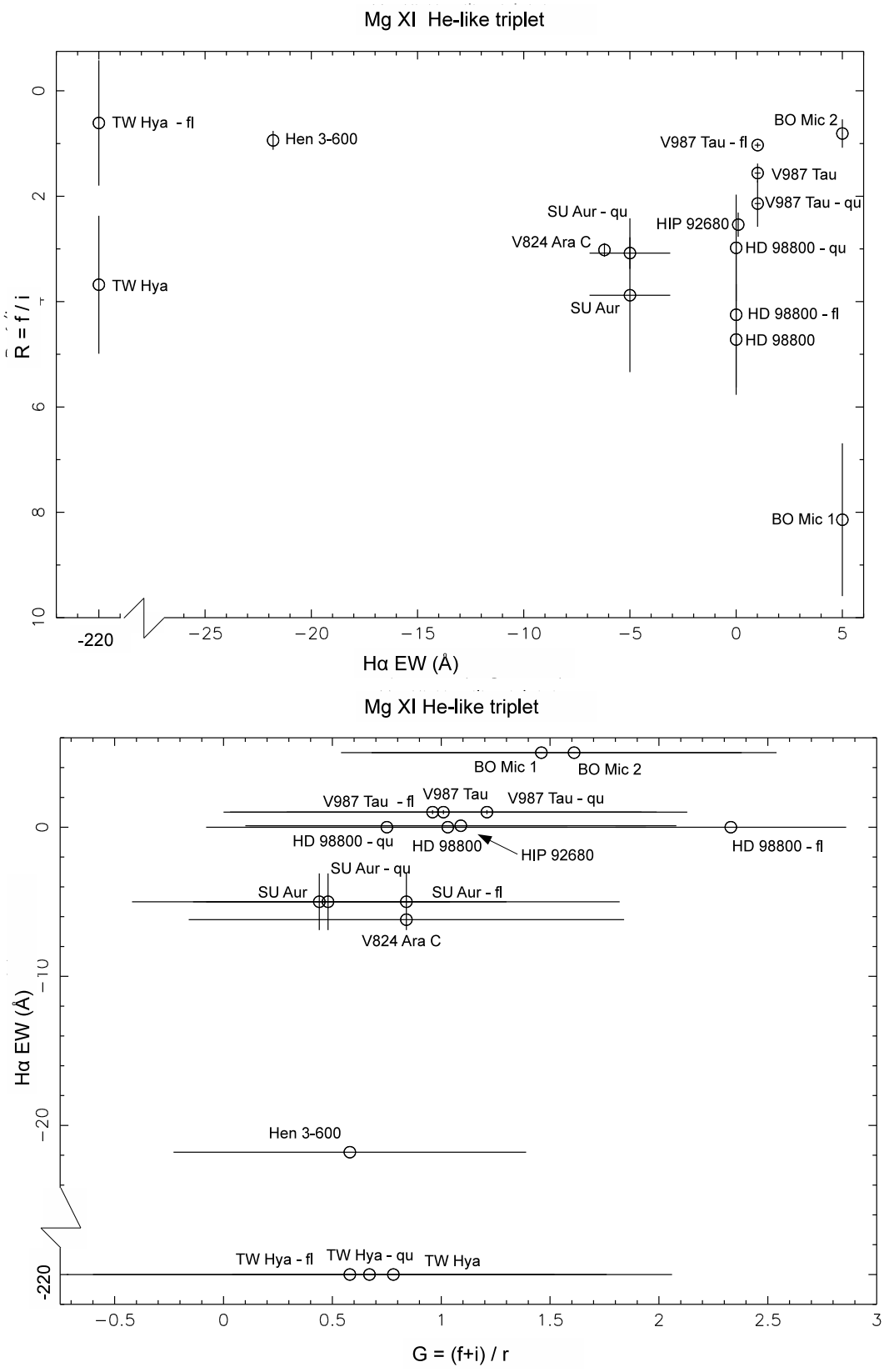

Figure 4.5: R and G ratio versus Hα EW for the Mg XI He-like triplet

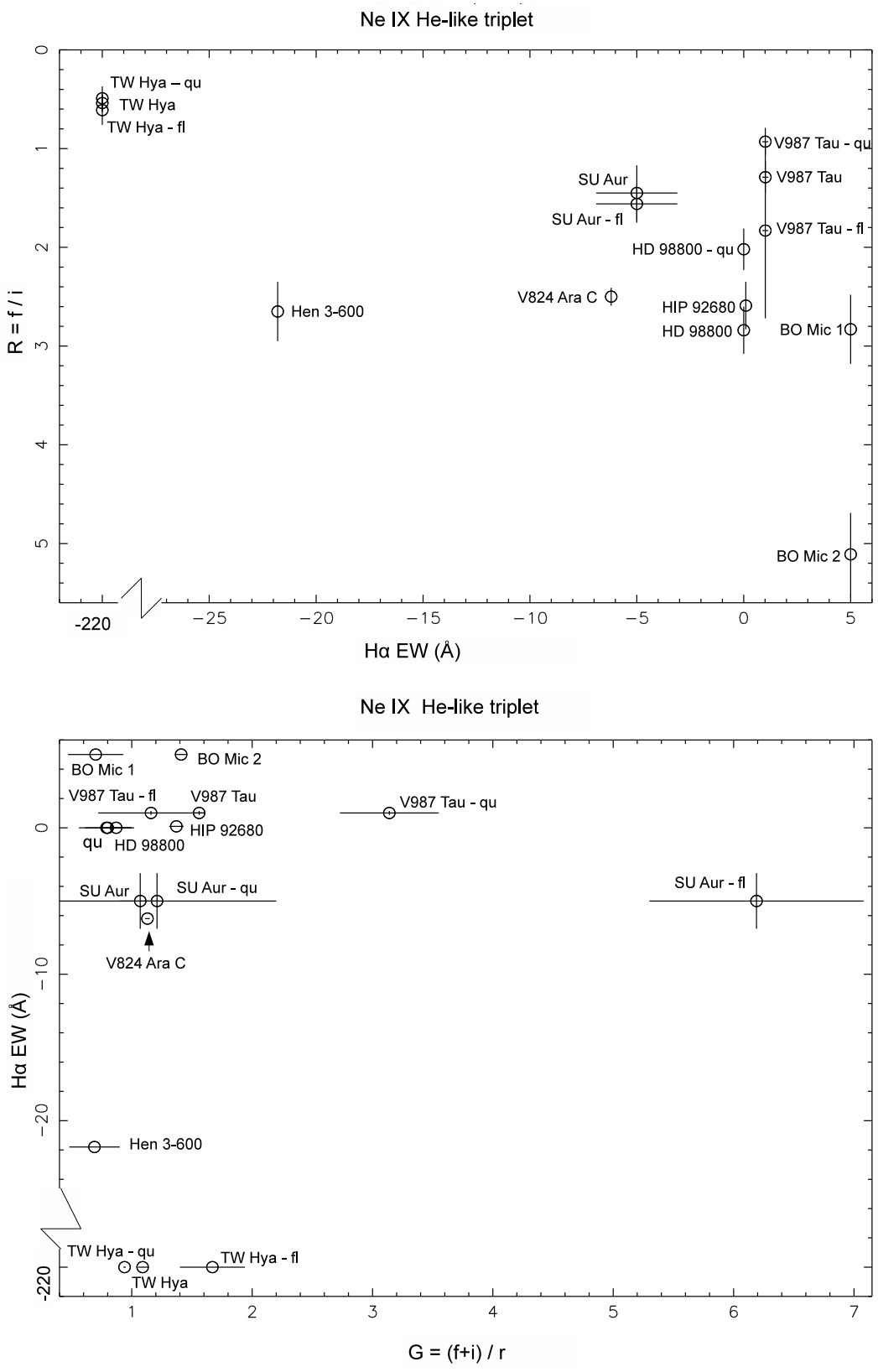

Figure 4.6: R and G ratio versus Hα EW for the Ne IX He-like triplet

V987 Tau, but the densities for V987 Tau inferred by the R ratio of Si XIII are lower than the theoretically predicted densities for this triplet.

TW Hya and Hen 3-600 again show high densities derived from the Mg XI He-like triplet, but high densities are also derived for V987 Tau and BO Mic from the Mg XI line. Also, the flaring state observations of TW Hya and V987 Tau exhibit higher densities than the quiescent states, opposite of what was observed with the Si XIII triplets. Interestingly, the second observation of BO Mic also shows a higher density derived from the Mg XI triplet than from either the Si XIII or the Ne IX triplet, possibly indicating that BO Mic was flaring during the second observation, in comparison with the first. No distinction can be made between the X-ray emitting plasmas of the flaring and quiescent states of HD 98800 and SU Aur.

TW Hya and V987 Tau in quiescence show the highest densities as indicated by the Ne IX triplet R ratios. For the stars with significant flares, the results from the Ne IX triplets are more consistent with the Si XIII triplet results than with the Mg XI results. Each flaring star (TW Hya, SU Aur, HD 98800 and V987 Tau) shows slightly higher density (lower R) in the quiescent state and slightly lower density (higher R) in the flaring state. If accretion processes are associated with X-ray emitting plasmas of high densities, this trend could indicate that accretion is suppressed during flares in these young stars. Alternatively, accretion may initially trigger a flare which in turn masks the signature of that accretion.

4.2.2.2 G ratios and inferred temperatures

Errors on the G measurements from the Si XIII triplet are higher than for the R ratios, and there is no difference among the temperature ranges for various Hα EWs except for TW Hya. The values of the G ratios for Si XIII do not differ within the errors for the flaring and quiescent states of SU Aur and HD 98800. V987 Tau shows a cooler temperature in quiescence, and the full spectrum of TW Hya indicated a cooler temperature than either the flaring or quiescent states, though this may be because of low signal-to-noise ratios in the flaring and quiescent states.

As mentioned in the previous section, the Mg XI triplet G ratios have very large errors, and thus the temperature range indicated by these ratios spans the entire plausible temperature range for each observation. The Ne IX G ratios are well-constrained. The flaring and quiescent states do not have distinguishable temperature ranges within the errors for HD 98800 and SU Aur, in agreement with the results from the Si XIII triplet. The quiescent and flaring states of TW Hya are very distinct, indicating there are likely two X-ray emitting plasmas of different temperatures producing the Ne IX emission. V987 Tau also shows a much cooler temperature for the quiescent state. SU Aur also shows a very cool temperature, but for the flaring state, though this is most likely due to poor line measurements. Except for the few exceptions noted above, the errors on the G measurements for all three triplets, Si XIII, Mg XI and Ne IX, are too high to place constraints on the temperature of the X-ray emitting plasmas of these stars.

4.2.3 *Improvements on data sets and models*

Although young stars are strong X-ray emitters among stars, they are still relatively weak X-ray emitters in comparison to other astrophysical objects. The integration times for each of our observations were on the order of ∼50 to 100 ks but some lines were still too weak to be measured. The majority of our measurements produce R and G ratios that within three-sigma span the entire range of plausible plasma densities and temperatures. There are a few exceptions in which the line measurements provide much better constraints, notably the Ne IX triplet measurements of TW Hya, V987 Tau, and HIP 92680. However, although the measurements for V987 Tau and HIP 92680 have low errors, the measurements themselves fall below the theoretically predicted plasma density/temperature regime. The same is true for the Si XIII measurements of Hen3-600 and V824 Ara C. This may indicate that the theoretical predictions for the temperature and density at which these particular lines can emit X-rays need to be re-evaluated.

4.2.4 *H-like Lyman α to He-like resonance line ratios*

For low-resolution X-ray spectra, like the observations of V710 Tau presented earlier in this chapter, the temperatures of the X-ray emitting plasmas are estimated by model-fitting in which one estimates the overall temperature structure of given plasma. With high-resolution X-ray data, individual line fluxes can be measured, and sets of line ratios can determine the temperatures likely to form a particular set of lines (e.g., the Ne IX He-like triplet). As shown in sections 4.3 and 4.4 above,

the G ratio (G = $(f+i)/r$) is indicative of plasma temperature. In addition to this ratio, one can infer temperature using the Hydrogen-like Lyman α (HLα) line and the Helium-like resonance (Her) line for a given ion. The HLα and Her lines for a given ion are often the strongest emitting X-ray lines in a Chandra HETGS observation. The ratio of these two lines is a proxy for temperature, since the two lines originate from adjacent ionization states for the same element and are thus not dependent on elemental abundances (Ness et al., 2004). Although the temperature estimates from these line ratios use the same plasma emission line database (APED), the uncertainty in temperature is slightly reduced since these two lines are strongly exposed and the contribution from weaker lines with greater uncertainty are not included (Ness et al., 2004).

For the Si, Mg, and Ne HLα/Her ratios, we find temperatures better constrained but in the same temperature ranges predicted by the G ratios with a few notable exceptions. The Ne HLα/Her ratios are systematically skewed to indicate slightly higher temperatures than the same G ratio for a given element. This suggests some difference in the theoretical predictions used to infer the temperatures. For all three elements, we plotted the HLα/Her ratios versus X-ray luminosity (see Chapter 3, Figure 3.9). We find a linear correlation for each elemental ratio, and the slope of that relationship decreases with increasing Z (from Ne to Mg to Si). Ness et al. (2004) performed a similar analysis with their sample of coronally active stars and found the same correlation. They attribute a higher X-ray luminosity to higher levels of activity, and thus higher temperatures are seen in stars with higher activity levels. For our sample, X-ray luminosity is not correlated with Hα emission, and the differences in

X-ray luminosity scale with distance rather than activity level for our sources.

4.2.5 *Abundances*

As discussed in Section 3.5, we determined a set of five ratios for each spectrum in our sample using the method described in (Liefke et al., 2008). Kastner et al. (2004) find Ne to be overabundant with respect to iron for HD 98800, similar to the results for TW Hya (Kastner et al., 2002) though not as extreme. Their determination of the Ne/Fe ratio stems from the fact that Ne IX and Fe XVII lines form at similar temperatures.

Other young stars including V710 Tau (Shukla et al., 2008) and Hen 3-600 (Huenemoerder et al., 2007) have also been observed to have a high Ne/Fe ratio. Drake & Testa (2005) suggest that metal depletion with respect to neon observed in young stars is evidence of condensation of metals onto grains. Models of molecular clouds at densities $n_e > 10^7$ cm^{-3} predict that nearly all metals condense into grains (Charnley, 1997). Like molecular clouds, regions of circumstellar disks around young stars can also have densities above 10^7, particularly in the inner disk and in the mid-plane of the disk. If the process of grain condensation is happening in these areas of the disk, we expect dust grain formation to take place, causing metals to preferentially move out of the gas phase and into solid dust grains. For young accreting stars, the gas in the inner part of the circumstellar disk accretes onto the star but the dust grains are preferentially left behind in the disk. The gas in the circumstellar disk is then depleted of metals trapped in the dust grains. As this gas separates from the dust grains, the metal-depleted gas is accreted onto the star and shock heated. If grains

formed in circumstellar material of these stars at any point during their development, we would expect the X-ray plasma in the vicinity of the star to be similarly depleted. For all of the stars in our sample, we do see an enhanced Ne/Fe ratio. Argiroffi et al. (2005) find that for the five stars in their analysis (TW Hya, TWA 5, HD 98800, PZ Tel, and V987 Tau) the Ne/Fe ratio decreases as Hα decreases. We do not find a similar trend in our data TW Hya has the lowest Ne/Fe ratio (3.15 ± 0.51) in our sample. This ratio is most pronounced with a value of 8.94 ± 1.60 for Hen 3-600, which is also in the TW Hya association. TW Hya, Hen 3-600, and HD 98800 show remarkably different Ne/Fe ratios considering they are all members of the TW Hya association and therefore presumably formed from the same primordial cloud.

A high Ne/Fe ratio may also be indicative of inverse first ionization potential (FIP) effect. The first ionization potential of a particular element is indicative of the energy required to remove the outermost electrons. FIP increases as the number of valence electrons approaches eight and decreases with increasing atomic radius. In late-type stars with low activity levels, elements with low FIP (i.e., easily ionized) tend to be enhanced with respect to those with higher FIP (Feldman & Widing, 2003). However, in active stars, an inverse FIP effect has been noted (Argiroffi et al., 2005, and references therein). The Ne/Fe ratio is a good indicator of inverse FIP effects since Ne has a very high FIP (21.6 eV) and Fe a relatively low one (7.9 eV). Currently, one cannot differentiate between a high Ne/Fe ratio caused by grain depletion or the inverse FIP effect.

From a sample of high-resolution Chandra spectra of nearby cool stars, Drake & Testa (2005) find a nearly constant Ne/O ratio of 0.41. Since this ratio is constant

among late type, non-accreting stars, they further state that a higher Ne/O ratio can be used to identify grain depletion in the plasmas generating X-rays via accretion, since the oxygen is depleted (i.e., locked in grains) relative to the neon (Drake et al., 2005). They find TW Hya to have a Ne/O ratio of 1.06 ± 0.13, as determined from Chandra HETGS data by the method described in Drake & Testa (2005), and interpret this high ratio as evidence of "compositional peculiarities" in the accreting gas, indicating that it is depleted of oxygen which is likely due to grain formation. For another accreting star, BP Tau, however, they find a Ne/O ratio similar to that which is found in their sample of coronally active stars. They state the difference to be due to the differences in ages and evolutionary states of the two stars (Drake et al., 2005).

For the stars in our sample, we do not find the Ne/O ratio for the stars that are accreting to be as high as those reported by Drake et al. (2005) for TW Hya. We find the Ne/O ratio for TW Hya to be 0.68 ± 0.14, lower than what is found by Drake et al. (2005) with Chandra observations of TW Hya, but consistent with the Ne/O ratio derived from XMM-Newton observations of TW Hya. The quiescent state observation of TW Hya does have a higher Ne/O ratio of 0.90 ± 0.16. Only two other observations in our sample show a high Ne/O ratio, HD 98800 (0.87 ± 0.39) and DoAr 21 (0.71 ± 0.64) both in the flaring state. However, both of these have significant errors that make it difficult to distinguish them from the rest of the sample based on this ratio. We therefore find no strong evidence that the Ne/O ratio is enhanced for any of our sources except TW Hya in quiescence, and therefore the X-ray emitting plasmas are not depleted of oxygen relative to neon.

CHAPTER V

CONCLUSIONS

5.1 Imaging Spectroscopy

We present the first spatially resolved X-ray observations of the wTTS/cTTS binary system V710 Tau. The two stars were cleanly resolved by the Chandra/ACIS-S3 imager, allowing us to separately analyze the X-rays emitted by each star. Both stars maintained near-constant count rates within each observation. V710 Tau N was evidently undergoing a flare event during the December 2004 observation since its X-ray flux was a factor $\sim$5 larger in December 2004 than in April 2005.

The best-fit models to each component of the V710 Tau binary indicate plasma temperatures in the range $kT_X \sim 0.7-1.1$ keV for V710 Tau S in 2004 December and for both stars in 2005 April, and that the X-ray emitting plasma associated with V710 Tau N was much hotter during the former exposure and marginally hotter during the latter exposure than the plasma associated with V710 Tau S. The 2004 December flare-state spectrum of V710 Tau N appears to require both a soft component and the addition of a second, higher-temperature plasma component ($kT_X \sim 2.5-3$ keV). There is also evidence for an enhanced Ne/Fe abundance ratio in the X-ray emitting plasma associated with V710 Tau N.

The spectral modeling results indicate that the individual components of this wTTS/cTTS binary system follow general trends apparent in recent statistical studies of cTTS and wTTS (e.g.,Wolk et al. (2005); Telleschi et al. (2007a)). Specifically, the

cTTS consistently exhibited somewhat harder X-ray emission than the wTTS, and the X-ray spectrum of the cTTS hardened considerably during the December 2004 flare event.

Hence, in the V710 Tau system, harder X-ray flux and possibly, an enhanced Ne/Fe abundance ratio appear to accompany enhanced stellar accretion. Additional, deeper Chandra exposures of V710 Tau and similar wTTS/cTTS binaries systems will better constrain the plausible sources of X-ray emission from low-mass, pre-main sequence stars. Deeper Chandra observations of V710 Tau N/S, as well as observations of similar "mixed" TTS binaries, are required to establish whether the characteristic plasma temperatures and abundances of cTTS and wTTS binary components differ consistently and significantly.

5.2 High Resolution X-ray Spectroscopy

We present the first globally consistent analysis of the young, pre-main sequence stars observed with Chandra HETGS to date. Our sample included two classical, four weak-lined, two post-T Tauri and one main sequence star. Each star was observed over moderately long integration times ($\sim$50-100 ks) and five of the stars in the sample showed significant flaring over the duration of their respective observations.

We extracted spectra for the full observations from the first order HEG and MEG data for each observation, and for the stars that exhibited flaring, we also extracted separate spectra from both the flaring and quiescent states.

For each spectrum, we estimated the continuum level with a multi-temperature plasma model fit to the line-free regions. Once the continuum was removed, individual

spectral emission lines were measured, particularly the H-like Lyα line and the He-like triplets of Si XIII, Mg XI, and Ne IX, but also selected lines of S VI and Fe XVII. From these measurements, we calculated the R ratio (f/i) and G ratio ($(f+i)/r$), which should be sensitive to the density and temperature, respectively, of the X-ray plasma producing the He-like triplet of a given ion.

The G ratio did not provide meaningful constraints on the plasma temperatures inferred from the He-like triplets of Si XIII, Mg XI, and Ne IX. For most of our observations, the errors on the G ratio measurements spanned the entire plausible range of plasma temperatures predicted by the theoretical models. However, even for the observations with reasonable signal-to-noise ratios, several of the G ratio values indicated temperatures outside the range of predicted values. We also measured the HLα/He-r ratios for these three elements, but although the temperatures were better constrained, no correlation between temperature and Hα emission was found. The density-sensitive R ratio is better constrained for our observations than the G ratio. The two sources with the highest Hα EW, TW Hya and Hen 3-600, also have the lowest R ratios (highest density) as determined from the Si XIII and Ne IX triplets; however, these low R ratios are also observed for stars not thought to be accreting (small Hα EW) in our sample. Consequently, we found no significant trend in observables that correlates either the R ratio or the G ratio with Hα emission, and therefore we found no correlation between the density or temperature of the X-ray emitting plasma with accretion.

For those observations for which we extracted separate quiescent and flaring state observations, we find that the Si XIII and Ne IX R ratios indicate that the quiescent

state observations have slightly higher densities than the flaring state observations, though the errors on the R ratios overlap at the one sigma level, so that the conclusion that the X-ray emitting plasmas are different (one higher, one lower density) during the quiescent and flaring states is of only marginal significance. If a high density is indicative of accretion, as has been suggested for TW Hya (Kastner et al., 2002; Stelzer & Schmitt, 2004), then, although this result appears contradictory, X-ray evidence of accretion may be more prominent during the quiescent state observations. However, it is also possible that accretion takes place continually, but that the high-density accretion signature is masked during the flare when accretion is presumably occurring more rapidly. These data suggest therefore the possibility that different X-ray emitting plasmas are the dominant producers of X-ray emission during the flaring and quiescent epochs. Longer integration time observations are necessary to distinguish whether plasmas of different densities produce X-ray emission during the flaring and quiescent epochs.

We also measured temperature-independent elemental abundance ratios using the technique described by Liefke et al. (2008). Using the strongest lines (HLα and the He-like triplets of S, Si, Mg, Ne, and O) with the lowest uncertainties, we were able to determine abundance ratios for S/Si, Si/Mg, Mg/Ne, Ne/Fe, and Mg/Fe. We find that all the stars in our sample have a high Ne/Fe ratio compared to solar photospheric values. A high Ne/Fe ratio may be due to the inverse FIP effect, an abundance anomaly seen in many coronal sources (Huenemoerder et al., 2007), or may be due to grain growth in the circumstellar disks of these stars, which in turn would lead to the accretion of metal-depleted gas onto these stars.

Drake et al. (2005) found that the Ne/O ratio has an average value of 0.44 in stellar coronae for active, nearby solar-like stars. Thus a Ne/O ratio greater than 0.44 in our observations would be indicative of oxygen depletion due to grain growth in the disk. Drake et al. (2005) found that indeed Ne/O was enhanced along with Ne/Fe for TW Hya, apparently confirming that the X-ray emitting plasma from TW Hya is from gas depleted of both Fe and O, as those elements condense onto refractory dust grains in the inner regions of TW Hya's circumstellar disk. However, for our sample, the data for only one star, TW Hya in quiescence, shows an enhanced Ne/O ratio. The average Ne/O ratio for our sample of young and pre-main sequence stars is 0.44, consistent with the value found by Drake & Testa (2005) field stars. The X-ray emitting plasmas of the stars in our sample are therefore not likely to be depleted of oxygen. This result may mean that the high Ne/Fe ratios are due to the inverse FIP effect, not to the accretion of iron-depleted gas. However, iron-oxide-rich grains would form at slightly lower temperatures (and slightly further out in the disk) than pure iron-rich grains. Since accretion of gas from the disk would likely occur from the hottest gas at the inner disk boundary, the possibility remains that the enhanced Ne/Fe ratio is a signature of accretion.

REFERENCES

Akeson, R. L., Ciardi, D. R., van Belle, G. T., & Creech-Eakman, M. J. 2002, ApJ, 566, 1124

Akeson, R. L., Rice, W. K. M., Boden, A. F., Sargent, A. I., Carpenter, J. M., & Bryden, G. 2007, ApJ, 670, 1240

Andre, P. & Montmerle, T. 1994, ApJ, 420, 837

Andrews, S. M. & Williams, J. P. 2005, ApJ, 631, 1134

Argiroffi, C., Drake, J. J., Maggio, A., Peres, G., Sciortino, S., & Harnden, F. R. 2004, ApJ, 609, 925

Argiroffi, C., Maggio, A., Peres, G., Stelzer, B., & Neuhäuser, R. 2005, A&A, 439, 1149

Arnaud, K. A. 1996, in ASP Conf. Ser. 101: Astronomical Data Analysis Software and Systems V, ed. G. H. Jacoby & J. Barnes, 17

Asplund, M., Grevesse, N., & Sauval, A. J. 2005, in Astronomical Society of the Pacific Conference Series, Vol. 336, Cosmic Abundances as Records of Stellar Evolution and Nucleosynthesis, ed. T. G. Barnes, III & F. N. Bash, 25–+

Audard, M., Drake, S. A., Güdel, M., Mewe, R., Pallavicini, R., Simon, T., Singh, K. P., Skinner, S. L., & White, N. 2004, in IAU Symposium, Vol. 219, Stars as Suns : Activity, Evolution and Planets, ed. A. K. Dupree & A. O. Benz, 243

Audard, M., Skinner, S. L., Smith, K. W., Güdel, M., & Pallavicini, R. 2005, in ESA Special Publication, Vol. 560, 13th Cambridge Workshop on Cool Stars, Stellar Systems and the Sun, ed. F. Favata, G. A. J. Hussain, & B. Battrick, 411

Barnes, J. R., Collier Cameron, A., James, D. J., & Donati, J.-F. 2000, MNRAS, 314, 162

Barrado y Navascués, D. & Martín, E. L. 2003, AJ, 126, 2997

Barsony, M., Ressler, M. E., & Marsh, K. A. 2005, ApJ, 630, 381

Bary, J. S., Weintraub, D. A., & Kastner, J. H. 2002, ApJL, 576, L73

Beckwith, S. V. W., Sargent, A. I., Chini, R. S., & Guesten, R. 1990, AJ, 99, 924

Bertout, C., Basri, G., & Bouvier, J. 1988, ApJ, 330, 350

Bouvier, J. & Appenzeller, I. 1992, A&AS, 92, 481

Canizares, C. R., Davis, J. E., Dewey, D., Flanagan, K. A., Galton, E. B., Huenemoerder, D. P., Ishibashi, K., Markert, T. H., Marshall, H. L., McGuirk, M., Schattenburg, M. L., Schulz, N. S., Smith, H. I., & Wise, M. 2005, PASP, 117, 1144

Charnley, S. B. 1997, MNRAS, 291, 455

Chartas, G., Garmire, G. P., Nousek, J. A., Koch, S., Kissel, S. E., Prigozhin, G. Y., & Bautz, M. W. 1998, in Society of Photo-Optical Instrumentation Engineers (SPIE) Conference Series, Vol. 3444, Society of Photo-Optical Instrumentation Engineers (SPIE) Conference Series, ed. R. B. Hoover & A. B. Walker, 258–266

Drake, J. J. & Testa, P. 2005, Nature, 436, 525

Drake, J. J., Testa, P., & Hartmann, L. 2005, ApJL, 627, L149

Dunstone, N. J., Barnes, J. R., Cameron, A. C., & Jardine, M. 2006, MNRAS, 365, 530

Favata, F., Flaccomio, E., Reale, F., Micela, G., Sciortino, S., Shang, H., Stassun, K. G., & Feigelson, E. D. 2005, ApJS, 160, 469

Favata, F., Giardino, G., Micela, G., Sciortino, S., & Damiani, F. 2003, A&A, 403, 187

Feigelson, E. D., Gaffney, J. A., Garmire, G., Hillenbrand, L. A., & Townsley, L. 2003, ApJ, 584, 911

Feigelson, E. D. & Montmerle, T. 1999, ARA&A, 37, 363

Feigelson et al. 2005, ApJS, 160, 379

Feldman, U. & Widing, K. G. 2003, Space Science Reviews, 107, 665

Flaccomio, E., Micela, G., & Sciortino, S. 2003, A&A, 397, 611

Furlan, E., Hartmann, L., Calvet, N., D'Alessio, P., Franco-Hernández, R., Forrest, W. J., Watson, D. M., Uchida, K. I., Sargent, B., Green, J. D., Keller, L. D., & Herter, T. L. 2006, ApJS, 165, 568

Gabriel, A. H. & Jordan, C. 1969, MNRAS, 145, 241

Gauvin, L. S. & Strom, K. M. 1992, ApJ, 385, 217

Gehrels, N. 1986, ApJ, 303, 336

Getman et al. 2005, ApJS, 160, 319

Giardino, G., Favata, F., Silva, B., Micela, G., Reale, F., & Sciortino, S. 2006, A&A, 453, 241

Gregory, S. G., Wood, K., & Jardine, M. 2007, MNRAS, 379, L35

Güdel, M., Audard, M., Briggs, K., Haberl, F., Magee, H., Maggio, A., Mewe, R., Pallavicini, R., & Pye, J. 2001, A&A, 365, L336

Gullbring, E., Barwig, H., Chen, P. S., Gahm, G. F., & Bao, M. X. 1996, A&A, 307, 791

Günther, H. M., Liefke, C., Schmitt, J. H. M. M., Robrade, J., & Ness, J.-U. 2006, A&A, 459, L29

Herbig, G. H. & Bell, K. R. 1988, Catalog of emission line stars of the Orion population : 3 : 1988, ed. G. H. Herbig & K. R. Bell

Hildebrand, R. H. 1983, QJRAS, 24, 267

Houck, J. C. & Denicola, L. A. 2000, in Astronomical Society of the Pacific Conference Series, Vol. 216, Astronomical Data Analysis Software and Systems IX, ed. N. Manset, C. Veillet, & D. Crabtree, 591

Houk, N. 1978, Michigan catalogue of two-dimensional spectral types for the HD stars, ed. N. Houk

Huenemoerder, D. 2007, aglc - ACIS Grating Light Curve, `http://space.mit.edu/cxc/analysis/aglc/index.html`

Huenemoerder, D. P., Canizares, C. R., & Schulz, N. S. 2001, ApJ, 559, 1135

Huenemoerder, D. P., Kastner, J. H., Testa, P., Schulz, N. S., & Weintraub, D. A. 2007, ApJ, 671, 592

Huenemoerder, D. P., Testa, P., & Buzasi, D. L. 2006, ApJ, 650, 1119

Hughes, A. M., Wilner, D. J., Qi, C., & Hogerheijde, M. R. 2008, ApJ, 678, 1119

Imanishi, K., Tsujimoto, M., & Koyama, K. 2002, ApJ, 572, 300

Jardine, M., Cameron, A. C., Donati, J.-F., Gregory, S. G., & Wood, K. 2006, MNRAS, 367, 917

Johns, C. M. & Basri, G. 1995, ApJ, 449, 341

Johns-Krull, C. M. 2007, ApJ, 664, 975

Kastner, J. H., Huenemoerder, D. P., Schulz, N. S., Canizares, C. R., Li, J., & Weintraub, D. A. 2004, ApJL, 605, L49

Kastner, J. H., Huenemoerder, D. P., Schulz, N. S., Canizares, C. R., & Weintraub, D. A. 2002, ApJ, 567, 434

Kastner, J. H., Richmond, M., Grosso, N., Weintraub, D. A., Simon, T., Henden, A., Hamaguchi, K., Frank, A., & Ozawa, H. 2006, ApJL, 648, L43

Kastner, J. H., Zuckerman, B., Weintraub, D. A., & Forveille, T. 1997, Science, 277, 67

König, B., Neuhäuser, R., & Stelzer, B. 2001, A&A, 369, 971

Li, J., Kastner, J. H., Prigozhin, G. Y., & Schulz, N. S. 2003, ApJ, 590, 586

Liedahl, D. A., Osterheld, A. L., & Goldstein, W. H. 1995, ApJL, 438, L115

Liefke, C., Ness, J.-U., Schmitt, J. H. M. M., & Maggio, A. 2008, A&A, 491, 859

Makarov, V. V. 2003, AJ, 126, 1996

Martin, E. L. 1997, A&A, 321, 492

Martin, E. L. & Brandner, W. 1995, A&A, 294, 744

Mewe, R., Gronenschild, E. H. B. M., & van den Oord, G. H. J. 1985, A&AS, 62, 197

Mewe, R., Lemen, J. R., & van den Oord, G. H. J. 1986, A&AS, 65, 511

Montes, D., López-Santiago, J., Gálvez, M. C., Fernández-Figueroa, M. J., De Castro, E., & Cornide, M. 2001, MNRAS, 328, 45

Montmerle, T. 2002, in Astronomical Society of the Pacific Conference Series, Vol. 277, Stellar Coronae in the Chandra and XMM-NEWTON Era, ed. F. Favata & J. J. Drake, 173–+

Morrison, R. & McCammon, D. 1983, ApJ, 270, 119

Muzerolle, J., Calvet, N., Briceño, C., Hartmann, L., & Hillenbrand, L. 2000, ApJL, 535, L47

Ness, J.-U., Güdel, M., Schmitt, J. H. M. M., Audard, M., & Telleschi, A. 2004, A&A, 427, 667

Ness, J.-U., Mewe, R., Schmitt, J. H. M. M., & Raassen, A. J. J. 2002a, in Astronomical Society of the Pacific Conference Series, Vol. 277, Stellar Coronae in the Chandra and XMM-NEWTON Era, ed. F. Favata & J. J. Drake, 545

Ness, J.-U., Schmitt, J. H. M. M., Burwitz, V., Mewe, R., Raassen, A. J. J., van der Meer, R. L. J., Predehl, P., & Brinkman, A. C. 2002b, A&A, 394, 911

Nguyen, D. C., Scholz, A., van Kerkwijk, M. H., Jayawardhana, R., & Brandeker, A. 2009, ApJL, 694, L153

Pallavicini, R., Golub, L., Rosner, R., Vaiana, G. S., Ayres, T., & Linsky, J. L. 1981, ApJ, 248, 279

Pasquini, L., Cutispoto, G., Gratton, R., & Mayor, M. 1991, A&A, 248, 72

Pasquini, L., Schmitt, J. H. M. M., & Pallavicini, R. 1989, A&A, 226, 225

Porquet, D. 2005, in American Institute of Physics Conference Series, Vol. 774, X-ray Diagnostics of Astrophysical Plasmas: Theory, Experiment, and Observation, ed. R. Smith, 177–186

Porter, R. L. & Ferland, G. J. 2007, ApJ, 664, 586

Pottasch, S. R. 1967, ApJ, 150, 361

Pradhan, A. K. & Shull, J. M. 1981, ApJ, 249, 821

Preibisch, T. & Feigelson, E. D. 2005, ApJS, 160, 390

Preibisch, T., Kim, Y.-C., Favata, F., Feigelson, E. D., Flaccomio, E., Getman, K., Micela, G., Sciortino, S., Stassun, K., Stelzer, B., & Zinnecker, H. 2005, ApJS, 160, 401

Randich, S. 2000, in ASP Conf. Ser. 198: Stellar Clusters and Associations: Convection, Rotation, and Dynamos, ed. R. Pallavicini, G. Micela, & S. Sciortino, 401

Rebull, L. M., Stapelfeldt, K. R., Werner, M. W., Mannings, V. G., Chen, C., Stauffer, J. R., Smith, P. S., Song, I., Hines, D., & Low, F. J. 2008, ApJ, 681, 1484

Robrade, J. & Schmitt, J. H. M. M. 2006, A&A, 449, 737

Scelsi, L., Maggio, A., Peres, G., & Pallavicini, R. 2005, A&A, 432, 671

Schmitt, J. H. M. M. & Ness, J.-U. 2002, A&A, 388, L13

Schmitt, J. H. M. M., Robrade, J., Ness, J.-U., Favata, F., & Stelzer, B. 2005, A&A, 432, L35

Schuetz, O., Meeus, G., Sterzik, M. F., & Peeters, E. 2009, ArXiv e-prints

Shukla, S. J., Weintraub, D. A., & Kastner, J. H. 2008, ApJ, 683, 893

Singh, K. P., Drake, S. A., Gotthelf, E. V., & White, N. E. 1999, ApJ, 512, 874

Smith, R. K., Brickhouse, N. S., Liedahl, D. A., & Raymond, J. C. 2001, ApJL, 556, L91

Soderblom, D. R., King, J. R., & Henry, T. J. 1998, AJ, 116, 396

Stassun, K. G., Ardila, D. R., Barsony, M., Basri, G., & Mathieu, R. D. 2004, AJ, 127, 3537

Stelzer, B. & Neuhäuser, R. 2001, A&A, 377, 538

Stelzer, B., Neuhäuser, R., & Hambaryan, V. 1999, in Astronomical Society of the Pacific Conference Series, Vol. 188, Optical and Infrared Spectroscopy of Circumstellar Matter, ed. E. Guenther, B. Stecklum, & S. Klose, 151

Stelzer, B. & Schmitt, J. H. M. M. 2004, A&A, 418, 687

Sylvester, R. J., Skinner, C. J., Barlow, M. J., & Mannings, V. 1996, MNRAS, 279, 915

Telleschi, A., Güdel, M., Briggs, K. R., Audard, M., & Palla, F. 2007a, A&A, 468, 425

Telleschi, A., Güdel, M., Briggs, K. R., Audard, M., & Scelsi, L. 2007b, A&A, 468, 443

Testa, P., Reale, F., Garcia-Alvarez, D., & Huenemoerder, D. P. 2007, ApJ, 663, 1232

Vuong, M. H., Montmerle, T., Grosso, N., Feigelson, E. D., Verstraete, L., & Ozawa, H. 2003, A&A, 408, 581

Webb, R. A., Zuckerman, B., Platais, I., Patience, J., White, R. J., Schwartz, M. J., & McCarthy, C. 1999, ApJL, 512, L63

Weinberger, A. J., Becklin, E. E., Schneider, G., Chiang, E. I., Lowrance, P. J., Silverstone, M., Zuckerman, B., Hines, D. C., & Smith, B. A. 2002, ApJ, 566, 409

Weintraub, D. A., Sandell, G., & Duncan, W. D. 1989, ApJL, 340, L69

White, R. J. & Ghez, A. M. 2001, ApJ, 556, 265

Wolk, S. J., Harnden, Jr., F. R., Flaccomio, E., Micela, G., Favata, F., Shang, H., & Feigelson, E. D. 2005, ApJS, 160, 423

Wolter, U., Robrade, J., Schmitt, J. H. M. M., & Ness, J. U. 2008, A&A, 478, L11

Zuckerman, B. & Webb, R. A. 2000, ApJ, 535, 959